Part I: Near-source Acoustic Coupling Between the Atmosphere and the Solid Earth During Volcanic Eruptions

Part II: Nearfield Normal Mode Amplitude Anomalies of the Landers Earthquake

Thesis by

Shingo Watada

In Partial Fulfillment of the Requirements

for the Degree of

Doctor of Philosophy

California Institute of Technology

Pasadena, California

1995

(Defended March 16, 1995)

Acknowledgments

I have been very fortunate to be a student in the Seismological Laboratory. My thesis advisors H. Kanamori and D. L. Anderson are truly great teachers. While they allowed me to pursue my scientific curiosity in a way I chose, consulting with them often opened my eyes to new directions when my research had reached a stagnation point. They have been very supportive, sometimes enthusiastic, of my slow studies.

In my early years in the Seismo Lab, T. Tanimoto taught me all the necessities to do research which formed the basic for the studies of later years. Without his introduction to long–period seismology, I could not have completed the research in this thesis. My academic advisor, D. V. Helmberger, protected me and encouraged me many times, like a father.

I also thank F. Gilbert for his discussions and sending me his notes, R. Clayton for taking care of me as a graduate student in the Seismo Lab, D. G. Harkrider for sharing his old wisdom and witty talks, and D. Neuhauser, G. Barbar and B. Zajac for maintaining the Seismo computer system.

Discussions during the Seismo coffee breaks, where one of my thesis research started, have been one of the most valuable resources available. Coffee breaks were always friendly and very stimulating.

Cheerful Seismo Lab staffs, Ann Freeman, Janet Fernades, Dee Page, Cheryl Contopulos and Sue Yamada, made my life in the lab much easier and more fun. Seeing fellow graduate students in the Lab had the largest impact on my Caltech life. Long–term officemates Tom Duffy, Brad Woods, Helen Qian, Craig Scrivner and Xi Song helped me in every aspect. Talking with Linda Rowan, Ed Garnero, Doug Dreger, Hong-Kie Thio, Weishi Huang, Sharon Kedar, Xiaodong Song, Paul Tackley, Toshiko Takata and Lianxing Wen was fun and comfortable. Living with roommates Mark, Marcus, John, Brent, Adam, Scott, Eric and Darrell has been a great source

of joy in my life.

I will remember all of you and what we talked about, saw, ate and, went to — and what I accomplished — with you in California.

Introduction

Long-period seismic waves from moderately large earthquakes somewhere in the world are commonly recorded daily. The study of these waves blossomed into the normal mode theory of the Earth. At long-periods, the generation and propagation of seismic waves by an earthquake are well understood and we can synthesize seismograms with great accuracy. The theory has been successfully used for constructing models of Earth's interior and determining earthquake source mechanisms. Daily observed long-period seismograms are usually explainable and do not violate the 'common' sense of seismologists.

However, the unexpected can happen on Earth. During the 1991 eruption of Mt. Pinatubo, in the Philippines, unidentified long-period harmonic ground motions were observed worldwide. Seismologists searched for a periodic source mechanism in the ground and the air. Anomalously large amplitude long-period surface waves from the 1992 Landers earthquake were observed in Southern California after they traveled the globe many times. Geophysicists pondered on the cause of these unprecedented amplitude anomalies.

In this thesis I tried to understand these new observations using the normal mode theory. The origins of these waves are discussed, physical models are developed, and the hypotheses are tested by comparing observations with predictions from the model, namely synthetic seismograms. The validities of the hypotheses are confirmed, and the results are reinterpreted in order to further understand the behavior of the Earth. This thesis contributes a little to expand the common sense of seismology.

Abstract

This thesis consists of two chapters. In the first chapter the normal mode theory of a spherical Earth model is extended to include the atmosphere and the theory is applied to understand the observation of air-ground acoustic coupling during volcanic eruptions and to construct synthetic ground motions. In chapter II, the fully developed normal mode theory of 3D Earth is applied to the nearfield amplitude anomalies of the surface waves of the Landers rearthquake. Synthetic seismograms for the recently-available three dimensional seismic global Earth models are constructed using the normal mode theory and compared with observations. The horizontal scale and the location of lateral seismic velocity variations which caused the amplitude anomalies are examined in detail.

Part I:

Long-period harmonic Rayleigh waves were observed by worldwide seismographic networks during the eruption of Mt. Pinatubo in 1991. It has been suggested that these Rayleigh waves were excited, through atmospheric-solid Earth coupling, by atmospheric oscillations set off by the eruption. We investigated this problem using the Earth's normal modes computed for a spherically symmetric Earth model with the solid (elastic) Earth, ocean and atmosphere. These normal modes represent Rayleigh waves in the solid Earth, tsunamis in the ocean, and Lamb waves, internal acoustic waves and internal gravity waves in the atmosphere. Since the atmosphere has a low sound velocity channel below the thermosphere (altitude 90 km), two characteristic acoustic modes with periods of 230 and 270 s exist. The energy coupling between atmospheric acoustic waves and Rayleigh waves is efficient because of the proximity of the horizontal phase velocities of these waves. The energy distribution suggests that a low altitude volcanic eruption would excite the 230 s mode more strongly than the 270 s mode. This is consistent with the observation for the Pinatubo eruption. In

contrast, the internal gravity mode has a period of 300 s. The barographic oscillation at a period of 300 s observed for the 1980 Mt. St. Helens eruption is probably this mode. However, because of its slow phase velocity, it would not couple to Rayleigh waves efficiently, and cannot be detected with seismographs.

Part II-A:

The 1992 Landers earthquake (M_w=7.3) occurred in the middle of the TERRAscope network. Long-period Rayleigh waves recorded at TERRAscope stations ($\Delta \leq 3°$) after travelling around the Earth show large amplitude anomalies, one order of magnitude larger than spherical Earth predictions up to a period of about 600 s. The ground motions over the epicentral region at and after the arrival of R4-5 are in phase at all stations. These observations are inconsistent with the nearly vertical strike slip mechanism of the Landers earthquake. Synthetic seismograms for a rotating, elliptic and laterally heterogeneous Earth model calculated by the variational method agree well with the observed waveforms. Calculations for various 3D Earth models demonstrate that the amplitudes are very sensitive to the large scale aspherical structure in the crust and the mantle. The anomalies for modes shorter than 300 s period can be explained by lateral heterogeneity shallower than the upper mantle. Rotation of the Earth and lower mantle heterogeneity are required to explain mode amplitudes at longer periods. Current whole mantle seismic tomographic models can fully explain the observed amplitudes longer than 300 s. To assess the effect of the high order lateral heterogeneity in the mantle, more precise estimate of the crustal correction is required.

Part II-B:

We modeled the interaction of the source mechanism and the station location with large-scale lateral heterogeneity using the splitting matrix of an isolated multiplet and the 'source-receiver function' whose spherical harmonic coefficients are given by

P_{st} where s and t are angular and azimuthal order numbers respectively. For a short period of time waveform perturbation is proportional to the integral of products of the splitting function with harmonic coefficients C_{st} and the 'source-receiver' function. For the Landers earthquake and TERRAscope stations source–receiver geometry, the 'source-receiver function' is dominated by the low-order components, paticularly $l = 2, m = \pm 2$ in the epicentral coordinates. This beach-ball like pattern is the same for all the near–source stations located in different quadrants of the strike-slip mechanism. The two maxima of the 'beach ball' pattern coincide with the locations of the degree 2 maxima of the splitting functions; western Pacific and east of South America. These features explain the weak dependence of the waveforms on higher order lateral heterogeneity and similarity of waveforms over the epicentral region. The location and the source mechanism of the Landers earthquake relative to the large scale lateral heterogeneity $l = 2$, including the variations of the cruatal structures, are responsible for the cause of amplitude anomalies near the epicenter. However, the amplitude near the epicenter of an earthquake with a thrust fault type mechanism, for example the Northridge earthquake, is explained well with a spherical Earth model.

Table of Contents

List of Figures

PART I :

List of Tables

PART I :

PART I

Near-source acoustic coupling between the atmosphere and the solid Earth during volcanic eruptions

Abstract

Long-period harmonic Rayleigh waves were observed by worldwide seismographic networks during the eruption of Mt. Pinatubo in 1991. It has been suggested that these Rayleigh waves were excited, through atmospheric-solid Earth coupling, by atmospheric oscillations set off by the eruption. We investigated this problem using the Earth's normal modes computed for a spherically symmetric Earth model with the solid (elastic) Earth, ocean and atmosphere. These normal modes represent Rayleigh waves in the solid Earth, tsunamis in the ocean, and Lamb waves, internal acoustic waves and internal gravity waves in the atmosphere. Since the atmosphere has a low sound velocity channel below the thermosphere (altitude 90 km), two characteristic acoustic modes with periods of 230 and 270 s exist. The energy coupling between atmospheric acoustic waves and Rayleigh waves is efficient because of the proximity of the horizontal phase velocities of these waves. The energy distribution suggests that a low altitude volcanic eruption would excite the 230 s mode more strongly than the 270 s mode. This is consistent with the observation for the Pinatubo eruption. In contrast, the internal gravity mode has a period of 300 s. The barographic oscillation at a period of 300 s observed for the 1980 Mt. St. Helens eruption is probably this mode. However, because of its slow phase velocity, it would not couple to Rayleigh waves efficiently, and cannot be detected with seismographs.

1. Introduction

A major eruption of Mt. Pinatubo (15.14°N 120.35°E) in the Philippines occurred on June 15, 1991. Kanamori and Mori (1992) and Widmer and Zürn (1992) recognized harmonic long-period ground motions associated with the eruption recorded at many world-wide seismographic networks. They confirmed from their group and phase velocities and the retrograde ground particle motion that the waves are fundamental Rayleigh waves radiated from Mt. Pinatubo. The observed wave trains have two distinct peaks at 230 and 270 s in the amplitude spectra. Widmer and Zürn (1992) also reported that similar bichromatic Rayleigh waves with periods of 195 and 266 s were radiated from the 1982 April 4 El Chichón eruption.

Various mechanisms of the generation of the harmonic waves were proposed. Widmer and Zürn (1992) suggested that the geometry of the feeding system or periodic spatial variation of the concentration of dissolved volatiles in the volcano, a feedback system between local atmospheric oscillations and the eruption process are responsible for the excitation of Rayleigh waves. Kanamori and Mori (1992) interpreted them as the seismic Rayleigh waves, excited by atmospheric oscillations set off by the eruption (Kanamori and Mori, 1992). If the source is the acoustic resonance of a magma chamber as suggested by Widmer and Zürn (1992), the size of the chamber required to explain the observed long-period oscillations is at least several hundred kilometers and unrealistic.

Kanamori and Mori (1992) reported that the source phase of the observed Rayleigh waves is azimuthally independent and the oscillatory pressure change observed at near Mt. Pinatubo (Δ=21 km) was about 3.5 mbar (1 bar = 10^5 Pa). They obtained the time history of the atmospheric loading near the volcano by deconvolving the observed Rayleigh waves with the synthetic ground motion excited by a delta function vertical single force. The amplitude of the atmospheric loading force

is about 1.6×10^{17} dyn (1 N = 10^7 dyn). Assuming that the pressure change occurred simultaneously over a circular area, they roughly estimated the radius of the area to be about 40 km.

Kanamori *et al.* (1994) showed that a seismogram recorded during the 1980 Mt. St. Helens eruption displayed a similar oscillation with a period of about 300 s. They tried to explain these spectral peaks observed at Mt. Pinatubo and Mt. St. Helens in terms of characteristic modes of atmospheric oscillations. They showed that in an isothermal atmosphere two distinct modes are excited by a point source in the atmosphere. They also showed that the two peaks, one at the acoustic cutoff frequency and one at a frequency less than the buoyancy frequency, appear in the amplitude spectra of near-source barograms. They suggested that the peaks of the Rayleigh wave spectra observed for the eruption of Mt. Pinatubo and of the seismogram recorded near the Mt. St. Helens eruption correspond to these two characteristic frequencies in the atmosphere.

Long-period air waves in the atmosphere, with a period of about $3 \sim 30$ minutes, from various sources such as volcanic eruptions (Pekeris, 1948; Press and Harkrider, 1966; Harkrider and Press, 1967; Mikumo and Bolt, 1985), a meteorite impact (Pekeris, 1939), ground deformation associated with a large earthquake (Mikumo 1968) and nuclear explosions in the air have been studied by many investigators (e.g., Georges, 1968; Pierce and Posey, 1970). These observed waves are propagating acoustic and gravity waves at far field from the source and none of these addressed the energy coupling of atmospheric waves to seismic Rayleigh waves near the source.

In this thesis, I investigate the acoustic coupling between seismic Rayleigh waves and atmospheric waves, and the excitation of Rayleigh waves by a point source in the atmosphere using the Earth's normal modes computed for a realistic spherically symmetric Earth model with the solid (elastic) Earth, the ocean and the atmosphere.

The objective is to understand the excitation mechanism of the harmonic ground motions generated during the volcanic eruptions of Mt. Pinatubo and Mt. St. Helens and the energy coupling between the waves in the atmospheric and the solid Earth.

2. Method

We employ the normal mode method which has been widely used in seismology. The theories have been presented by Love (1911), Alterman *et al.* (1956), Takeuchi and Saito (1972), Gilbert (1980), Saito (1988), and Woodhouse (1988). Earth models used in these studies are bounded at the surface by the ground or the ocean surface, and the atmosphere has been neglected.

I extend the Earth model to include the atmosphere. A top boundary is placed arbitrarily in the upper atmosphere. Three types of upper boundary conditions, stress free, no vertical dispalacement and radiation, are considered. A volcanic eruption is simply modeled with an isotropic point source in the atmosphere.

The following symbols are used in this section.

r, θ, φ	spherical coordiantes
$(\hat{r}, \hat{\theta}, \hat{\varphi})$	unit vectors
t	time
x	local horizonal coodinate
z	altitude from ground surface
c	sound velocity
A^*	non–dimensional buoyancy frequency defined by eq. 69
A_{ij}	coefficient matrix element of differential eq. 1
B_{ij}	coefficient matrix element of differential eq. 40
C_{ij}	coefficient matrix element of differential eq. 64
E	modal energy density defined by eq. 71
$\mathbf{F}$	energy flux vector
G	gravitational constant
H_s	scale height defined by eq. 49
K	non–dimensional number defined by eq. 65
M_r	total mass inside radius r
N	buoyancy frequency
N_A	acoustic cutoff frequency
P	pressure
Q	pressure eigenfunction
R	radius where top bounday is placed
U	vertical displacement eigenfunction
V, W	horizontal displacement eigenfunctions
U_m	non–dimensional number defined by eq. 50
V_g	non–dimensional number defined by eq. 51

Y_i	eigenfunctions used in eq. 40
Z_i	a set of eigenfunctions modified from Y_i (eqs. 42–45)
X_i	a set of eigenfunctions modified from Z_i (eqs. 62–63)
Γ	specific heat ratio defined by eq. 60
$\mathbf{g}$	gravity vector
k_h, k_x	horizontal wavenumber
k_z	vertical wavenumber
$\mathbf{u}$	displacement vector
$\mathbf{v}$	velocity vector of a meterial element
κ	bulk modulus
ρ	density
ϕ	gravitational potential
Φ	gravity potential eigenfunction
λ	defined by eq. 67
γ	defined by eq. 68
ω	angular frequency
ω_1	cutoff frequency bounding gravity modes
ω_2	cutoff frequency bounding acoustic modes
σ	non–dimensional frequency of ω
σ_1	non–dimensional frequency of ω_1
σ_2	non–dimensional frequency of ω_2
$x^\dagger$	complex conjugate of x
$\|x\|^2$	$xx^\dagger$
x_o	reference state of x
x'	Eulerian perturbation of x
δx	Langrangian perturbation of x

2.1 Equation of motion

We ignore the effects of rotation of the Earth such as the centrifugal force and the Coriolis force because the period of waves we are interested in is much shorter than 1day. We ignore the advection of the background medium such as wind in the atmosphere and thermal diffusion and radiation processes. We consider that the Earth is spherically symmetric.

The differential equations for the eigenfunctions Z_i in a fluid commonly used in seismology (Saito, 1988; Woodhouse, 1988) are

$$\frac{d}{dr}\begin{pmatrix} Z_1 \\ Z_2 \\ Z_5 \\ Z_6 \end{pmatrix} = \mathbf{A}\begin{pmatrix} Z_1 \\ Z_2 \\ Z_5 \\ Z_6 \end{pmatrix}, \qquad 1$$

where A_{ij}'s are given by

$$\begin{pmatrix} -\frac{1}{r}+\frac{l(l+1)g_o}{\omega^2 r^2} & \frac{1}{\kappa}-\frac{l(l+1)}{\omega^2\rho_o r^2} & \frac{l(l+1)}{\omega^2 r^2} & 0 \\ -\omega^2\rho_o+\frac{l(l+1)}{\omega^2 r^2}\rho_o {g_o}^2-4\frac{\rho_o g_o}{r} & \frac{1}{r}-\frac{l(l+1)g_o}{\omega^2 r^2} & \frac{\rho_o g_o l(l+1)}{\omega^2 r^2}-\frac{l+1}{r} & 4\pi G\rho_o \\ -4\pi G\rho_o & 0 & -\frac{l}{r} & 4\pi G \\ -\frac{(l+1)}{r}+\frac{l(l+1)\rho_o g_o}{\omega^2 r^2} & -\frac{l(l+1)}{\omega^2 r^2} & \frac{l(l+1)\rho_o}{\omega^2 r^2} & \frac{l}{r} \end{pmatrix}. \qquad 2$$

These equations are a special case of the more general six simultaneous first order differential equations for a solid model. In a fluid Z_4, the eigenfuction for the shear traction vanishes everywhere because the shear modulus is zero. Z_3 is expressed explicitly as a linear combination of Z_1,Z_2 and Z_5. By eliminating Z_3, the differential equations are reduced to eqs. 1 and 2 (Takeuchi and Saito, 1972; Saito, 1988).

In the equation 2, note that the A_{ij} do not contain the radial gradient of the Earth model parameters and we can avoid numerical differentiations of the model parameters. At the first sight this seems to contradict the intuition that in a fluid the radial gradient of density should play an important role in the equation of motion as a source of buoyancy. When a parcel in a gravitationally stratified fluid is displaced vertically, the parcel expands or contracts adiabatically according to the ambient vertical pressure profile in the fluid and changes its density. The density

contrast between the displaced parcel and the surrounding fluid material is the origin of buoyancy and the expression of this term supposedly includes the vertical density gradient. However, the equations above are a set of correct equations as discussed by Pierce (1966) and indeed the dispersion relation of an isothermal horizontally stratified medium (e.g., Gill 1982) can be derived from these equations by ignoring the gravity potential perturbation and using a flat Earth approximation for an isothermal atmosphere. Here we derive the differential equations for a fluid (eq. 2) from the basic physical principles.

The basic equations that govern the inviscid, adiabatic motions of a self–gravitating fluid are:

Momentum balance

$$\rho \frac{D^2\mathbf{u}}{Dt^2} = -\nabla P + \rho \mathbf{g}. \qquad 3$$

Equation of continuity

$$\delta\rho + \rho\nabla \cdot \mathbf{u} = 0. \qquad 4$$

The adiabatic equation of state for an ideal fluid

$$\delta\rho = \left(\frac{\partial\rho}{\partial P}\right)_S \delta P = \frac{\delta P}{c^2}. \qquad 5$$

The Poisson equation for gravitational potential

$$\nabla^2\phi = 4\pi\rho. \qquad 6$$

The definition of the gravity potential

$$\mathbf{g} = -\nabla\phi. \qquad 7$$

δ denotes the Lagrangian perturbation which is defined for a given parcel of the medium at $\mathbf{x}$ which was at $\mathbf{x_o}$ at $t = 0$. The Eulerian perturbation, denoted by $'$, is defined as a perturbation of a physical quantity at a given position $\mathbf{x_o}$. A physical quantity $f(\mathbf{x}, t)$ and its reference state $f_o(\mathbf{x})$ are therefore expressed by either

$$f(\mathbf{x}, t) = f_o(\mathbf{x}) + f'(\mathbf{x}, t) \qquad 8$$

or

$$f(\mathbf{x},t) = f_o(\mathbf{x_o}) + \delta f(\mathbf{x},t). \quad 9$$

Now consider small oscillations. The Lagrangian and Eulerian perturbations and derivatives are related to each other to the first order of $\mathbf{u}$ by

$$\delta f(\mathbf{x},t) = f'(\mathbf{x},t) + \mathbf{u}\cdot\nabla f_o(\mathbf{x},t) \quad 10$$

and by

$$\mathbf{x} = \mathbf{x_o} + \mathbf{u}, \quad 11$$

$$\frac{D}{Dt} = \frac{\partial}{\partial t} + \mathbf{u}\cdot\nabla. \quad 12$$

Subtracting the reference equations such as

$$-\nabla P_o + \rho_o \mathbf{g_o} = 0, \quad 13$$

$$\nabla^2\phi_o = 4\pi\rho_o \quad 14$$

and

$$\mathbf{g_o} = -\nabla\phi_o = -g_o\hat{r}, \quad 15$$

where $\mathbf{g_o} = (-g_o, 0, 0)$, and ignoring the second order of the displacement and perturbations, we obtain the equation of motion of the perturbed states

$$\rho_o\frac{\partial^2\mathbf{u}}{\partial t^2} + \nabla P' + \rho' g_o\hat{r} + \rho_o\nabla\phi' = 0, \quad 16$$

$$\delta\rho + \rho_o\nabla\cdot\mathbf{u} = \rho' + \nabla\cdot(\rho_o\mathbf{u}) = 0, \quad 17$$

$$\delta\rho = \frac{\delta P}{c^2}, \quad 18$$

$$\nabla^2\phi' = 4\pi G\rho'. \quad 19$$

Because $\delta P = P' + \mathbf{u}\cdot\nabla P_o = P' - u_r\rho_o g_o$ and $\rho' = \delta\rho - u_r\frac{d\rho}{dr}$, the vertical component of eq. 16 becomes

$$\rho_o\frac{\partial^2 u_r}{\partial t^2} + \frac{\partial\delta P}{\partial r} + \frac{g_o}{c^2}\delta P + \rho_o\frac{\partial(u_r g_o + \phi')}{\partial r} = 0. \quad 20$$

In spherical coordinates a vector spherical component (l, m) of the displacement $\mathbf{u}$ can be expressed as

$$\mathbf{u} = (U\hat{r} + \nabla_\perp V - \hat{r} \times \nabla_\perp W) Y_m^l(\theta, \varphi) e^{i\omega t}, \tag{21}$$

where

$$\nabla_\perp = (0, \frac{\partial}{\partial\theta}, \frac{1}{\sin\theta}\frac{\partial}{\partial\varphi}) \tag{22}$$

and $Y_m^l(\theta, \varphi)$ is the spherical harmonic function (e.g., Arfken, 1985). Because from eqs. 16–19 we find that the displacement $(\hat{r} \times \nabla_\perp W)$ does not result in any pressure, density and potential perturbations, the (l, m) component of the displacement is simply expressed at frequency ω as

$$\mathbf{u}(r, \theta, \varphi, t) = \left(U, V\frac{\partial}{\partial\theta}, \frac{V}{\sin\theta}\frac{\partial}{\partial\varphi}\right) Y_m^l(\theta, \varphi) e^{i\omega t} \tag{23}$$

and the Lagrangian pressure perturbation as

$$\delta P(r, \theta, \varphi, t) = Q\, Y_m^l(\theta, \varphi) e^{i\omega t} \tag{24}$$

and the Eulerian gravitational perturbation as

$$\phi'(r, \theta, \varphi, t) = \Phi\, Y_m^l(\theta, \varphi) e^{i\omega t}, \tag{25}$$

where $U(r), V(r), Q(r)$ and $\Phi(r)$ are functions of r. The vertical component of eq. 16 is written as

$$\left(-\omega^2\rho_o U + \frac{\partial Q}{\partial r} + \frac{g_o}{c^2}Q + \rho_o\frac{\partial(Ug_o + \Phi)}{\partial r}\right) Y_m^l(\theta, \varphi) e^{i\omega t} = 0. \tag{26}$$

By rewriting $\delta P = -c^2\rho_o\nabla \cdot \mathbf{u}$ and using

$$\nabla \cdot \mathbf{u} = \left(\frac{1}{r}\frac{\partial(r^2U)}{\partial r} - l(l+1)\frac{V}{r}\right) Y_m^l(\theta, \varphi) e^{i\omega t}, \tag{27}$$

we obtain

$$Q = -\kappa\left(2\frac{U}{r} + \frac{\partial U}{\partial r} - l(l+1)\frac{V}{r}\right), \tag{28}$$

where $\kappa = \rho_o c^2$ is the bulk modulus. The horizontal component of eq. 16 is written as

$$\left(-\omega^2 \rho_o V + \frac{1}{r}(Q + U\rho_o g_o + \rho_o \Phi)\right) \nabla_\perp Y_m^l(\theta, \varphi) e^{i\omega t} = 0. \tag{29}$$

From eqs. 17 and 19 we have

$$\nabla^2 \phi' = -4\pi G(\mathbf{u} \cdot \nabla \rho_o + \rho_o \nabla \cdot \mathbf{u}) \tag{30}$$

or

$$\frac{\partial^2 \Phi}{\partial r^2} + \frac{2}{r}\frac{\partial \Phi}{\partial r} - l(l+1)\frac{\Phi}{r^2} = -4\pi G\left(\rho_o(\frac{\partial U}{\partial r} + \frac{2U - l(l+1)V}{r}) + U\frac{\partial \rho_o}{\partial r}\right). \tag{31}$$

Introducing a new dependent variable defined as

$$Y_6 = \frac{\partial \Phi}{\partial r} + (l+1)\frac{\Phi}{r} + 4\pi G \rho_o U, \tag{32}$$

eq. 27 is expressed as

$$\frac{\partial Y_6}{\partial r} = \frac{1}{r}\left(-(l+1)4\pi G\rho_o U + l(l+1)4\pi G\rho_o V + (l-1)Y_6\right). \tag{33}$$

Using V from eq. 29,

$$V = \frac{1}{\omega^2 \rho_o r}(Q + \rho_o g_o U + \rho_o + \Phi), \tag{34}$$

we can eliminate V from eqs. 28 and 33. The results are

$$\frac{\partial U}{\partial r} = (-\frac{2}{r} + \frac{l(l+1)g_o}{\omega^2 r^2})U + (-\frac{1}{\kappa} + \frac{l(l+1)}{\omega^2 \rho_o r^2})Q + \frac{l(l+1)}{\omega^2 r^2}\Phi, \tag{35}$$

$$\frac{\partial Y_6}{\partial r} = 4\pi G\left(-\frac{(l+1)}{r} + \frac{l(l+1)\rho_o g_o}{\omega^2 r^2}\right)U + 4\pi G\frac{l(l+1)}{\omega^2 r^2}Q + 4\pi G\frac{l(l+1)\rho_o}{\omega^2 r^2}\Phi + \frac{(l-1)}{r}Y_6. \tag{36}$$

From the definition of Y_6,

$$\frac{\partial \Phi}{\partial r} = -4\pi G\rho_o U + \frac{l+1}{r}\Phi + Y_6. \tag{37}$$

From eqs. 14 and 15 we find that the reference gravity and density are related by

$$\frac{\partial g_o}{\partial r} = 4\pi g_o \rho_o - \frac{2}{r} g_o. \tag{38}$$

By eliminating $\frac{\partial U}{\partial r}$, $\frac{\partial g_o}{\partial r}$ and $\frac{\partial \Phi}{\partial r}$ from eq. 26, we obtain

$$\begin{aligned} \frac{\partial Q}{\partial r} = & \left(\omega^2 \rho_o - \frac{l(l+1)}{\omega^2 r^2} \rho_o {g_o}^2 + 4\frac{\rho_o g_o}{r} \right) U - \frac{l(l+1) g_o}{\omega^2 r^2} Q \\ & + \left(-\frac{\rho_o g_o l(l+1)}{\omega^2 r^2} + \frac{l+1}{r} \right) \Phi - \rho_o Y_6. \end{aligned} \tag{39}$$

The redefined variables $Y_1 = U$, $Y_2 = -Q$, $Y_5 = \Phi$ and Y_6 are then the same variables defined in Takeuchi and Saito (1972) except that the sign of the potential perturbation is opposite. The four simultaneous first order differential equations (eqs. 35, 36, 37 and 39)

$$\frac{d}{dr} \begin{pmatrix} Y_1 \\ Y_2 \\ Y_5 \\ Y_6 \end{pmatrix} = \mathbf{B} \begin{pmatrix} Y_1 \\ Y_2 \\ Y_5 \\ Y_6 \end{pmatrix}, \tag{40}$$

where B_{ij}'s are given by

$$\begin{pmatrix} -\frac{2}{r} + \frac{l(l+1) g_o}{\omega^2 r^2} & \frac{1}{\kappa} - \frac{l(l+1)}{\omega^2 \rho_o r^2} & \frac{l(l+1)}{\omega^2 r^2} & 0 \\ -\omega^2 \rho_o + \frac{l(l+1)}{\omega^2 r^2} \rho_o {g_o}^2 - 4\frac{\rho_o g_o}{r} & -\frac{l(l+1) g_o}{\omega^2 r^2} & \frac{\rho_o g_o l(l+1)}{\omega^2 r^2} - \frac{l+1}{r} & \rho_o \\ -4\pi G \rho_o & 0 & -\frac{l+1}{r} & 1 \\ 4\pi G \left(-\frac{(l+1)}{r} + \frac{l(l+1)\rho_o g_o}{\omega^2 r^2} \right) & -4\pi G \frac{l(l+1)}{\omega^2 r^2} & 4\pi G \frac{l(l+1)\rho_o}{\omega^2 r^2} & \frac{(l-1)}{r} \end{pmatrix} \tag{41}$$

are the governing equations of eigenfunctions in a fluid region (Takeuchi and Saito, 1972). Further, we change the dependent variables from Y_i's to Z_i's by

$$Z_1 = rY_1 = rU, \tag{42}$$

$$Z_2 = rY_2 = -rQ, \tag{43}$$

$$Z_5 = rY_5 = r\Phi, \tag{44}$$

$$Z_6 = \frac{rY_6}{4\pi G} = \frac{1}{4\pi G} \left(r\frac{\partial \phi}{\partial r} + (l+1)\Phi \right) + \rho_o r U. \tag{45}$$

Then the coefficient matrix in eq. 41 is transformed into the one in eq. 2. The system of the differential equations improves its symmetry and, together with appropriate

boundary conditions, becomes self-adjoint (Saito, 1988; Woodhouse, 1988). If we use the Eulerian pressure perturbation, which is customary in the literature for the oscillations of stars, the coefficient matrix of the differential equations contains the radial gradient of stellar model parameters (Ledoux and Walraven 1958, Cox 1980, Unno *et. al.* 1989) and the differential equations are not self-adjoint.

2.2 Local behavior of eigenfunctions

In the short wavelength limit, the effect of gravity on the equation of motion can be ignored and the local behavior of an eigenfunction of sound waves $e^{i(k_x x + k_z z)}$ is expressed by

$$k_x{}^2 + k_z{}^2 = \frac{\omega^2}{c^2} \tag{46}$$

and

$$k_x{}^2 = \frac{l(l+1)}{r^2}. \tag{47}$$

For a given frequency, sound velocity, angular order number and position r, $k_z{}^2$ can be negative, then waves are exponentially growing or decreasing in the z direction. If $k_z{}^2$ is positive, waves are propagating in the z direction. At low frequency gravity plays an important role. For atmospheric waves, the gravity perturbation caused by the density variation is very small compared to the reference gravity, elasticity and buoyancy forces. We ignore the gravity potential perturbation but include the reference gravity g_o (Cowling 1941). The differential equations then become

$$\frac{d}{dr}\begin{pmatrix} Z_1 \\ Z_2 \end{pmatrix} = \begin{pmatrix} -\frac{1}{r} + \frac{l(l+1)g_o}{\omega^2 r^2} & \frac{1}{\kappa} - \frac{l(l+1)}{\omega^2 \rho_o r^2} \\ -\omega^2\rho_o + \frac{l(l+1)}{\omega^2 r^2}\rho_o g_o{}^2 - 4\frac{\rho_o g_o}{r} & \frac{1}{r} - \frac{l(l+1)g_o}{\omega^2 r^2} \end{pmatrix}\begin{pmatrix} Z_1 \\ Z_2 \end{pmatrix}. \tag{48}$$

The vertical variation of P_o and ρ_o define a local scale height H_s given by

$$H_s = -\frac{dr}{d\ln P_o} \sim -\frac{dr}{d\ln \rho_o}. \tag{49}$$

Through the middle and lower atmosphere, 6.4 km $< H_s <$ 8.4 km at $0 < z <$ 86 km and $H_s \sim$ 50 km at $z \sim$ 300 km (Gill, 1982). In order to examine the local behavior of

eigenfunctions from the coefficient matrix, the rapid change of the coefficient matrix as a function of radius is not desirable. Because ρ_o, κ are the most rapidly changing variables in eq. 48, and radial gradient of g_o is much smaller, the vertical scale length of the B_{12} and B_{21} terms is about that of ρ_o or κ, or from eq. 49, H_s. On the other hand the vertical scale length of the eigenfunctions can be as large as $\sim$ 100 km thickness of the atmospheric layer.

Here we introduce non–dimensional quantities which are finite as r approaches $r = R$ where the boundary condition is imposed. Following Unno *et al.* (1989), the non–dimensional numbers, U_m, V_g, c_1, σ are

$$U_m = \frac{d \ln M_r}{d \ln r} = \frac{4\pi\rho_o r^3}{M_r} = \frac{3\rho_o}{\bar{\rho}}, \tag{50}$$

$$V_g = \frac{g_o r}{c^2} = \frac{GM_r}{c^2 r} = \frac{r}{\Gamma H_s}, \tag{51}$$

$$c_1 = \frac{r^3 M}{R^3 M_r} = \frac{\bar{\rho}(R)}{\bar{\rho}(r)}, \tag{52}$$

$$\omega^2 = \frac{GM}{R^3}\sigma^2, \tag{53}$$

where

$$M_r = \int_0^r \rho_o(r) 4\pi r^2 dr, \tag{54}$$

$$\bar{\rho}(r) = \frac{M_r}{\frac{4}{3}\pi r^3}, \tag{55}$$

$$g_o(r) = \frac{GM_r}{r^2}, \tag{56}$$

$$\frac{r}{g_o}\frac{dg_o}{dr} = \frac{4\pi\rho r^3}{M_r} - 2 = U_m - 2, \tag{57}$$

$$\rho_o = U_m \frac{M_r}{4\pi r^3}. \tag{58}$$

Here we have used the definition of the scale height

$$H_s = -\frac{dr}{d \ln P_o} \tag{59}$$

and Γ is defined by

$$\Gamma = \frac{\rho_o}{P_o}\left(\frac{\partial P}{\partial \rho}\right)_s. \tag{60}$$

G, M, R and σ^2 are constants, and M_r, U_m, c^2 and c_1 are functions of r. We can rewrite eq. 48 using the dimensionless numbers

$$\frac{d}{dr}\begin{pmatrix} Z_1 \\ Z_2 \end{pmatrix} = \begin{pmatrix} -\frac{1}{r} + \frac{l(l+1)}{c_1\sigma^2 r} & \frac{4\pi R^6}{GU_m M^2 r^2}\left(c_1^2 V_g - \frac{l(l+1)c_1}{\sigma^2}\right) \\ \frac{GU_m M^2}{4\pi R^6}\left(\frac{-\sigma^2}{c_1} + \frac{l(l+1)}{\sigma^2 c_1^3} - \frac{4}{c_1^2}\right) & \frac{1}{r} - \frac{l(l+1)}{\sigma^2 c_1 r} \end{pmatrix}\begin{pmatrix} Z_1 \\ Z_2 \end{pmatrix}. \tag{61}$$

Changing the dependent variables from (Z_1, Z_2) to (X_1, X_2) which are defined by

$$X_1 = Z_1 = rU, \tag{62}$$

$$X_2 = \frac{Z_2}{\rho_o g_o} = \frac{4\pi c_1 R^6}{GU_m r M^2} Z_2, \tag{63}$$

we obtain

$$\begin{aligned} r\frac{d}{dr}\begin{pmatrix} X_1 \\ X_2 \end{pmatrix} &= \begin{pmatrix} -1 + \frac{l(l+1)}{c_1\sigma^2} & c_1 V_g - \frac{l(l+1)}{\sigma^2} \\ -\sigma^2 + \frac{l(l+1)}{\sigma^2 c_1^2} - \frac{4}{c_1} & 3 + K - U_m\frac{l(l+1)}{\sigma^2 c_1} \end{pmatrix}\begin{pmatrix} X_1 \\ X_2 \end{pmatrix} \\ &= C\begin{pmatrix} X_1 \\ X_2 \end{pmatrix} \end{aligned} \tag{64}$$

where

$$K = -\frac{d\ln\rho_o}{dr} r = \frac{r}{H_s}. \tag{65}$$

Now in the coefficient C_{ij} for X_1 and X_2, rapidly changing model parameters ρ_o and κ disappear and only c_1, V_g, K and U_m which change slowly with r exist. Hereafter we assume that the change of the C_{ij} is so small compared to the change of eigenfunctions X_1 and X_2 that the C_{ij}'s are locally constant. In the atmosphere c_1 is close to 1, U_m is close to zero and V_g has a finite value of the order of 100 to 1000. Since $f(r) = r^a$ is the solution of a $rdf(r)/dr = af(r)$ type differential equation, we assume X_1 and X_2 locally depend on radius as r^λ. Then the characteristic equation for eq. 64 is

$$\lambda^2 - (2+K)\lambda - \left(\frac{l(l+1)}{\sigma^2} - V_g\right)(\sigma^2 - K + V_g) - (V_g^2 - V_g(K+4) + 3 + K) = 0 \tag{66}$$

and its solutions are

$$\lambda_{\pm} = \frac{1}{2}\left(2 + K \pm \sqrt{\gamma}\right), \tag{67}$$

where

$$\gamma = (K - 2V_g + 4)^2 + 4\left(\frac{l(l+1)}{\sigma^2} - V_g\right)(\sigma^2 - K - V_g). \tag{68}$$

Here we have replaced c_1 by 1 and U_m by 0. Using the normalized buoyancy frequency A^*

$$\begin{aligned} A^* &= \frac{N^2 r}{g_o} = -\left(\frac{r}{\rho_o}\frac{d\rho_o}{dr} + \frac{g_o r}{c^2}\right) \\ &= K - V_g, \end{aligned} \tag{69}$$

where N is the buoyancy frequency (or Brunt Väisälä frequency), γ is expressed as

$$\gamma = (A^* - V_g + 4)^2 + 4\left(\frac{l(l+1)}{\sigma^2} - V_g\right)(\sigma^2 - A^*). \tag{70}$$

Unno *et al.* (1989), who used the Eulerian pressure perturbation as a dependent variable instead of the Lagrangian pressure perturbation, reached the same characteristic equation. In this characteristic equation the radial gradient of model parameters is indeed included through $K = r/H_s$. The energy density of a mode, $E = \rho_o(\frac{\partial \mathbf{u}}{\partial t}) \cdot (\frac{\partial \mathbf{u}}{\partial t})^{\dagger} = \rho_o|\omega|^2|\mathbf{u}|^2$, is given by

$$\begin{aligned} E &= \rho_o|\omega^2|(|U|^2 + l(l+1)|V|^2)Y_l^m(\theta,\varphi)^{\dagger}Y_l^m(\theta,\varphi) \\ &\propto \rho_o|\omega|^2\left(\frac{|X_1|^2}{r^2} + \frac{l(l+1)}{r^2\sigma^4}(|X_1 - X_2|)^2\right) \\ &\propto r^{-K-2} \quad r^{2\lambda_{\pm}} \\ &= r^{\pm\sqrt{\gamma}}. \end{aligned} \tag{71}$$

If $\gamma > 0$ two solutions of the growing and decreasing modal energy with altitude exist. This type of mode is called an evanescent mode. At the top boundary the solution of the growing modal energy is rejected and the modal energy decreases exponentially with altitude near the top. If $\gamma < 0$ the solutions associated with λ_+ and λ_- represent waves whose vertical phase velocity is downward and upward, respectively, because

eigenfunctions have time dependence $e^{i\omega t}$ and their radial dependence, near $r = r_o$, can be approximated by

$$r^{\sqrt{\gamma}} \propto e^{\frac{r}{r_o}\sqrt{\gamma}}. \tag{72}$$

The power of the exponential form in eq. 72 is determined so that at $r = r_0$, two functions have the same value and gradient. This type of mode is called a propagating mode. For a given atmospheric model, γ is a function of local model parameters and the period and the horizontal wavelength of the mode, and can be written as

$$\begin{aligned}\gamma &= -\frac{4V_g}{\sigma^2}\left(\left(\sigma^2 - \frac{l(l+1)}{V_g}\right)(\sigma^2 - K + V_g) - (K - 2V_g + 4)^2\frac{\sigma^2}{4V_g}\right) \\ &= -\frac{4V_g}{\sigma^2}(\sigma^2 - \sigma_1^2)(\sigma^2 - \sigma_2^2).\end{aligned} \tag{73}$$

σ_1 and σ_2 are the roots of the right–hand side of eq. 73. Because $\frac{l(l+1)}{V_g} > 0$, $\frac{(K-2V_g+4)^2}{4V_g} > 0$ and for a stably stratified fluid

$$K - V_g = A^* = \frac{N^2 r}{g_o} > 0 \tag{74}$$

holds, the two positive real frequencies σ_1 and σ_2 ($\sigma_1 < \sigma_2$) always exist for any subadiabatic atmospheric model. Waves are evanescent for $\sigma_2 > \sigma > \sigma_1$ and are propagating vertically for $\sigma_2 < \sigma$ or $\sigma_1 > \sigma$. We have the following asymptotic values of the boundaries ($\gamma = 0$) between the propagating region and the evanescent region:

$$\begin{aligned} &l \to 0, \quad {\sigma_1}^2 \to 0, \quad {\sigma_2}^2 \to A^* + \tfrac{(A^* - V_g + 4)^2}{4V_g} \\ &l \to \infty, \quad {\sigma_1}^2 \to A^*, \quad\quad {\sigma_2}^2 \to \tfrac{l(l+1)}{V_g} \end{aligned} \tag{75}$$

or

$$\begin{aligned} &l \to 0, \quad {\omega_1}^2 \to 0, \quad {\omega_2}^2 \to N^2 + c^2\left(\tfrac{1}{2H_s} - \tfrac{g_o}{c^2} + \tfrac{2}{R}\right)^2 \\ &l \to \infty, \quad {\omega_1}^2 \to N^2, \quad\quad {\omega_2}^2 \to \tfrac{l(l+1)c^2}{R^2} \end{aligned} \tag{76}$$

These local cutoff frequencies are the same as those of an isothermal atmosphere (e.g., Gill 1982) if $R \gg H_s$.

$$\begin{aligned} &k_h \to 0, \quad \omega_1^2 \to 0, \quad \omega_2^2 \to N^2 + c^2\left(\tfrac{1}{2H_s} - \tfrac{g_o}{c^2}\right)^2 = \left(\tfrac{c}{2H_s}\right)^2 = {N_A}^2 \\ &k_h \to \infty, \quad \omega_1^2 \to N^2, \quad\quad\quad\quad \omega_2^2 \to c^2{k_h}^2 \end{aligned} \tag{77}$$

where N_A is the acoustic cutoff frequency and k_h is the horizontal wavenumber.

The rate of vertical flow of energy per unit area, F_r, is given by (Gill 1982, eq. 4.6.4) the radial component of the real part of

$$\mathbf{F} = (p' + \frac{1}{2}|\mathbf{v}|^2)\mathbf{v}^\dagger, \tag{78}$$

where $\mathbf{v} = \frac{D\mathbf{u}}{Dt}$. For a small oscillation, F_r is approximated by $F_r = p'(\frac{\partial u_r}{\partial t})^\dagger$

$$\begin{aligned} Re(F_r) &= Re\,(-i\omega p' u_r) \\ &\propto -i\omega \frac{\rho_o g_o}{r^2}(X_1 X_1^\dagger - X_2 X_1^\dagger) \\ &= -i\omega \frac{\rho_o g_o}{r^2}(V_g - 1 - \lambda_\pm)|X_1|^2 \\ &\propto -Im(\lambda_\pm) \\ &\propto -Im(\pm\sqrt{\gamma}), \end{aligned} \tag{79}$$

where the upper and lower signs correspond to the λ_+–solution and λ_-–solution, respectively. Here we have used eq. 64 to eliminate X_2 and the polynomial expression of X_1. Now we consider the energy leak of propagating waves. In order to be a decaying oscillation, the square of the complex eigenfrequency $s_1 + s_2 i = \sigma^2$ requires $s_1 \gg s_2 > 0$. Going back to the definition in eq. 68, the imaginary part of γ is given by

$$Im(\gamma) = 4s_2 \left(-V_g + \frac{l(l+1)}{\sigma^2 \sigma^{2\dagger}} A^*\right). \tag{80}$$

When $V_g > \frac{l(l+1)}{\sigma^2\sigma^{2\dagger}}A^*$ or equivalently $|\omega|^2 > L_l N$, $Im(\gamma) = 2Re(\sqrt{\gamma})Im(\sqrt{\gamma})$ is negative, where L_l, called the Lamb frequency in Unno *et al.* (1989), is defined by

$${L_l}^2 = \frac{l(l+1)}{r^2}c^2. \tag{81}$$

If $Re(\sqrt{\gamma}) > 0$ and $Im(\sqrt{\gamma}) < 0$, a λ_+ or λ_-–solution has both phase velocity and energy flux upward, or both phase velocity and energy flux downward, respectively. If $Re(\sqrt{\gamma}) < 0$ and $Im(\sqrt{\gamma}) > 0$, a λ_+ or λ_-–solution has both phase velocity and energy flux downward, or both phase velocity and energy flux upward, respectively. In both cases, since we reject the solution with downward energy flow, an appropriate solution

always has an upward phase velocity. Similarly, when $V_g < \frac{l(l+1)}{\sigma^2\sigma^{2\dagger}}A^*$ or equivalently $|\omega|^2 < L_l N$, $Im(\gamma) = 2Re(\sqrt{\gamma})Im(\sqrt{\gamma})$ is positive, an appropriate solution always has a downward phase velocity.

In summary, acoustic modes ($\omega > \omega_2$), which approach the sound waves in the short horizontal wavelength limit, have an upward phase velocity and upward energy transport. Evanescent modes ($\omega_2 > \omega > \omega_1$) have zero upward phase velocity and no vertical energy transport. Gravity modes ($\omega_1 > \omega$), whose eigenperiod approach the buoyancy frequency in the short wavelength limit, have a downward phase velocity and upward energy transport. The locally defined quantity γ diagnoses the local behavior of waves in the vertical direction for a given period and horizontal wavelength. In the region where γ is negative, waves are trapped or propagating depending on the boundary condition. In the region where γ is positive, waves become evanescent and the modal energy density decays or increases exponentially in the vertical direction. This is valid when the vertical scale length of waves is shorter than that of γ. As the vertical scale length of γ approaches the vertical wavelength of atmospheric waves, this statement becomes less accurate.

2.3 Computation of normal modes

2.3.1 Conventional upper boundary conditions

Under the Cowling approximation, the free upper boundary condition is satisfied by setting Z_2 to zero, and the non–vertical displacement boundary condition is satisfied by setting Z_1 to zero. When the gravitational potential perturbation is included, an additional boundary condition $Z_6 = 0$ must be imposed. The determinant of the two sets of dependent solutions at the boundary is computed. The boundary condition is satisfied when the determinant vanishes (Takeuchi and Saito, 1972).

2.3.2 Radiation upper boundary condition

For an evanescent mode with $\omega_2 > \omega > \omega_1$

$$(C_{11} - \lambda_-)Z_1 + C_{12}\frac{Z_2}{\rho_o g_o} = 0 \qquad 82$$

or

$$C_{21}Z_1 + (C_{22} - \lambda_-)\frac{Z_2}{\rho_o g_o} = 0 \qquad 83$$

is the boundary condition. The eigenfrequency and eigenfunctions are real. For an acoustic mode with $\omega > \omega_2$ or a gravity mode with $\omega < \omega_1$,

$$(C_{11} - \lambda)Z_1 + C_{12}\frac{Z_2}{\rho_o g_o} = 0 \qquad 84$$

or

$$C_{21}Z_1 + (C_{22} - \lambda)\frac{Z_2}{\rho_o g_o} = 0 \qquad 85$$

is the boundary condition. The eigenfrequency and the eigenfunctions become complex. We choose $\lambda = \lambda_+$ or λ_- to satisfy the radiation boundary condition that inhibits downward energy flow through the upper boundary. If we define $\sqrt{\gamma}$ with $Im(\sqrt{\gamma}) \geq 0$, from the discussion in section 1.2, λ_- is the appropriate boundary condition for acoustic modes, and λ_+ is the appropriate boundary condition for gravity modes. The boundary condition for the propagating modes is treated a little differently in Unno *et al.* (1989). They set the boundary condition where modal energy density E in eq. 71 does not grow or decay locally by adjusting the value of $\lambda_\pm$. Their set of complex eigenfrequency σ, complex γ and complex λ do not satisfy the characteristic equation (eqs. 66, 67 and 68).

2.3.3 Lower boundary conditions

For atmospheric modes, the bottom ground surface is assumed rigid by setting Z_1 to 0. For modes whose eigenfunctions start beneath the ocean or ground surface,

such as seismic Rayleigh waves and the modes for an Earth model including the atmosphere, the boundary values of eigenfunctions at a starting level are obtained from the analytic solution of an isotropic homogeneous fluid or solid body whose model parameters are the same as those at the boundary (Pekeris and Jarosh 1958, Takeuchi and Saito 1972). The appropriate starting level of the integration is where the amplitudes of the eigenfunctions become so small that the ratio of amplitude at the starting level relative to the maximum amplitude reaches a pre-set computational accuracy. Such a staring level is roughly estimated by integrating the radial wavenumber of a mode from the starting level to the turning level of the corresponding seismic ray.

2.3.4 Integration

We use a shooting method to compute the normal modes. The differential equations for a fluid body (eq. 37) are integrated from a starting level to a boundary level. The compound–matrix method (Takeuchi and Saito, 1972), or equivalently the minors method (Woodhouse, 1988), is not used. In a solid the equations of motion are reduced to six, or four if the Cowling approximation is used, simultaneous first order differential equations. The continuation of eigenfunctions at the solid–fluid boundary is described in Takeuchi and Saito (1972). The complex eigenfrequencies and eigenfunctions are obtained by a complex root search similar to the one used by Friedman (1966). We employ an adaptive step size control Runge–Kutta integrator (Press *et al.*, 1992). Model parameters are given as a table at discrete points. Between the grid points the model parameters are linearly interpolated. Since the program controls the integration step size, a uniform accuracy of the eigenfunctions can be maintained easily. For an eigenfunction with the free surface boundary or rigid boundary condition, the integration is crudely checked by the energy integrals.

When the integration is performed in a relatively thick region where γ has large positive values and the modal energy is decreasing in the direction of integration, the

differential equation becomes stiff and the integration becomes numerically unstable because the unwanted solution grows exponentially. However, the eigenvalue is accurately computed for this distorted eigenfunction because this growing component is the other solution with the same eigenvalue (Jensen *et al.*, 1994). For gravity modes with large angular order numbers, the modal energy is trapped sometimes locally, e.g., near the mesopause, and the oneway integration becomes unstable. For these cases we integrate from the bottom boundary upward and from the top boundary downward and match the two sets of eigenfunctions at a level where the modal energy is trapped. For low order acoustic modes we can stably integrate both upward and downward by the adaptive step size Runge–Kutta integration because $|\gamma|$ is relatively small. The group velocity is obtained by numerical differentiation along the modal branch or, if the boundary condition is free or rigid, by integral relations (Takeuchi and Saito, 1972).

3. Normal modes in the atmosphere

Figure 1 shows the acoustic velocity profile of the atmosphere model used in this study. The sound velocity is computed from the temperature and the pressure by $c^2 = \Gamma P_o/\rho_o$. We assume that Γ is constant, 1.4, the value for ideal diatomic molecule gas. Figure 2 shows the normal modes for the atmosphere model. The cutoff frequencies computed at z=100 km and 200 km are plotted in Figure 3. In the non–rotating spherically symmetric atmosphere, three types of waves exist, acoustic waves, Lamb waves and internal gravity waves. Many references on atmospheric acoustic waves, the Lamb waves and internal gravity waves can be found in, for example, Beer (1974) and Georges (1968). The group velocity of a mode can be roughly obtained from the slope of the branch in the $(\omega - k)$ plot. All the computed normal modes for the atmosphere fall into these three categories except one surface gravity wave, or deep–water–wave–like branch in the atmosphere which is an artifact

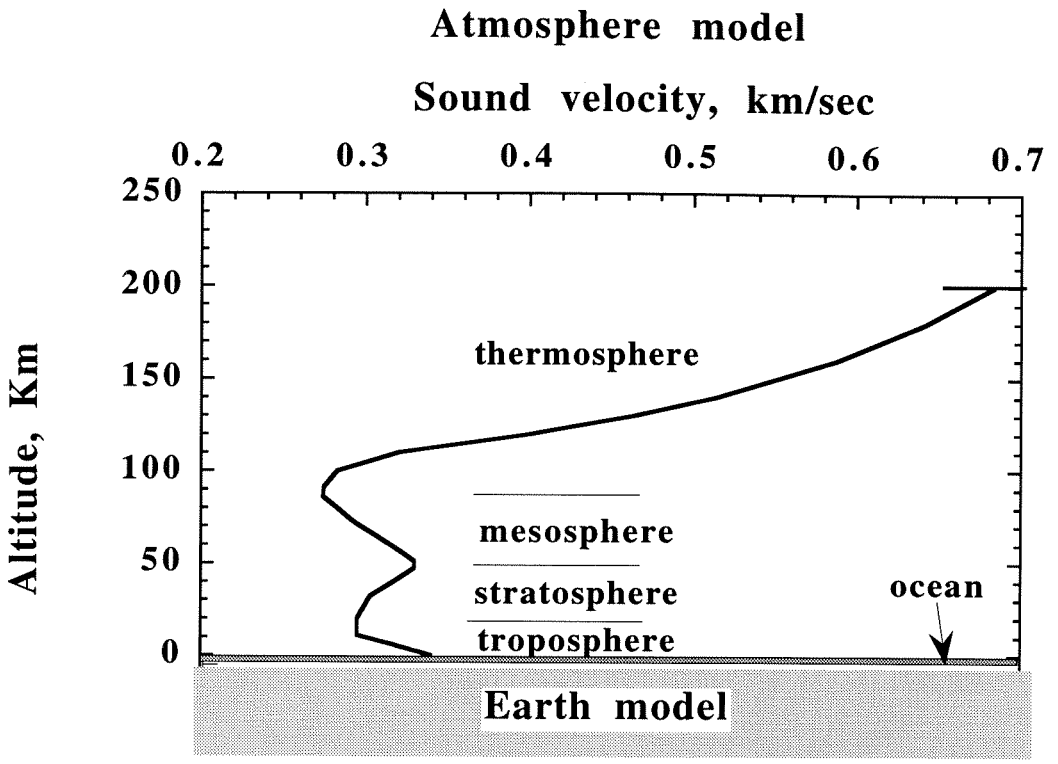

Figure 1. Atmospheric model used in this study, U.S. standard atmosphere 1976. Atmospheric density decreases quickly upward with a scale height of about 7 km. At 100 km, the density is about one millionth of the ground atmospheric density. The exospheric temperature of U.S. 1976 standard atmosphere approaches 1000 K.

(a)

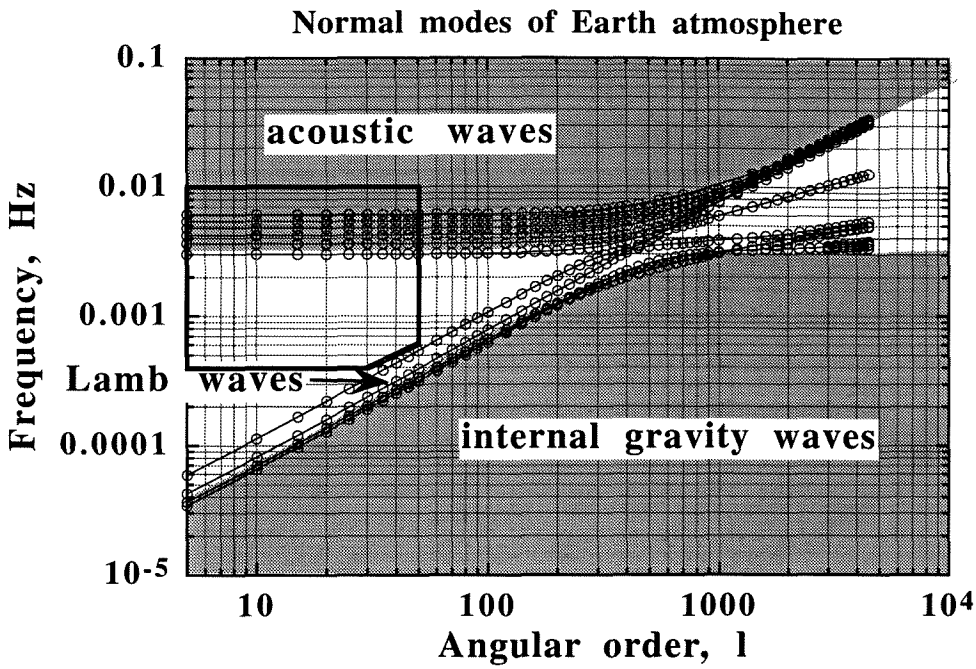

Figure 2. Normal modes of the atmosphere model in Figure 1. The top boundary at 200 km is a stress free surface boundary and the bottom is a rigid boundary. Three major groups of eigenmodes exist. Acoustic modes are the sound waves in the atmosphere. Gravity modes exist for a fluid body under gravity with subadiabatic density stratification, such as the Earth's atmosphere. Lamb waves are boundary waves which travel along the ground with the speed of sound. (a) Angular order vs. frequency plot. The boxed region is magnified in Figure 7. (b) Period vs. phase velocity plot for comparison with early studies. The horizontal phase velocity is computed by $\omega r_e/(l+0.5)$, where r_e=6371 km.

(b)

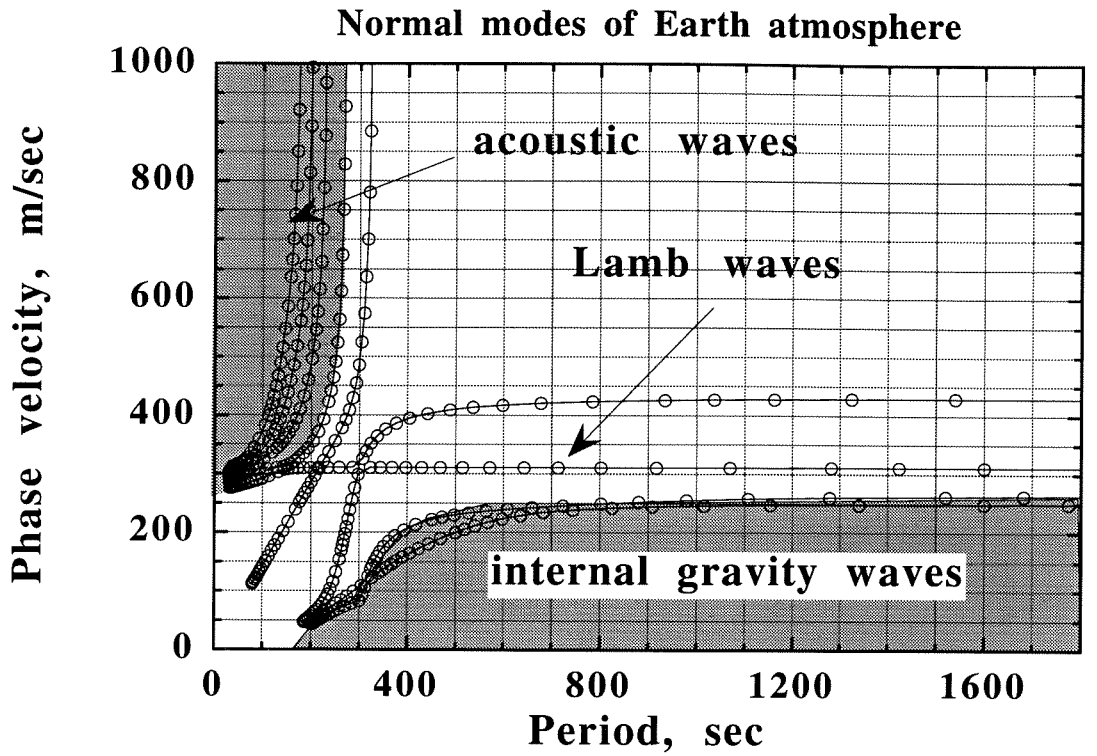
Normal modes of Earth atmosphere
Phase velocity, m/sec
1000
800
600
400
200
0
0
400
800
1200
1600
Period, sec
acoustic waves
Lamb waves
internal gravity waves

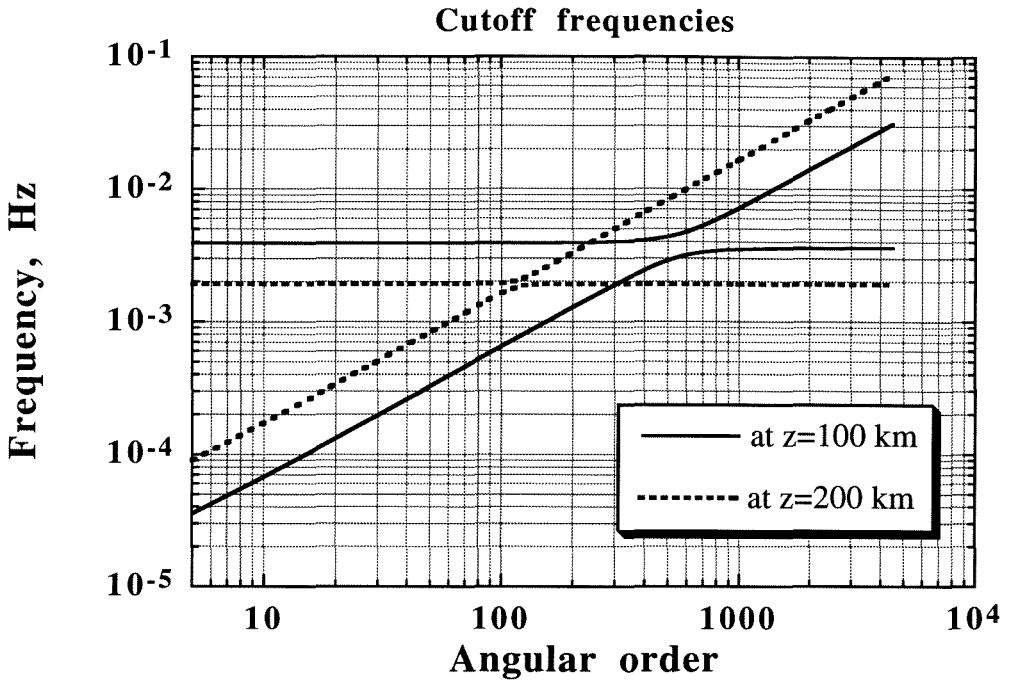

Figure 3. Cutoff frequencies ω_1 and ω_2 ($\omega_1 < \omega_2$) for the U.S. standard atmosphere computed at z=100 km and 200 km. In the region where $\omega_2 > \omega > \omega_1$, waves become evanescent. In the region where $\omega > \omega_2$ or $\omega < \omega_1$, propagating waves exist.

of the free surface boundary (Figure 2).

In the frequency band in which the harmonic seismic surface waves were observed during the eruption of Mt. Pinatubo, about 200~300 s, all three types of atmospheric waves can exist. They are long wavelength acoustic waves near the acoustic cutoff frequency, Lamb waves and short wavelength gravity waves near the buoyancy frequency, or the Brunt-Väisälä frequency. Kanamori *et al.* (1994) suggested that the acoustic modes near the acoustic cutoff frequency and the gravity modes near the buoyancy frequency can be excited efficiently by a volcanic eruption. For the long wavelength acoustic modes near the acoustic cutoff, the longer the wavelength, the larger the phase velocity and the smaller the group velocity. For example, at angular order 30 or horizontal wavelength 1300 km, the gravest three acoustic modes have a horizontal phase velocity of about 4~5 km/s and a horizontal group velocity of about 10 m/s. Short wavelength gravity modes, for example at l=2000, near the cutoff have small horizontal phase velocity $\leq$ 100 m/s and horizontal group velocity $\geq$ 10 m/s.

The propagation and excitation of these atmospheric pressure waves from natural sources such as the Great Siberian meteorite of 1908 (Pekeris, 1939), the explosion of the Krakatoa volcano in 1883 (Pekeris, 1948; Harkrider and Press, 1967; Press and Harkrider, 1966), the 1964 great Alaskan earthquake (Mikumo, 1968), the 1980 eruption of Mt. St. Helens (Mikumo and Bolt, 1985), from the detonations of nuclear bombs in the atmosphere (e.g, Georges, 1968; Pierce and Posey, 1970), have been studied. However, none of these reported harmonic oscillations of pressure.

Benioff *et al.* (1951) reported harmonic oscillations in microbarograph records with a very short period of about 1 s after a natural earthquake at a regional distance. The waveforms in the farfield barographic records were dominated by the Lamb waves, which propagate at the speed of sound. A few branches of acoustic and gravity modes, whose group and phase velocities are close to the sound velocity in the atmosphere,

are required in the computation to simulate the barographic observations (Harkrider 1964).

Kanamori and Mori (1992) and Kanamori *et al.* (1994) reported harmonic barographic pressure changes recorded during the eruptions of Krakatoa 1883, Mt. St. Helens 1980 and Mt. Pinatubo 1991. Table 1 summarizes harmonic oscillations found in barograms and seismograms during these major volcanic eruptions.

The modal energy density of long wavelength (l=30, wavelength=1300 km) acoustic modes near the cutoff frequency is shown in Figure 4. The gravest mode with a period of 329 s has its energy only in the thermosphere. For this period and horizontal wavelength, a standing or propagating waves may exist in the thermosphere and the troposphere where γ is negative. To have a standing wave in a negative γ 'well', we require from eq. 72

$$h\frac{\sqrt{-\bar{\gamma}}}{r_o} = n\pi, \qquad 86$$

where $\bar{\gamma}$ is the average of γ in the negative–γ region, h is the vertical extent of the negative region and n is a positive integer. The negative γ region in the troposphere does not contain a standing wave because the vertical scale of the troposphere is too small to have a standing wave in this region and only a propagating wave exists in the thermosphere for this model. When we take the boundary at z=100 km, this mode disappears.

The second gravest mode with a period of 274 s, which is close to one of the observed periods (Table 1), is a trapped mode. The positive γ region in the mesopause, the low velocity channel which forms the boundary region between the thermosphere and mesosphere, works as a wave–reflecting wall for this mode and the modal energy is trapped below the mesopause and above the ground (Figure 1).

The third gravest mode with a period of 236 s, which is also close to one of the observations, has a large energy concentration below the thermosphere where

Eruption	Period	Observation Method	Distance
1991 Pinatubo	270 s, 230 s	seismograph	teleseism
1982 El Chichón	195 s, 266 s	seismograph	teleseism
1980 Mt. St. Helens	$\sim$ 300 s	seismograph worked as barograph	near source
1883 Krakatoa	$\sim$ 300 s	barograph	near source

Table 1. Observations of harmonic atmospheric oscillations and harmonic ground motion during major volcanic eruptions. Compiled by Kanamori *et al.* (1994).

γ has larger negative values than in the upper atmosphere. Because γ is negative everywhere, the modal energy can leak into the upper atmosphere. For this type of mode a radiation boundary condition is necessary. The energy distribution of higher frequency acoustic modes changes with altitude like a $\cos^2$ standing–wave type oscillation. This standing wave type oscillation is an artifact caused by the reflection at the free surface boundary and the modal energy will smoothly propagate upward or downward through the boundary if we remove the reflecting boundary at the top. The oscillation of trapped modes represents the reverberation of sound waves in the γ negative well and may be a source of the temporal harmonic loading on the ground. At higher frequencies, because upward short period acoustic waves do not come down by reflection, acoustic reverberation in the atmosphere may not exist and cannot be a source of harmonic loading. The harmonic ground motions with periods of 270 s and 230 s recorded on seismograms throughout the world may correspond to trapped acoustic modes that coupled to the ground.

The short wavelength gravitational modes (l=2000, wavelength=20 km) (Figure 4) have concentrated modal energy at higher altitude near z=100 km except one mode. The mode with a period of 300 s has energy concentration in the stratosphere. A low altitude source such as a volcanic eruption may preferentially excite this mode and the periodic pressure change with a period of 300 s may be recorded at the ground level. Because of its small group velocity, the pressure change associated with this gravity mode will be observed near the volcano. The atmospheric oscillation with a period near 300 s observed by a seismometer which worked as a barograph near Mt. St. Helens just after the explosive eruption in 1980 may be this type of gravity mode trapped in the stratosphere. A satellite infrared image of Mt. Pinatubo during the 1991 eruption shows (Kanamori *et al.* 1994, figure 11) a concentric pattern of temperature disturbance with wavelength of several tens of kilometers around the

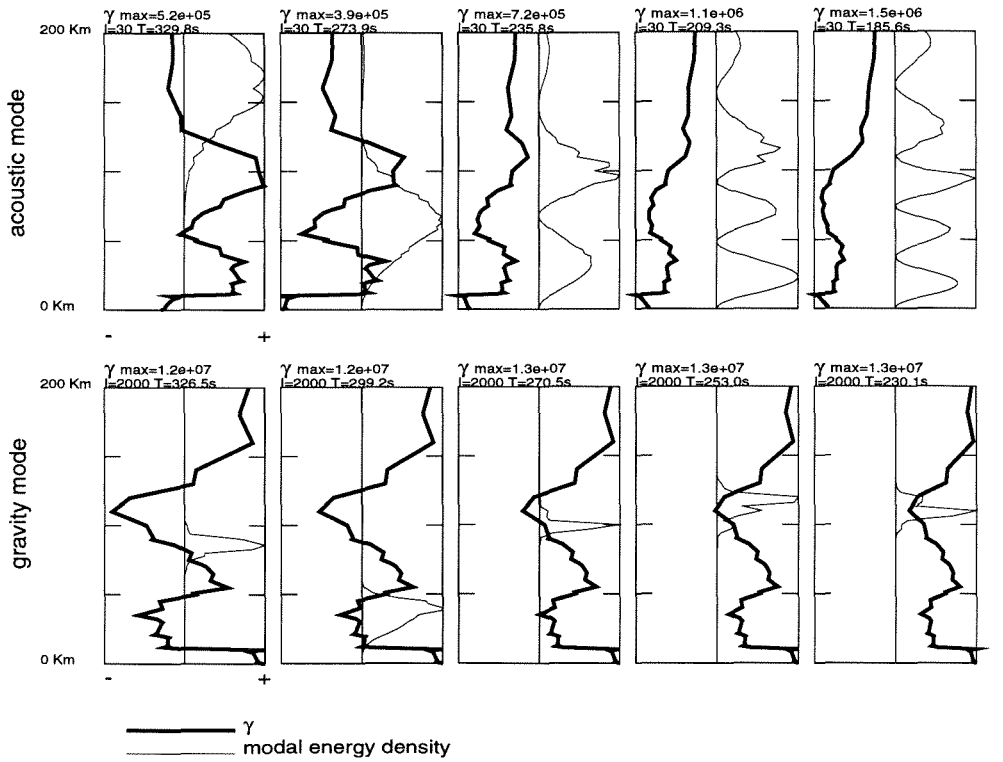

Figure 4. Modal energy density $\rho_o(|U|^2 + l(l+1)|V|^2)r^2$ of acoustic modes l=30 and gravity modes l=2000 with a period of about 230~330 s. The local characteristic function γ, eq. 68, was computed as a function of radius for the eigenperiod and angular order of each mode. $\gamma > 0$ is seen as a potential wall where modal energy evades and the eigenfunction becomes evanescent. $\gamma < 0$ is seen as a potential well where modal energy is trapped. The modal energy for each mode is normalized to the maximum value. γ is also normalized to its maximum. The scale for γ is at the top of each plot, but the unit is arbitrary.

volcano extending over a distance of about 400 km. If we assume that the waves in the satellite image have the period of about 300 s, the concentric pattern is identified to be the gravity waves excited by the volcanic eruption, because acoustic waves and Lamb waves should have much more shorter periods at the wavelength of several tens kilometers.

The choice of the top boundary type and its location are not important if a mode is naturally trapped, or ducted, below the top boundary by 'wall' layers which have positive γ. Our numerical computation confirms that the 270 s acoustic mode always exists for any type of top boundary if placed at higher than 100 km (Figure 5). The mode always hits a natural boundary near z=100 km and its modal energy is confined between z=0 and about 100 km.

The local atmospheric structure can deviate from the standard atmosphere model diurnally, seasonally, geographically and latitudinally. In the thermosphere the temperature is mainly controlled by the solar activity (CIRA 1972). These variations may result in the change of not only eigenperiod but also the energy density distribution of modes; as a result a trapped mode may become a propagating mode and vice versa. In table 2 we list the result of computation for an atmospheric structure close to the local model during the eruption of Mt. Pinatubo in 1991.

The local atmospheric model near Mt. Pinatubo in June has two distinct features. Low temperature, about 10^o K lower than the average at the bottom of the stratosphere, and high thermospheric temperature, about 500^o K higher. We choose the high thermospheric temperature because the solar activity was high in 1991. The trapped acoustic modes have little change in the eigenperiod. Two gravity modes with energy trapped in the stratosphere exist with distinct eigenfrequencies. The high temperature in the thermosphere results in the increase of γ, but still negative, and the modal energy density decreases more near z=200 km than those for

(a)

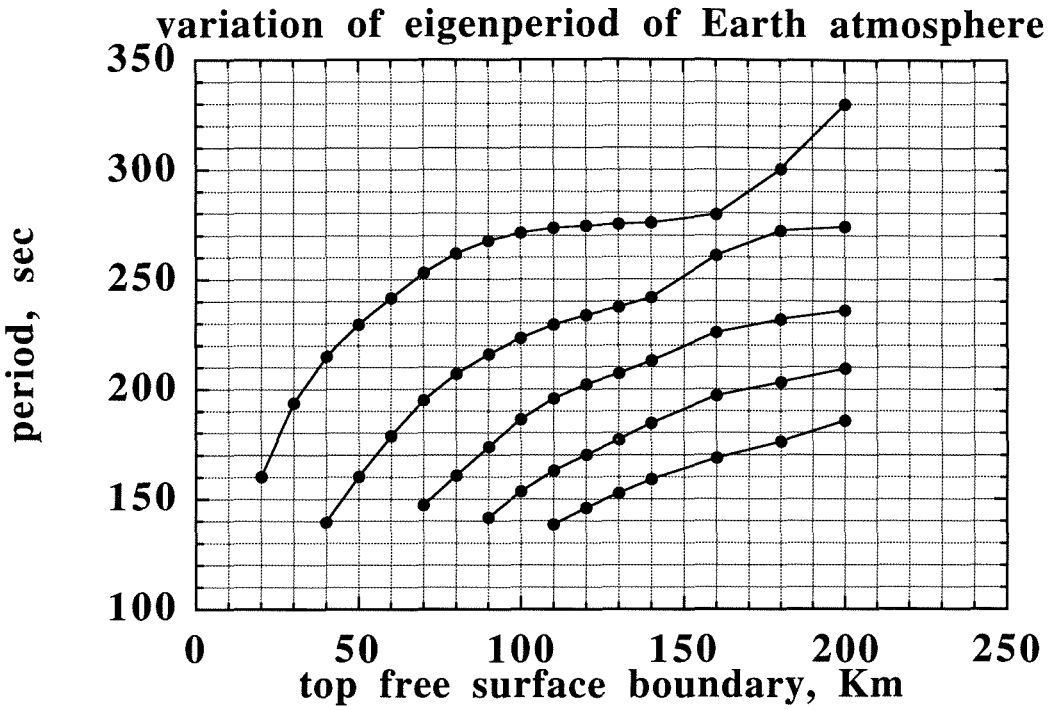

Figure 5. The variation of the eigenperiod of atmospheric acoustic modes (l=30) for the altitude change of the top boundary. (a) For free surface boundary. (b) For zero vertical displacement surface boundary.

(b)

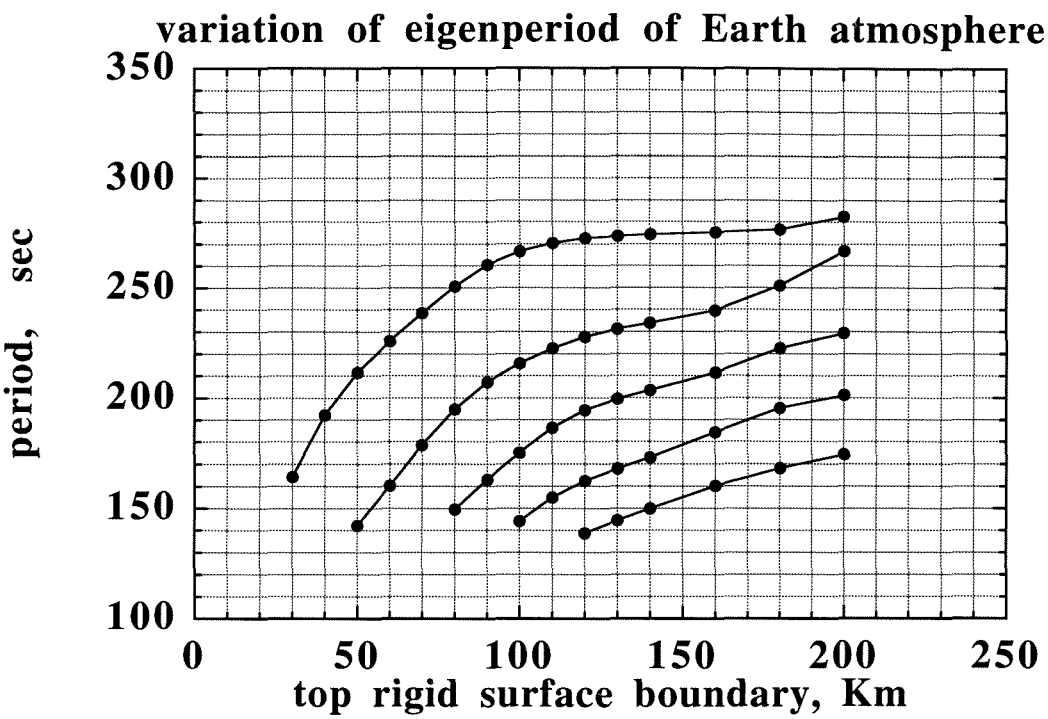
variation of eigenperiod of Earth atmosphere
period, sec
350
300
250
200
150
100
0
50
100
150
200
250
top rigid surface boundary, Km

Standard atmosphere		Local at Mt. Pinatubo	
mode type	period	mode type	period
acoustic	274 s	acoustic	272 s
acoustic	236 s	acoustic	235 s
acoustic	209 s	acoustic	207 s
acoustic	186 s	acoustic	182 s
gravity	299 s	gravity	320 s, 290 s

Table 2. Comparison of the eigenmodes of two atmospheric models. Local model near Mt. Pinatubo atmosphere is composed of: 0 km $<$ z $<$ 90 km reference atmosphere at 15^o N July, 90 km $<$ z $<$ 110 km reference atmosphere at 10^o N June and 110 km $<$ z $<$ 200 km exospheric temperature 1600 K. Tables are found in (Jursa ed., 1985). The same boundary conditions used in Figure 2 is applied. Acoustic modes with l=30 and gravity modes with l=2000 are computed.

the standard atmosphere. We speculate that the observed period 195 s during the 1982 El Chichón eruption may be a trapped acoustic mode when the solar activity was extremely high. In fact, in 1982 its cycle was near the peak (commun. National Geophysical Data Center). However, the reason why the amplitude spectrum peak near 230 s is missing in the seismographic observation during the 1982 El Chichón eruption is unknown.

4. Normal modes in the Earth

We use the preliminary reference Earth model (PREM) of Dziewonski and Anderson (1981) for the solid Earth. The normal modes of PREM are shown in Figure 6. A notable feature in Figure 6 is the tsunami branch with a nearly constant phase velocity of about 170 m/s. This mode is a surface gravity wave in the top ocean layer of the PREM Earth model with a thickness of $h = 3$ km. The tsunami branch and seismic branches are separated well in the $\omega - k$ domain. For the tsunami mode a simple long–wave approximation gives a non–dispersive phase velocity $\sqrt{g_o h}$ (Gill, 1982) which is close to the phase velocity of the tsunami modes computed for PREM. At very long wavelength, the phase velocity slightly decreases. For example, at l=10 the phase velocity decreases by about 3% from 170 m/s. At long period the Coriolis effect should be taken into account. At short wavelength, the dispersion relation of water waves deviates from the shallow water approximation and approaches the deep water approximation, and its phase velocity decreases according to $\sqrt{g_o/k_h}$. The reason why the two waves, Rayleigh waves and tsunamis with similar eigenfrequencies, do not couple is that the wavelength of the excess pressure field at the ocean bottom caused by tsunamis is very different from the wavelength of Rayleigh waves. Two waves having an interface between them are able to couple efficiently when both the period and the horizontal wavelength of the two waves are the same. This computation confirms the study by Comer (1984) who showed that for a flat Earth model,

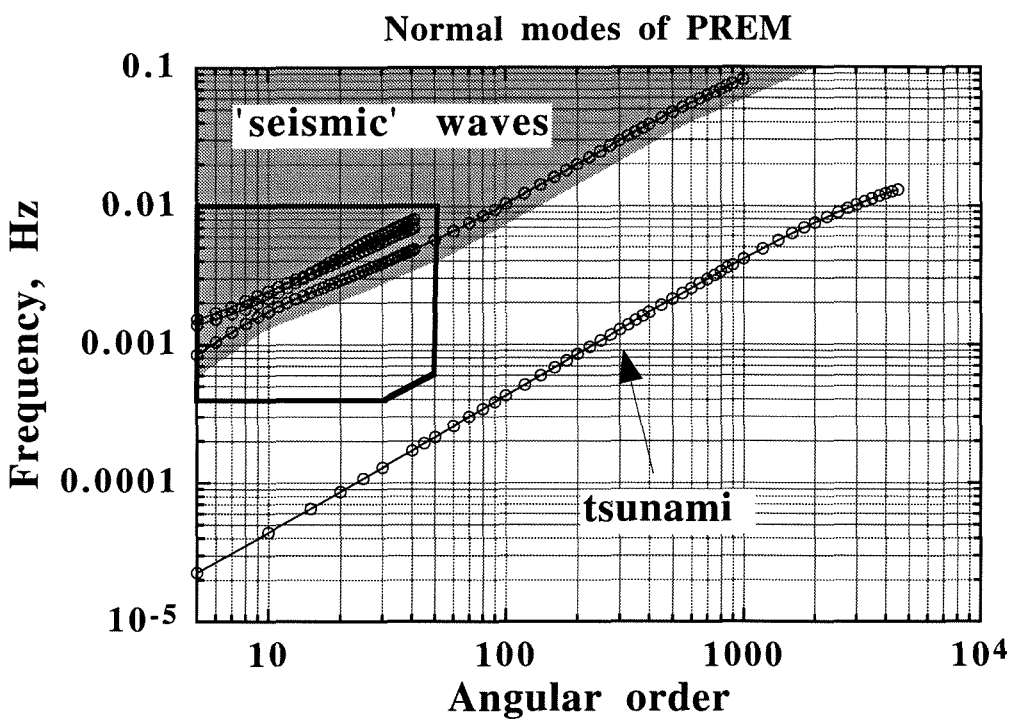

Figure 6. Spheroidal normal modes in the PREM (Dziewonski and Anderson 1981) Earth model which has a 3 km ocean layer at the top that allows water waves. Seismic waves and tsunami waves are almost decoupled. High angular normal modes l> 50 and tsunami modes are computed using the Cowling approximation. The boxed region is magnified in Figure 7.

Rayleigh waves and tsunamis are practically uncoupled over the entire periods of seismic waves, so in the propagation of tsunamis the elasticity of the Earth can be safely ignored. This weak coupling between seismic surface waves and tsunamis explains why the tsunamis in the ocean are never reported as an excitation source of surface waves of the solid Earth. However, it should be noted that tsunamis are indeed excited by the local deformation at the ocean bottom associated with earthquakes. In this case the initial disturbance of tsunami is caused by a sudden uplift or subsidence of the ocean surface and not related to the wave coupling.

The adoption of the Cowling approximation changes the eigenperiod of the non–radial spheroidal normal modes. The eigenperiods of the fundamental spheroidal modes with and without the Cowling approximation for a solid Earth model are shown in Table 3. The frequency of fundamental spheroidal modes which we are interested in, 3–5 mHz, changes by less than 0.3%. The merit of the use of the Cowling approximation is that we can reduce the computational time by a factor of a few and improve the computational accuracy because we have fewer dependent variables.

5. Coupling between the atmosphere and the solid Earth

The acoustic coupling between the atmosphere and the solid Earth has been considered to be very small. The atmosphere is treated as a vacuum by seismologists and the surface of the Earth is a rigid boundary for atmospheric scientists because of the large acoustic impedance contrast; $(\rho c)_{atmosphere}/(\rho c)_{crust}$ is about the order of 10^{-4}. The phase velocity of acoustic waves in the atmosphere differs from that of seismic waves by one order of magnitude. However, in a few cases ground motions induced by the atmospheric acoustic coupling have been observed on seismograms. Seismic waves with a period of about 240 s excited by the pressure pulse near a nuclear explosion in the air were observed by a ground tiltmeter (Ben–Menahem and

angular order	Cowling approx.	without approx.
2	4127.43	3233.51
3	2505.96	2134.26
4	1693.90	1545.43
5	1258.02	1189.87
6	999.04	963.18
7	832.87	811.81
8	720.92	707.45
9	642.86	633.59
10	586.01	579.21
11	542.21	536.93
12	506.63	502.41
13	476.76	473.27
14	451.05	448.14
15	428.65	426.18
16	408.93	406.79
17	391.38	389.54
18	375.68	374.06
19	361.52	360.10
20	348.68	347.41
21	336.95	335.82
22	326.20	325.17
23	316.25	315.33
24	307.04	306.19
25	298.43	297.67
26	290.39	289.69
27	282.84	282.19
28	275.71	275.12
29	268.98	268.43
30	262.60	262.08
31	256.53	256.05
32	250.76	250.31
33	245.24	244.82
34	239.97	239.58
35	234.93	234.56
36	230.09	229.75
37	225.45	225.13
38	220.99	220.69
39	216.71	216.42
40	212.58	212.31
41	208.60	208.34
42	204.76	204.52
43	201.06	200.84
44	197.49	197.27
45	194.04	193.83
46	190.70	190.51
47	187.47	187.29
48	184.34	184.17
49	181.32	181.15
50	178.39	178.23

Table 3. Eigenperiod of fundamental spheroidal modes for the PREM Earth model (Dziewonski and Anderson 1981) in second. The left column numbers are the eigenperiods including the effect of self–gravity. The right column is obtained using the Cowling approximation (Cowling 1941) which ignores the gravity potential perturbation but includes the reference gravity. The physical dispersion is included in both cases.

Singh, 1980) at a teleseismic distance. Harkrider *et al.* (1974) computed theoretical seismograms from atmospheric point sources for the fundamental Rayleigh waves with a period of less than 60 s at teleseismic distances. Long–period harmonic Rayleigh wave motion associated with the 1991 eruption of Mt. Pinatubo (15.14^o N 120.35^{o}E) in the Philippines, were reported by Kanamori and Mori (1992) and Widmer and Zürn (1992), and with the 1982 El Chichón eruption by Widmer and Zürn (1992) (Table 1).

5.1 Coupling mechanism

We can expect efficient coupling between the solid Earth and the atmosphere if seismic modes and the atmospheric modes fall into the same region of the frequency wavenumber ($\omega - k$) domain. In fact, a common region of atmospheric modes and seismic modes exists near the period of about 200$\sim$300 s (Figure 7), the period of the observed Rayleigh wave. As discussed earlier, an atmospheric acoustic mode near the period 200$\sim$300 s with a small angular order has a small group velocity and the modal energy density is trapped in the atmosphere below the thermosphere. Once a long–wavelength atmospheric acoustic mode is excited by a point source in the air, the modal energy is confined in the atmosphere horizontally and vertically. The trapped acoustic mode can efficiently excite a Rayleigh wave that has the same eigenfrequency and horizontal wavelength to those of the acoustic mode.

5.2 Comparison of synthetic ground motion with observations

Since the observed surface waves are fundamental mode Rayleigh waves (Kanamori and Mori, 1992; Widmer and Zürn, 1992), we compute the normal modes near the fundamental spheroidal mode branch (Figure 8) for a spherically symmetric Earth model including the ocean and atmosphere. These waves represent seismic Rayleigh waves and acoustic waves in the atmosphere. The normal modes of a coupled system using a combined Earth model automatically takes into account the mechan-

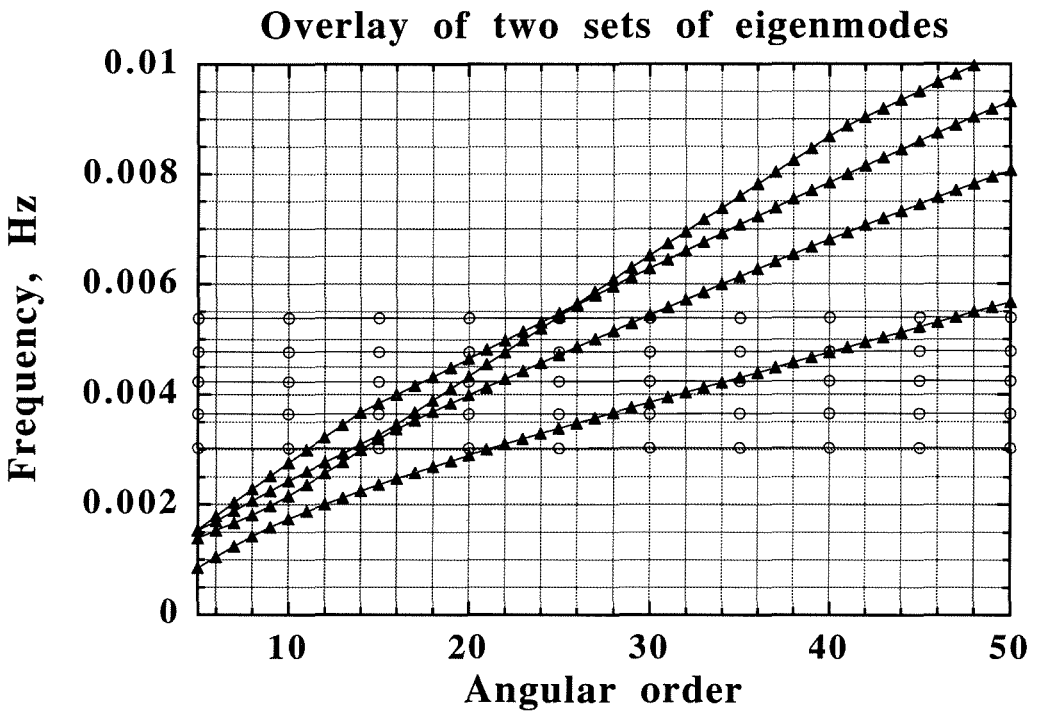

Figure 7. Overlay of atmospheric modes (box in Figure 2) and seismic modes (box in Figure 6). Solid triangles and open circles are fundamental and higher spheroidal modes and atmospheric acoustic modes, respectively. Strong coupling between the Rayleigh waves and the atmospheric acoustic waves is expected because of the proximity of the horizontal phase velocities.

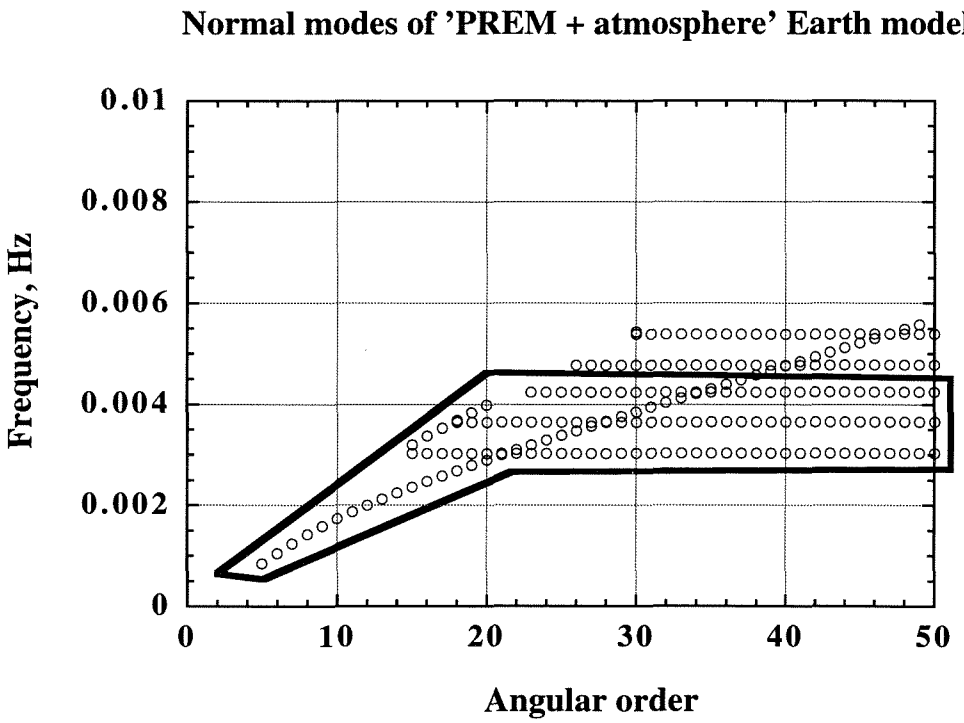

Figure 8. Normal modes of the combined PREM Earth model and U.S. Standard Atmosphere 1976. Only modes inside the polygon are used in the computation of synthetic spectrum in Figure 11.

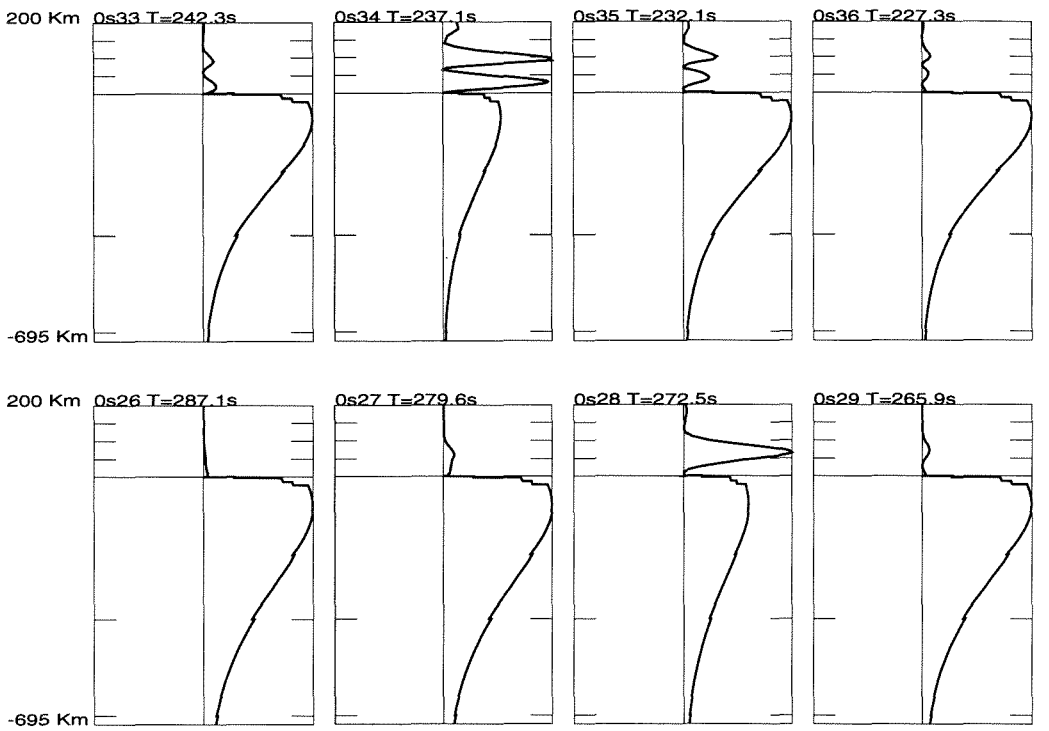

Figure 9. Modal energy density distribution of the fundamental spheroidal modes near the trapped atmospheric acoustic mode branch for the combined Earth model. Energy density in the atmosphere is magnified by 100. Amplitude of energy density of each mode is normalized by its maximum value and scale is linear.

ical coupling between atmosphere, ocean and solid Earth. The computed eigenfrequencies for the combined model deviates little from the uncoupled eigenfrequencies except when two modes with the same angular order have very close eigenfrequencies.

The modal energy density of the fundamental spheroidal modes for the combined Earth model is shown in Figure 9. Note that the plotted energy density in the atmosphere is magnified by 100. The atmospheric part of the energy density of Rayleigh waves is generally very small, far less than 1% of the maximum energy density in the solid Earth. Conversely the acoustic modes also have little energy penetration in the solid Earth. For a few exceptional seismic spheroidal modes with a period close to the trapped atmospheric acoustic modes, the peak amplitude of the energy density in the atmosphere is as large as 1% of the peak density amplitude in the solid Earth. The small but substantial modal energy distribution of 272 s and 237 s spheroidal modes in the atmosphere suggests that the 272 s and 237 s modes are preferentially excited by a source in the lower atmosphere compared to other spheroidal modes because the excitation amplitude of an eigenmode by a point source is roughly proportional to the energy density amplitude at the location of the source.

The amplitude in the air of a seismic spheroidal mode can be large because of very small density in the upper atmosphere. From the ratio of the amplitude peaks of the energy density in the air and the solid Earth, $\sim 1\%$, and the ratio of material density at the peaks, $\sim 10^{-10}$, we get $u_{\text{at z=100km}}/u_{\text{at z=-50km}} \sim 10^4$. When the mode has amplitude 1 μm at the ground, the amplitude of this mode at z=100 km is about 1 cm and much smaller than the wavelength of this mode. The linear amplitude theory of small oscillations is still valid.

We compute the synthetic seismograms using the eigenfunctions for the combined Earth model for the subset of modes shown in Figure 8. The excitation source

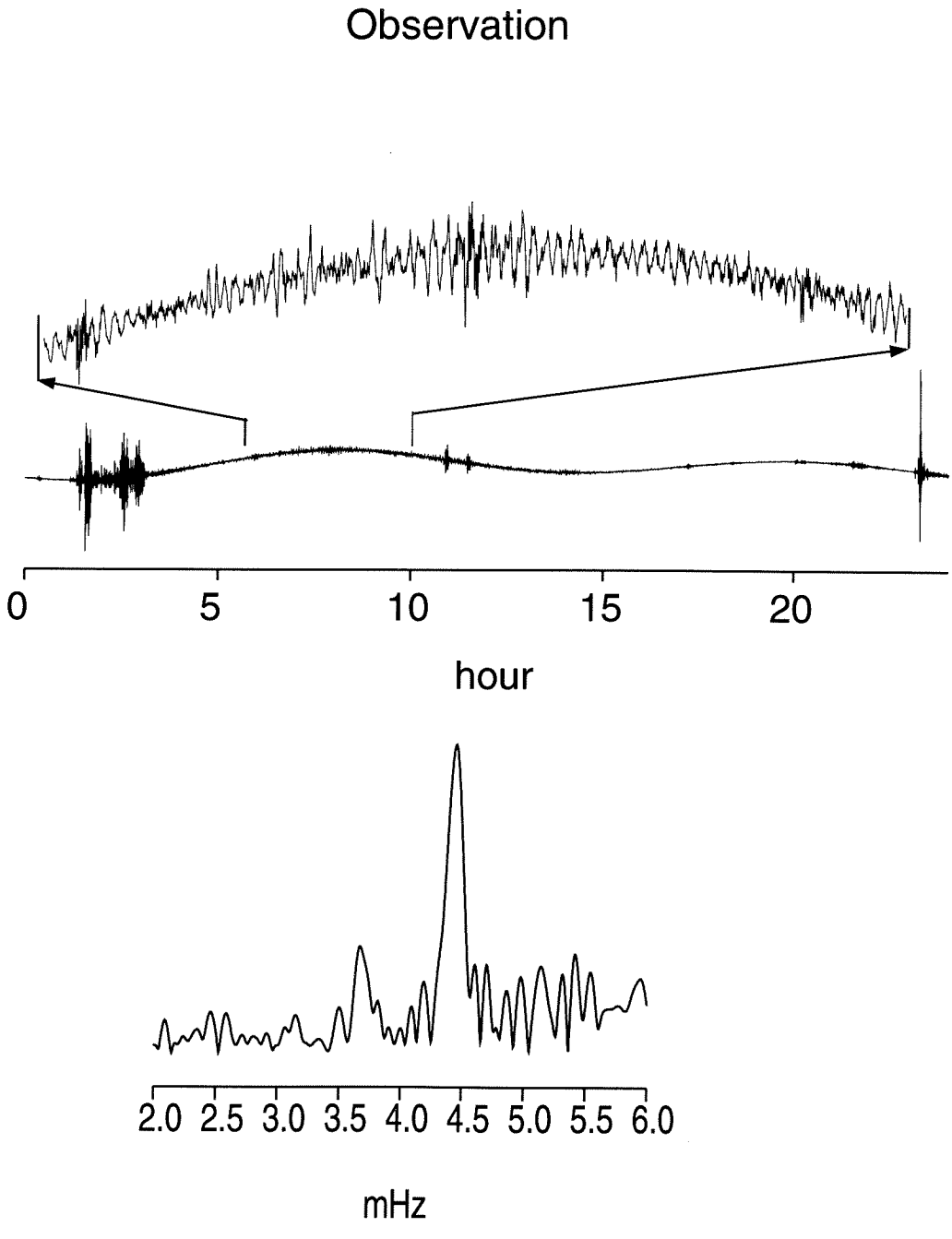
Observation
0
5
10
15
20
hour
2.0 2.5 3.0 3.5 4.0 4.5 5.0 5.5 6.0
mHz

Figure 10. Top) Observed harmonic signals in vertical VLP channel data at MAJO (Δ=26^o) Matsushiro, Japan. The record starts at 1991/06/15 00:00 GMT. The large signals in the first five hours are from teleseismic events, a Ms 6.5 in the Caucasus and a Ms 6.5 in the South Sandwich Is. The peak to peak amplitude is about 6 micron–meters after removing the very long–period tidal signals. Bottom) Amplitude spectra of the magnified part of the seismogram. The peaks at 4.4 mHz (230 s) and 3.7 mHz (270 s) are observed at many seismographic stations. The vertical scale is linear.

is modeled by an isotropic point source with a moment M_o, three mutually perpendicular "dipoles without moment," which is located at $(r_s, 0, 0)$ and varies as a step function in time.

The displacement at (r, θ, φ) is given by (Woodhouse and Girnius 1982)

$$\begin{aligned} u_r(r,\theta,\varphi,t) &= \sum_k c_0 U_k(r) Y_l^{0\,0}(\theta,\varphi) S_k e^{i\omega_k t}, \\ u_\theta(r,\theta,\varphi,t) &= \sum_k c_1 V_k(r)(-Y_l^{1\,0}(\theta,\varphi) + Y_l^{-1\,0}(\theta,\varphi)) S_k e^{i\omega_k t}, \\ u_\varphi(r,\theta,\varphi,t) &= 0, \end{aligned} \tag{87}$$

where

$$S_k = -c_0 M_o \left(\frac{\partial U_k(r_s)}{\partial r_s} + \frac{2U_k(r_s)}{r_s} - \frac{l(l+1)V_k(r_s)}{r_s} \right), \tag{88}$$

$$c_0 = \sqrt{\frac{2l+1}{4\pi}}, \tag{89}$$

$$c_1 = \frac{1}{2}\sqrt{\frac{(2l+1)(l+1)l}{4\pi}} \tag{90}$$

and $Y_l^{N\,m}(\theta, \varphi)$ is the generalized spherical harmonics defined in Phinney and Burridge (1973) and k denotes a multiplet mode. The eigenfunctions used here are computed with the free or zero radial displacement surface boundary condition and normalized by

$$\int_0^R \omega^2 \rho_o ({U_k}^2 + l(l+1){V_k}^2) r^2 = 1. \tag{91}$$

The original broadband seismogram recorded in the day of the Pinatubo eruption is shown in Figure 10. The amplitude spectrum of the synthetic ground motion is plotted in Figure 11. As we expected, the spheroidal modes near 270 s and 230 s are preferentially excited and the observed amplitude ratio of the two peaks near 230 s and 270 s is reproduced in the synthetic. We did not include the modes with periods shorter than 200 s because in the real Earth, the atmospheric eigenfunction becomes a propagating acoustic wave (section 3) and the excitation of the mode by a source

in the propagating region will be small compared to the excitation by a source in the standing wave region.

A higher altitude source yields larger ground motion because the energy density of the strongly coupled modes increases with altitude in the troposphere and the stratosphere and these modes are excited more efficiently by a source at higher altitude. The amplitude of the ground motion by a source located at 1, 2, 4 and 8 km in the air relative to the amplitude by a source at 0.5 km are 1.1, 1.2, 1.5 and 2.2, respectively. The waveforms of harmonic oscillations have little dependence on the source altitude.

Seismic moment has been used to express the magnitude of earthquakes in seismology; however, the source description in terms of energy is more appropriate for volcanic eruptions. We follow Ingersoll and Kanamori (written communication, 1995) to relate the dipole moment source to an energy source. For an elastic medium the permanent displacement u_r at distance r from an isotropic dipole moment M_o is $M_o/(4\pi r^2(\kappa + 4\mu/3))$, where μ is the rigidity. For a fluid we simply take μ=0. Static increase of the radius of a small cavity in a fluid from ϵ to $\epsilon + \delta\epsilon$ displaces the material at r by $(\epsilon/r)^2\,\delta\epsilon$. The energy E_o worked against the ambient pressure P_o by the increase of the volume of the cavity is $P_o 4\pi\epsilon^2\,\delta\epsilon$. Using $\kappa = \Gamma P_o$ and requiring E_o and M_o produce the same static displacement, we obtain $E_o = M_o/\Gamma$. Kanamori and Mori (1992) observed that the source duration is at least two hours. If we take the two hours as the source duration, the dipole moment 10^{19} Nm is required to explain the Rayleigh wave amplitude. Based on the conversion from isotropic moment to energy, we can roughly estimate the energy release from Mt. Pinatubo during the major eruption in 1991/06/15, about 10^{19} J. Using the relationship between the size of a nuclear explosion and its energy release, 1 ton nuclear explosion = 10^9 calories = 4.189e109 joules (personal comm. Harkrider, 1995), the energy release during the

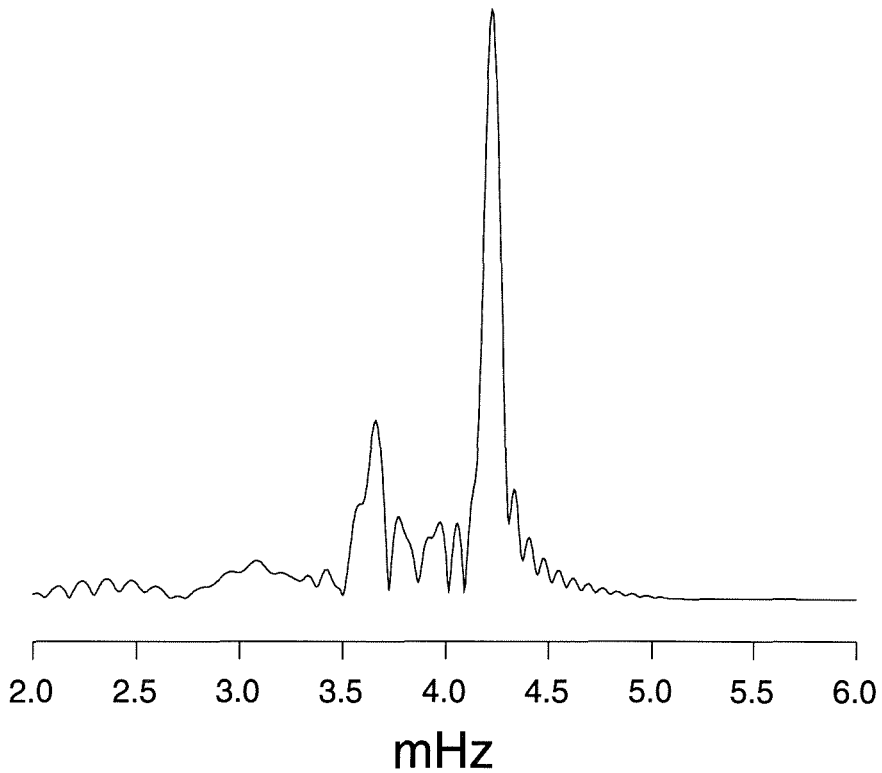

Figure 11. Fourier spectrum of the synthetic ground motion at MAJO for a point source located 1 km high in the atmosphere. The ground motion is computed using the normal mode method by summing up the modes in Figure 7. A seismic moment of 10^{19} Nm is required to explain the observed ground motion for a 2–hour–long source duration. The amplitude spectra is computed for a 4.4–hour–long synthetic seismogram starting at 45 minutes after the origin time. The vertical scale is linear.

1991 Mt. Pinatubo eruption corresponds to a 2000 Mton size nuclear explosion For more precise estimate we need to model the physical mechanism of volcanic eruptions, and its excess thermal and mass input should appear in the equation of motion as excitation terms (Pierce, 1968).

6. Discussion

The air–sea coupling, instead of the air–ground coupling of our study, was studied by Press and Harkrider (1966) and Harkrider Press (1967). They discussed the coupling between the ocean waves and the atmospheric internal gravity waves excited by the 1883 Krakatoa eruption. They showed that in the synthetic marigram computed for a source in the air, three distinct signals corresponding to the Lamb wave branch, an internal gravity branch and the tsunami branch exist; however, in the synthetic barograph only two signals corresponding to the first two air waves appear and no substantial signal exists at the arrival time of the tsunami wave. If we consider only the static pressure response of the ocean surface for the surface atmospheric pressure loading and unloading originating from a source in the air, the missing atmospheric pressure disturbance corresponding to the tsunami is not explained. In Figure 2b, we can draw a dispersion line of long–waves in the ocean, tsunami, with a constant phase velocity of about 170 m/s. The tsunami branch crosses the internal gravity mode branches of the atmosphere. The ocean dynamic response for an atmospheric pressure disturbance is frequency dependent and becomes very sensitive to a wave in the atmosphere which has the same wavelength and period as that of tsunami. Those atmospheric waves can couple to the ocean and produce tsunami, in spite of the very small atmospheric pressure variation.

The mechanism of the coupling of the atmospheric acoustic modes to the solid Earth we discussed is similar to this case. In both cases, two media, one overlaying the other, can sustain waves with the same wavelength and frequency along the boundary.

The coupling can sometimes become so strong that we only come to observe the waves in the layer which does not contain the source but excited through coupling to the waves in the other layer. For the 1883 Krakatoa eruptions, the source is in the air and atmospheric waves were excited. The waves in the ocean layer, tsunami, were excited through the air–sea coupling. For the 1991 Pinatubo eruption the source is also in the air and atmospheric waves are excited. The waves in the solid Earth, Rayleigh waves, were excited through the air–ground coupling.

Below z=100 km the kinetic eddy viscosity has about constant value $\sim$ 100 m^2/s and the molecular viscosity is several orders of magnitude smaller. At z=200 km the atmospheric density decreases further to about 10^{-10} of the surface air density, or 10^{-3} of the air density at z=100 km. Above z=100 km the molecular diffusion is the dominant factor in the dissipation of atmospheric waves, and its value increases with altitude (U.S. standard atmosphere). The distinction of eigenfunctions below the highly viscous region for different types of the upper boundary condition will be small and the boundary condition becomes less important (Francis 1973). The dissipation of a seismic spheroidal mode resulting from the wave disspation in the atmosphere is negligible compared to the intrinsic Q in the solid Earth because the total energy in the atmosphere is only a very small fraction of the total modal energy of the spheroidal mode.

7. Conclusion

The two peaks at about 230 and 270 s of the amplitude spectra of the ground motion observed for the 1991 Mt. Pinatubo eruption correspond to the resonant period of very long wavelength standing acoustic modes in the atmosphere. For a standard atmosphere and solid Earth model, a few atmospheric acoustic modes at low angular order numbers become a standing wave in the atmosphere and have the same eigenperiod as some spheroidal modes of the solid Earth with the same

horizontal wavelength. These acoustic modes in the air set off by the volcanic eruption can couple to Rayleigh waves efficiently. The oscillation of standing wave results in periodic loading and unloading on the ground and can be detected with seismographs at teleseismic distances. On the other hand, the gravity mode with a period of 300 s was recorded as a barographic pressure change near a volcanic source such as the 1980 Mt. St. Helens eruption, but was not detected by seismographs. Because of its slow phase velocity of about 100 m/s, the gravity wave does not couple to Rayleigh waves efficiently.

From the energy density distribution and the local behavior analysis of the normal modes of the atmosphere, we found that the atmospheric structure near the mesopause and the thermosphere results in a standing acoustic wave with long wavelength confined between the ground and the thermosphere. The mode with a period of 270 s is the gravest mode for this structure and the mode with a period of 230 s is the first overtone. Higher overtones become vertically propagating waves and will not be a source of harmonic loading on the surface. The gravity mode with a period of 300 s is a trapped mode in the stratosphere. A regional or temporal variation of the atmospheric structure, such as lower temperature in the stratosphere in tropics and higher thermospheric temperature caused by the high solar activity, may result in variations of the period of the barographic oscillations because of the change of the eigenperiod of the gravity mode trapped in the stratosphere, and the addition of one more frequency in the harmonic ground motion because of the appearance of the second standing overtone.

To simulate the coupling effect between the atmosphere and the solid Earth during the volcanic eruption of Mt. Pinatubo, synthetic ground motion is computed with the normal mode method. The observed amplitude spectral peaks of long–period Rayleigh waves at 230 s and 270 s are seen in the synthetic amplitude spectrum and

the amplitude ratio of the two peaks is reproduced in the simulation.

The observed absolute amplitude is explained by an isotropic point source with a moment 10^{19} Nm for a two–hour–long source duration. Using the conversion from a moment source to a energy source, the amount of energy, which contributed to the excitation of atmospheric waves, released from the 1991/06/15 Mt. Pinatubo eruption is estimated about 10^{19} J.

8. Acknowledgements

The author would like to thank many people who joined the discussion on the normal mode formulations from the basic physical first principles. F. Gilbert, R. Hide, A. Ingersoll, G. Masters, J. Woodhouse, and all the participants of the seismo lab coffee breaks convinced me that all the normal mode formulism for the Earth, the Sun, stars, tsunami and the atmosphere can be derived indeed from a common set of first principles and are consistent with each other.

References

Alterman, Z., H. Jarosch and C. L. Pekeris, 1956, Oscillations of the earth, *Proc. Roy. Soc. London, A*, **252**, 80–95.

Arfken, G., 1985, *Mathematical Methods for Physicists, 3rd ed.*, San Diego, Academic Press.

Beer, T., 1974, *Atmospheric Waves*, John Wiley & Sons, Inc., New York.

Benioff, H., M. Ewing and F. Press, 1951, Sound waves in the atmosphere generated by a small earthquake, *Proc. Ntl. Acd. Sci.*, **37**, 600–603.

Ben–Menahem, A. and S. J. Singh, 1981, *Seismic Waves and Sources*, Springer–Verlag, New York.

CIRA 1972: COSPAR international reference atmosphere, 1972, COSPAR working group IV. Akademie–Verlag, Berlin.

Comer, P. R., 1984, Tsunami generation: a comparison of traditional and normal mode approaches. *Geophys. J. Astron. Soc.*, **77**, 29–41.

Cowling, T. G., 1941, The non–radial oscillations of polytropic stars, *Mon. Not. Roy. Astron. Soc.*, **101**, 367–375.

Cox, J. P., 1980. *Theory of Stellar Pulsation*, Princeton University Press, Princeton N. J.

Dziewonski, A. M. and D. L. Anderson, 1981, Preliminary reference Earth model, *Phys. Earth Planet. Inter.*, **25**, 297–356.

Francis, S. H., 1973, Acoustic–gravity modes and large–scale traveling ionospheric disturbances of realistic, dissipative atmosphere, *J. Geophys. Res.*, **78**, 2278–2301.

Friedman, J. P., 1966, Propagation of internal gravity waves in a thermally stratified atmosphere, *J. Geophys. Res.*, **71**, 1033–1054.

Georges, T. M. ed., 1968, Acoustic–gravity waves in the atmosphere, ESSA/ARPA symposium proceedings, at Boulder Colo., U.S. Government Printing Office, Washington D.C.

Harkrider, G. D., 1964, Theoretical and observed acoustic–gravity waves from explosive sources in the atmosphere, *J. Geophys. Res.*, **69**, 5295–5321.

Harkrider, G. D., and F. Press, 1967, The Krakatoa air–sea waves: an example of pulse propagation in coupled systems, *Geophys. J. Astron. Soc.*, **13**, 149–159.

Harkrider, G. D., C. A. Newton and E. A. Flinn, 1974, Theoretical effect of yield and burst height of atmospheric explosions on Rayleigh wave amplitudes, *Geophys. J. Astron. Soc.*, **36**, 191–225

Gilbert, F., 1980, An introduction to low–frequency seismology, *Proc. Int. Scho. Phy.*, LXXVIII, Dziewonski and Bosch ed., 41–81, North–Holland, Amsterdam.

Gill, E. A., 1982, *Atmospheric–Ocean Dynamics*, Academic Press, San Diego.

Ledoux, P. and T. Walraven, 1958, *Handbuch der physik*, **51**, 353–604.

Love, A. E. H., 1911, *Some Problems of Geodynamics*, University Press, Cambridge.

Jensen, F. B., W. A. Kupperman, M. B. Porter and H. Scmidt, 1994, Computational ocean acoustics, AIP Press, New York.

Jursa, A. S. ed., 1985, *Handbook of Geophysics and Space Environment*, U.S. Air Force Geophysics Laboratory, Air Force Systems Command National Technical Information Service.

Kanamori, H. and J. Mori, 1992, Harmonic excitation of mantle Rayleigh waves by the 1992 eruption of mount Pinatubo, Philippines, *Geophys. Res. Lett.*, **19**, 721–724.

Kanamori, H., J. Mori and D. G. Harkrider, 1994, Excitation of atmospheric oscillations by volcanic eruptions. *JGR*, **99**, 21947–21961.

Mikumo, T., 1968, Atmospheric pressure waves and tectonic deformation associated with the Alaskan earthquake of March 28, 1964, *J. Geophys. Res.*, **73**, 2009–2025.

Mikumo, T. and B. A. Bolt, 1985, Excitation mechanism of atmospheric pressure waves from the 1980 Mount St. Helens eruption, *Geophys. J. Astron. Soc.*, **81**, 445–461.

Pekeris, C. L., 1939, The propagation of a pulse in the atmosphere, *Proc. Roy. Soc. London, A*, **171**, 434–449.

Pekeris, C. L., 1948, The propagation of a pulse in the atmosphere. Part II, *Phys. Rev.*, **73**, 145–154.

Pekeris, C. L. and H. Jarosch, 1958, The free oscillations of the Earth, *Contribution in Geophysics in Honor of Beno Gutenberg*, **1**, 171–192, Pergamon, New York.

Phinney, R. A. and R. Burridge, 1973, Representation of the elastic–gravitational excitation of a spherical Earth model by generalized spherical harmonics, *Geophys. J. Astron. Soc.*, **34**, 451–487.

Pierce, D. A., 1966, Justification of the use of multiple isothermal layers as an approximation of the real atmosphere for acoustic–gravity wave propagation, *Radio Science*, **1**, 265–267.

Pierce, D. A., 1968, Theoretical source models for the generation of acoustic–gravity waves by nuclear explosions, in *Acoustic–Gravity Waves in the Atmosphere*, ed. T. M. Georges, U.S. Government Printing Office, Washington, D.C.

Pierce, D. A. and J. W. Posey, 1970, Theoretical prediction of acoustic–gravity pressure waveforms generated by large explosions in the atmosphere, Air Force Cambridge Research Laboratories, Bedford, MA.

Press, F. and D. G. Harkrider, 1966, Air–Sea waves from the explosion of Krakatoa, *Science*, **154**,1325–1327.

Press, W. H., S. T. Teukolsky, W. T. Vettering and B. P. Flannery, 1992, *Numerical Recipes, 2nd ed.*, Cambridge University Press.

Saito, M., 1988, DISPER80: A subroutine package for the calculation of seismic normal–mode solutions, in *Seismic Algorithms*, 293–391, Academic Press, New York.

Takeuchi, H. and M. Saito, 1972, Seismic surface waves, in *Methods in Computational Physics*, Vol. 11, ed. B. A. Bolt, 217–295, Academic Press, New York.

Unno, W., Y. Osaki, H. Ando, H. Saio, H. Shibahashi, 1989, *Nonradial Oscillations of Stars, 2nd ed.*, Tokyo University Press, Tokyo.

U.S. standard atmosphere, 1976, Committee on the Extension to the Standard Atmosphere, U.S. Government Printing Office, Washington.

Widmer, R. and W. Zürn, 1992, Bichromatic excitation of long–period Rayleigh and air waves by the Mount Pinatubo and El Chichón volcanic eruptions, *Geophys. Res. Lett.*, **19**, 765–768.

Woodhouse, J. H., 1988, The calculation of eigenfrequencies and eigenfunctions of

the free oscillations of the Earth and the Sun, in *Seismic Algorithms*, 321–370, Academic Press, New York.

Woodhouse, J. H. and T. P. Girnius, 1982, Surface waves and free oscillations in a regionalized earth model, *Geophys. J. Astron. Soc.*, **68**, 653–673.

PART II-A

An analysis of nearfield normal mode amplitude anomalies of the Landers earthquake

Abstract

The 1992 Landers earthquake (M_w=7.3) occurred in the middle of the TERRAscope network. Long-period Rayleigh waves recorded at TERRAscope stations ($\Delta \leq 3°$) after travelling around the Earth show large amplitude anomalies, one order of magnitude larger than spherical Earth predictions up to a period of about 600 s. The ground motions over the epicentral region at and after the arrival of R4-5 are in phase at all stations. These observations are inconsistent with the nearly vertical strike slip mechanism of the Landers earthquake. Synthetic seismograms for a rotating, elliptic and laterally heterogeneous Earth model calculated by the variational method agree well with the observed waveforms. Calculations for various 3D Earth models demonstrate that the amplitudes are very sensitive to the large scale aspherical structure in the crust and the mantle. The anomalies for modes shorter than 300 s period can be explained by lateral heterogeneity shallower than the upper mantle. Rotation of the Earth and lower mantle heterogeneity are required to explain mode amplitudes at longer periods. Current whole mantle seismic tomographic models can fully explain the observed amplitudes longer than 300 s. To assess the effect of the high order lateral heterogeneity in the mantle, more precise estimate of the crustal correction is required.

1. Introduction

The 1992 Landers Earthquake (6/28/1992 M_w=7.3) occurred in the middle of the Caltech/USGS TERRAscope network. Figure 1 shows the epicenter, the source mechanism determined from teleseismic surface waves (Kanamori *et al.*, 1992) and nearby broadband stations in California. Since the mechanism is a nearly vertical strike slip, we expect long–period Rayleigh waves, or spheroidal modes, to be nodal near the epicenter and antipode for a spherical non–rotating laterally homogeneous Earth model. However, the amplitudes of the Rayleigh waves observed at the TERRAscope stations are much larger than expected for a spherical Earth model. Figure 2 compares the observed long–period vertical component seismograms at one teleseismic station and four nearby stations with synthetic seismograms computed for a spherically symmetric non–rotating Earth model. Surface waves with frequency between 3 and 4 mHz dominate in these records. A spherical Earth model explains Rayleigh wave amplitudes at MAJO (distance $\Delta = 81°$) and BKS ($\Delta = 6°$) but not at TERRAscope stations ($\Delta \leq 3°$) where observed amplitudes are an order of magnitude larger than the spherical Earth predictions.

2. Observations

We take the Fourier spectra of the observed and synthetic seismograms for a spherical non–rotating Earth model at MAJO, BKS and PAS (Figure 3). At PAS the discrepancy of the amplitudes of the fundamental spheroidal modes is very large up to a period of about 600 s, or mode ${}_0S_{10}$. At BKS anomalous amplitudes are found around ${}_0S_{11}$ and ${}_0S_{19}$. At large epicentral distances (e.g., MAJO) no amplitude anomalies are observed. All TERRAscope stations are located within 300 km of the epicenter and show similar large amplitude spectra. We also observed that the ground motion at long periods, several hours after the origin time, becomes in phase over the entire epicentral region (Figure 4 top). This is not expected from the surface wave

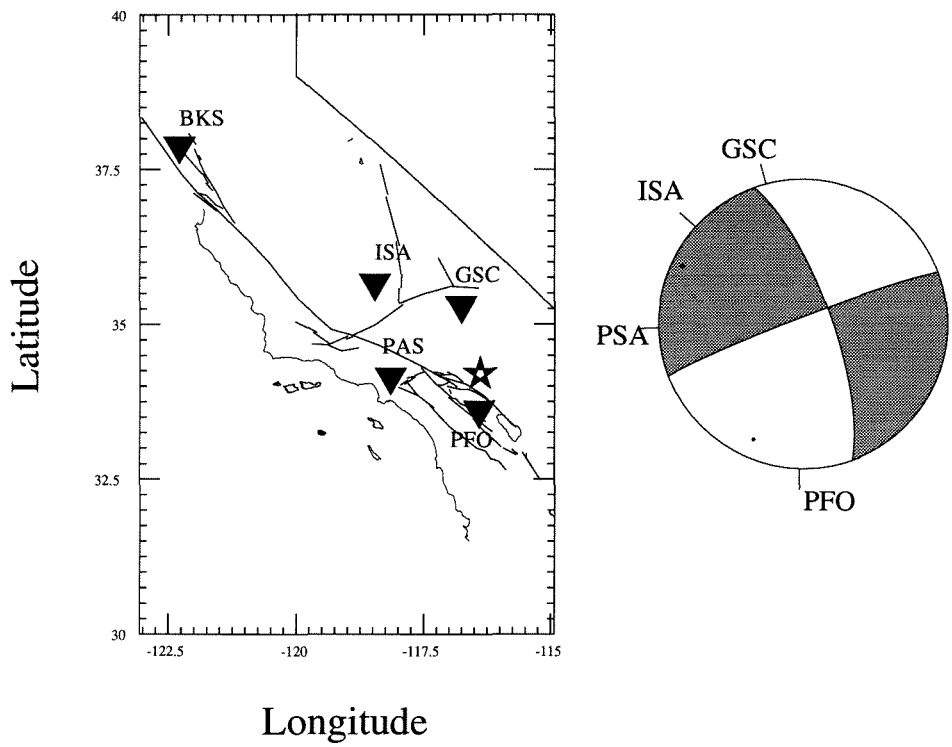

Figure 1. The location of the Landers earthquake (M_w=7.3, June 28, 1992, 11h57m34s GMT, 34.20°N, 116.44°W) and the five broadband stations in California used in this study. The source mechanism (dip=74°, rake=-176°, strike=340°) is nearly vertical strike slip.

Figure 2.

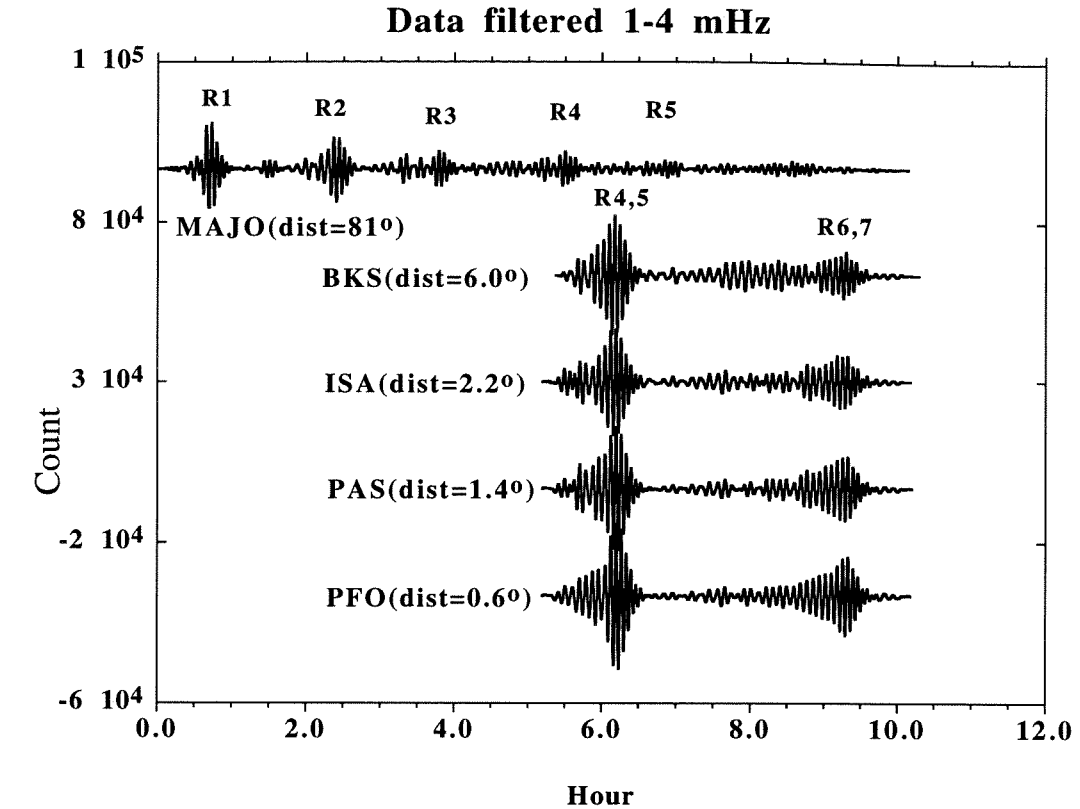
Data filtered 1-4 mHz
1 10^5
8 10^4
3 10^4
-2 10^4
-6 10^4
Count
R1
R2
R3
R4
R5
R4,5
R6,7
MAJO(dist=81°)
BKS(dist=6.0°)
ISA(dist=2.2°)
PAS(dist=1.4°)
PFO(dist=0.6°)
0.0
2.0
4.0
6.0
8.0
10.0
12.0
Hour

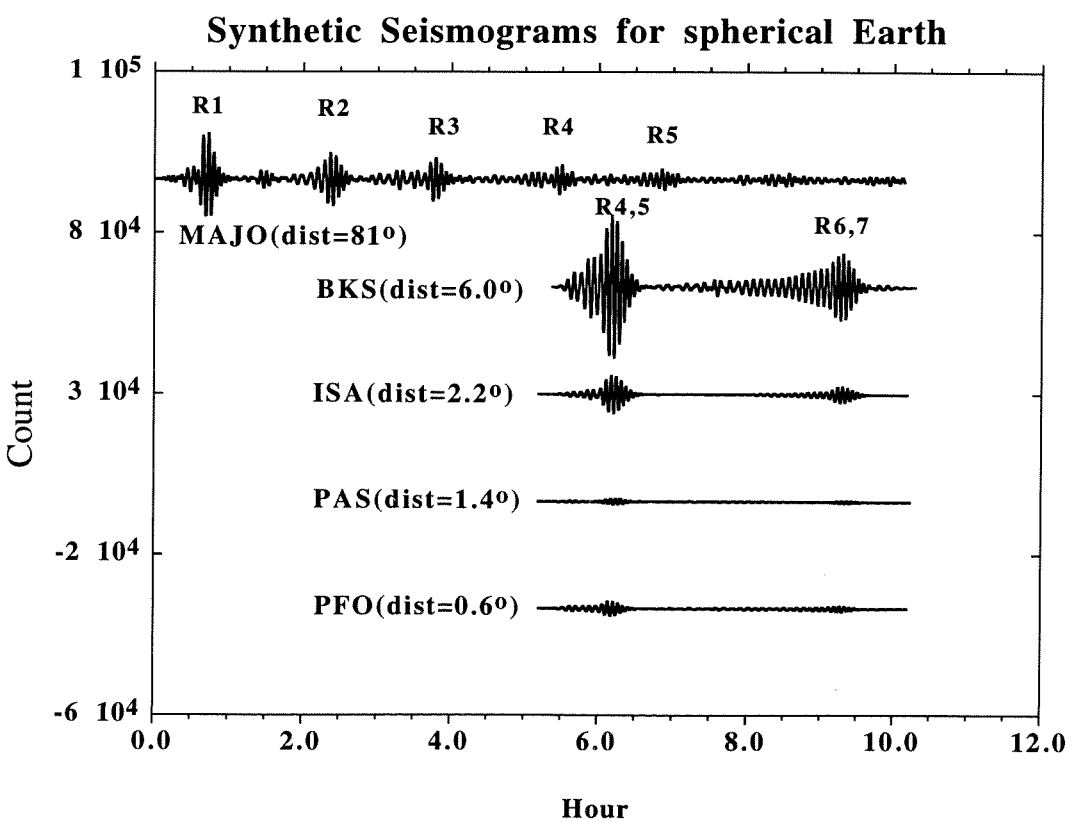
Synthetic Seismograms for spherical Earth
1 10^5
8 10^4
3 10^4
-2 10^4
-6 10^4
Count
R1
R2
R3
R4
R5
R4,5
R6,7
MAJO(dist=81°)
BKS(dist=6.0°)
ISA(dist=2.2°)
PAS(dist=1.4°)
PFO(dist=0.6°)
0.0
2.0
4.0
6.0
8.0
10.0
12.0
Hour

Figure 2. VLP vertical channel records (upper traces) filtered between 1 and 4 mHz and synthetic (PREM model) seismograms (lower traces) of the Landers earthquake at one teleseismic station, MAJO, and four nearby stations, BKS, ISA, PAS and PFO. At all nearby stations the initial part of the records up to R1 was clipped. R2 and R3 were also clipped by the signals from the Big Bear earthquake (M_w = 6.4) which occurred about three hours after the Landers earthquake and are not shown here. BKS records are multiplied by a factor of four to make the response similar to TERRAscope stations.

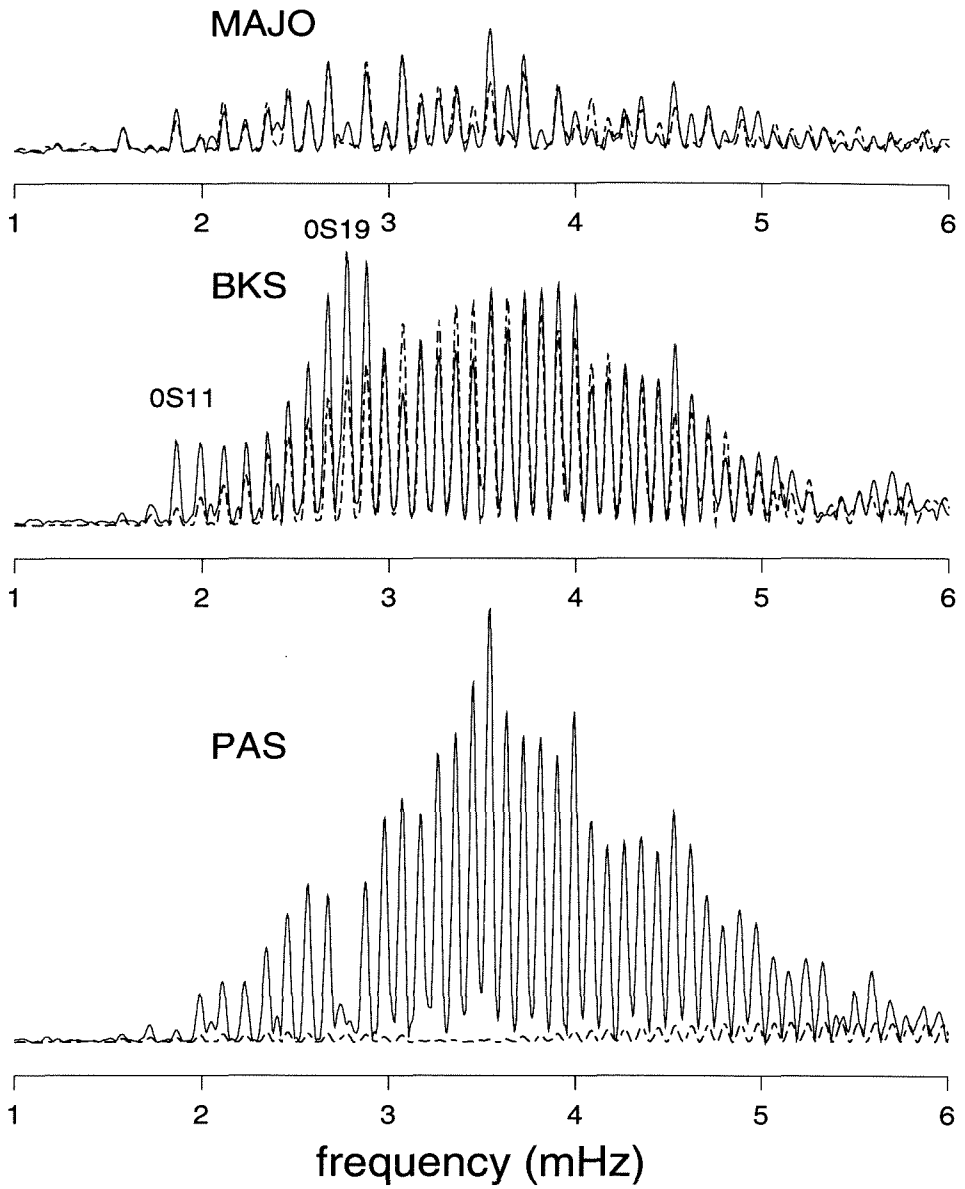

Figure 3. The Fourier spectra of Hanning–tapered VLP vertical channel records (solid line) and spherical Earth synthetic seismograms (dashed line) at MAJO, BKS and PAS. Records start at 15000 s and end at 65000 s after the origin time. Vertical axes are linear and on the same scale for all the stations. BKS records are multiplied by a factor of four.

radiation pattern of the nearly vertical strike slip mechanism. The initial part of the long–period R2,3 packet recorded at TERRAscope stations (not shown here) is as large as R4,5 packet. Horizontal component records are too noisy to be used for determination of the modal peaks in the Fourier spectra.

3. The cause of the anomalies

The non–spherical nature of the Earth such as the rotation, ellipticity and aspherical structure could cause the anomalies. Since the small amplitude of the spheroidal oscillations from a strike–slip source near the origin results from the destructive interference of waves radiating in the orthogonal directions from the source, the non–spherical nature of the Earth could reduce the degree of destructive interference, thereby increasing amplitudes at the origin. Several hours after the event, the long–period waves may be disturbed enough to make the source region non–nodal.

4. Synthetic test

To test the asphericity hypothesis, we compare long–period synthetic seismograms for a realistic Earth model with data. The epicentral and antipodal regions are the major caustics of seismic waves of a sphere. The raypath between the earthquake and seismic stations cannot be defined and conventional raypath approaches break down. We use the variational method (Park *et al.*, 1986, Tsuboi, 1992) which calculates synthetic seismograms from the eigenfunctions and eigenfrequencies of a rotating, elliptic Earth model with a three dimensional structure. The eigenfunctions and eigenfrequencies of non–spherical Earth are obtained by solving generalized eigenvalue problems of the form,

$$(V - \omega^2 T)\mathbf{x} = 0,$$

where V and T are the potential and kinetic energy matrices respectively. ω is the eigenfrequency of a 3D eigenfunction $\mathbf{x}$. The rotational energy matrix W is included

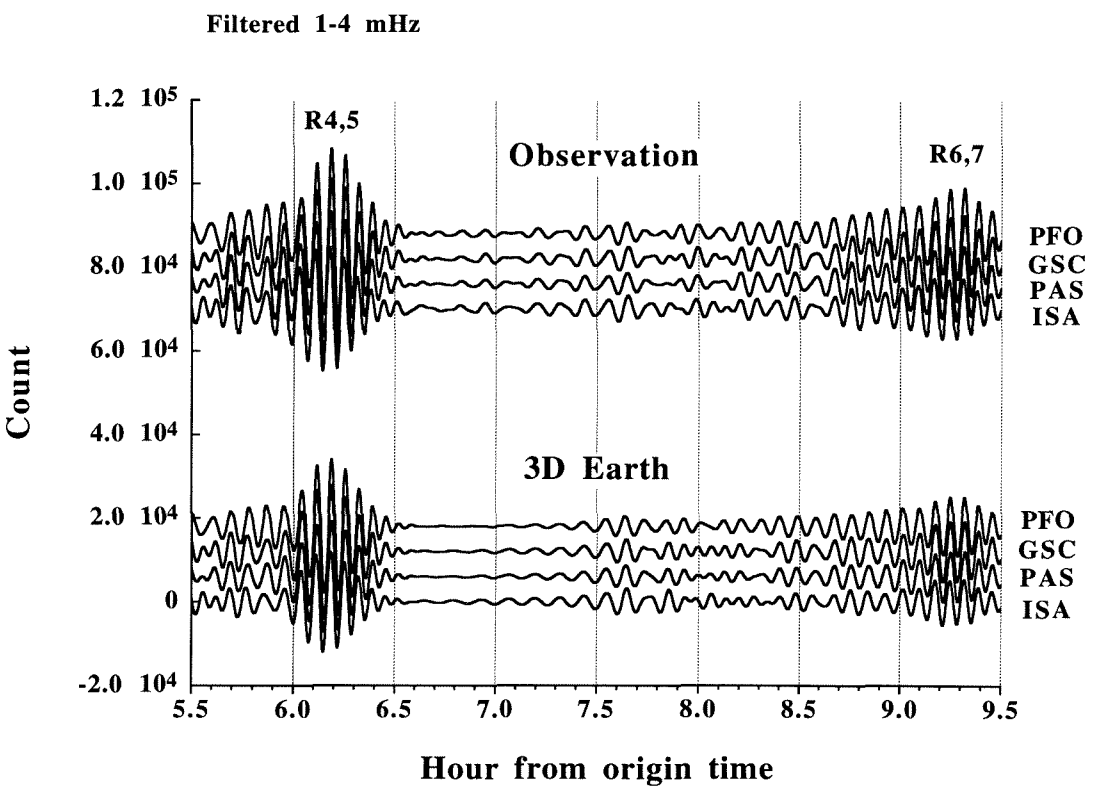

Figure 4. Top) Vertical component seismograms at TERRAscope stations. Bottom) Synthetic seismograms for rotating, elliptic and 3D earth model SH8U4L8 (Dziewonski and Woodward, 1992) at the TERRAscope stations. Both filtered between 1 and 4 mHz.

in V (Masters *et al.*, 1983). We use equivalent isotropic PREM (Dziewonski and Anderson, 1981) as a reference Earth model. Matrix elements of V, W and T are given in Woodhouse (1980) and Shibata *et al.* (1990). We include the crustal correction as velocity perturbations in the crust and boundary undulations based on the ocean function expanded up to the same order as that used for to the mantle (appendix of Woodhouse and Dziewonski, 1984). The PREM spherical attenuation structure is included in V. Five nearby spheroidal and five toroidal fundamental mode multiplets are used as a basis set to calculate a hybrid eigenfunction and eigenfrequency up to 4 mHz to take into account the effects of self coupling, fundamental mode along–branch coupling and spheroidal–toroidal (S–T) coupling. Synthetic seismograms for a whole mantle model SH8U4L8 (up to degree $l = 8$, Dziewonski and Woodward, 1992) are in good agreement with the observed records (Figure 4) and seem to explain the amplitude anomalies over a frequency range of 1.6 to at least 4 mHz (Figure 5a).

5. Sensitivity to 3D Earth models

To see the effects of the lateral heterogeneity in the mantle on the nearfield normal modes amplitudes, we also calculated non–spherical Earth synthetics for 1) rotation + ellipticity only, 2) M84A (upper mantle $l \leq 8$) (Woodhouse and Dziewonski, 1984) + rotation + ellipticity, 3) MDLSH (whole mantle $l \leq 6$) (Tanimoto, 1990) + rotation + ellipticity, 4) upper mantle part of SH8U4L8 + rotation + ellipticity, 5) SH8U4L8 + one–tenth of real rotation rate + ellipticity, 6) self coupling SH8U4L8 + rotation + ellipticity, 7) SH8U4L8 + rotation + ellipticity without crustal correction (Figure 5). All 3D Earth models include S velocity, P velocity and density perturbations scaled according to $d \ln v_p / d \ln v_s = 0.8$, $d \ln \rho / d \ln v_s = 0.4$.

Rotation and ellipticity alone cannot explain the amplitude anomalies (Figure 5b). The crustal correction has a large effect up to about 600 s (Figure 5h). Other than the crustal structure, the upper mantle heterogeneity is mainly responsible for the

large amplitude anomalies above 3 mHz (Figure 5e). As the frequency decreases the mode energy penetrates to the lower mantle whose aspherical structure can change the amplitude by a factor of two around ${}_0S_{14}$ (Figure 5e). Although self coupling explains most of the anomalies in the synthetics (Figure 5g), holes in the observed spectra around ${}_0S_{11}$ and ${}_0S_{19}$ (Figure 3 bottom) are probably caused by strong S–T coupling (Figure 5f). We also calculated normal mode amplitude anomalies for other global seismic models, M84C (upper mantle $l \leq 8$) (Woodhouse and Dziewonski, 1984), SH8WM13 (whole mantle $l \leq 8$) (Dziewonski and Woodward, 1992) and SH12WM13 (whole mantle $l \leq 12$) (Su *et al.*, 1992). M84C and both SH8WM13 and SH12WM13 predict synthetics similar to M84A and SH8U4L8, respectively. Amplitudes predicted by SH12WM13 are not larger than those by SH8U4L8.

6. Discussion

The comparable amplitudes of the initial part of R2,3 (not shown) and R4,5 observed at the TERRAscope stations indicate that long–period surface waves, longer than 250 s, are already disturbed after the wave travelled around the Earth once.

The change in the normal–mode amplitude with and without the crustal correction is about as large as that caused by the lateral heterogeneity in the mantle (Figure 5a, b and h) suggesting that the mantle structures in tomographic models without crustal correction are seriously contaminated by the crustal structure (e.g., M84A and MDLSH). Models with higher order lateral heterogeneity do not necessarily give better fits to the observed amplitude anomalies and phase. Synthetic test shows that observed anomalies are not sensitive to the truncation of spherical harmonics (e.g., SH8U4L8 and SH8WM13 extend to $l = 8$, SH12WM13 extends to $l = 12$) and parameterizations of Earth models (e.g., in SH8U4L8 the upper and lower mantles are parameterized separately; in SH8WM13 and SH12WM13 no boundary is pre-assumed in the mantle) indicating that short wave length heterogeneity ($12 \geq l \geq 8$) has little

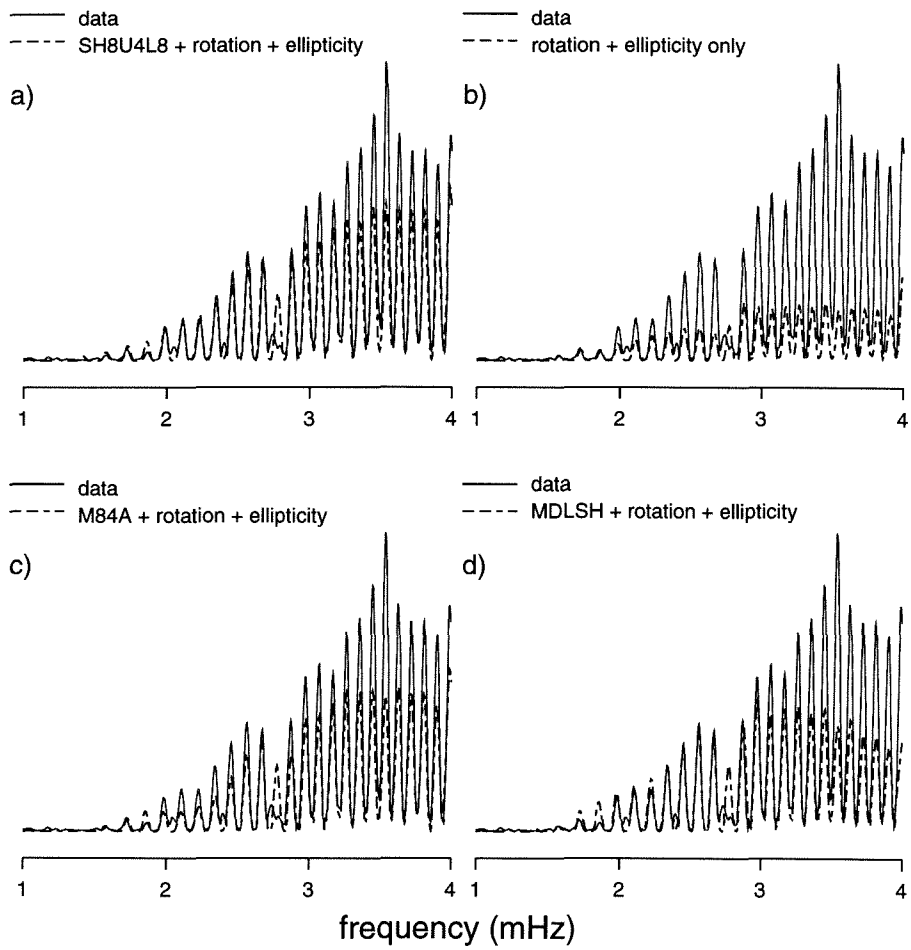

Figure 5. Synthetic spectra at PAS for various non–spherical Earth models. The Fourier spectra are taken for Hanning–tapered records starting at 15000 s ending at 65000 s after the origin time. a) is the same case as Figure 4. b)–h) are the spectra for the cases 1)–7) in the text respectively. Vertical axes indicate the linear amplitude on the same scale.

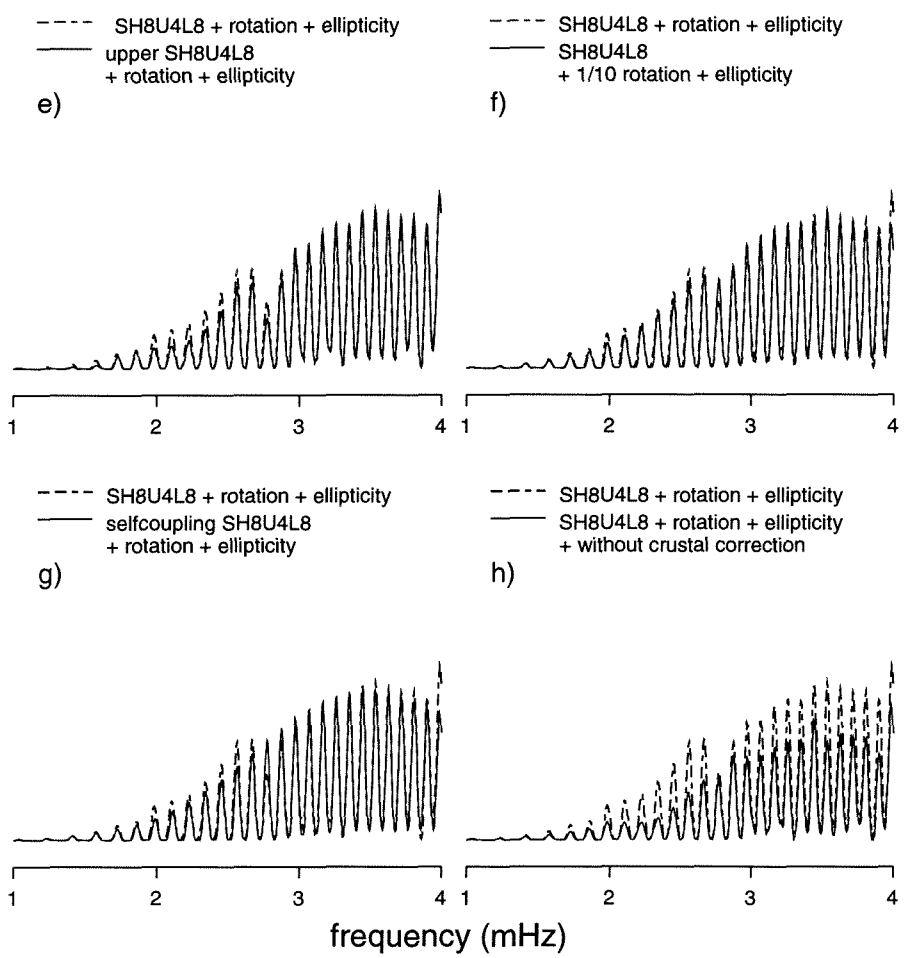

Figure 5 cont.

effects on this observation. The amplitude deficit in the synthetics compared to the observation around 3–4 mHz (Figure 5a) may be explained by the lateral heterogeneity higher than $l=13$ or by more realistic large scale crustal lateral heterogeneity.

Synthetic calculations (not shown) demonstrate that the amplitude anomalies observed at BKS are explained by strong rotational S–T coupling (Masters *et al.*, 1983).

7. Conclusion

Anomalously large long–period Rayleigh waves observed at the TERRAscope stations of the Landers earthquake can be explained by the non–spherical nature of the Earth, such as rotation, ellipticity and large scale lateral heterogeneity. The observed long–period spheroidal mode amplitudes are very sensitive to the large scale structure in the crust and the mantle structure. Below 3 mHz the lower mantle structure and the rotation of the Earth can also change the amplitudes by a factor of two or more. To assess the effect of higher order lateral heterogeneity on the amplitude anomalies near the epicenter, more precise knowledge of the large scale crustal structure is required.

8. Acknowledgements

I thank H. Kanamori, D. L. Anderson, T. Tanimoto and S. Tsuboi for useful discussions. I also thank W.-j. Su and R. L. Woodward for providing us with their whole mantle seismic models, A. Dziewonski for bringing the importance of the crustal correction to our attention, and an anonymous reviewer for valuable comments. A part of computations was supported by the JPL/Caltech supercomputing project. This research was partially supported by the U. S. Geological Survey Grant 1434–93–G–2287. This research was conducted under the TERRAscope project supported by the L. K. Whittier and Arco foundations. Contribution No. 5295 Division of Geological and Planetary Sciences, California Institute of Technology.

References

Dziewonski, A. M. and D. L. Anderson, 1981, Preliminary reference Earth model, *Phys. Earth Planet. Inter.*, **25**, 297-356.

Dziewonski, A. M. and R. L. Woodward, 1992, Acoustic imaging at the planetary scale, *Acoustical Imaging*, **19**, 785–797,

Kanamori, H., H.-K. Thio, D. Dreger, E. Hauksson and T. Heaton, 1992, Initial investigation of the Landers, California, earthquake of June 28, 1992 using TERRAscope. *Geophys. Res. Lett.*, **19**, 2267–2270.

Masters, G., J. Park and F. Gilbert, 1983, Observation of coupled spheroidal and toroidal modes, *J. Geophys. Res.*, **88**, 10285–10298.

Park, J. and F. Gilbert, 1986, Coupled free oscillations of an aspherical, dissipative, rotating Earth: Galerkin theory, *J. Geophys. Res.*, **91**, 7241–7260.

Shibata, N., N. Suda and Y. Fukao, 1990, The matrix element for a transversely isotropic earth model *Geophys. J. Int.*, **100**, 315–318.

Su, W.-J., R. L. Woodward and A. M. Dziewonski, 1992, Joint inversions of travel–time and waveform data for the 3-D models of the Earth up to degree 12, *EOS. Trans. Am. Geophys. Un.*, **73**, 201.

Tanimoto, T., 1990, Long–wavelength S–wave structure throughout the mantle, *Geophys. J. Int.*, **100**, 327–336.

Tsuboi, S., 1992, Amplitude anomalies of surface waves from the July 16, 1990, Philippine Island earthquake, *Geophys. Res. Lett.*, **19**, 341–344.

Woodhouse, J. H., 1980, The coupling and attenuation of nearly resonant multiplet in the Earth's free oscillation spectrum *Geophys. J. Astron. Soc.*, **61**, 261–283.

Woodhouse, J. H. and A. M. Dziewonski, 1984, Mapping the upper mantle: Three dimensional modeling of Earth structure by inversion of seismic waveforms, *J.*

Geophys. Res., **89**, 5953–5986.

Woodward, R. L., A. M. Forte, W.-J. Su and A. M. Dziewonski, 1993, Constraints on the large–scale structure of the Earth's mantle, in *Evolution of the Earth and Planets*, E. Takahashi, R. Jeanloz and D. Rubie eds., *Geophys. Mono. 74, Am. Geophys. Un.*, 89–109.

PART II-B

The cause of nearfield normal mode amplitude anomalies of the Landers earthquake

Abstract

We modeled the interaction of the source mechanism and the station location with large-scale lateral heterogeneity using the splitting matrix of an isolated multiplet and the 'source-receiver function' whose spherical harmonic coefficients are given by P_{st} where s and t are angular and azimuthal order numbers respectively. For a short period of time waveform perturbation is proportional to the integral of products of the splitting function with harmonic coefficients C_{st} and the 'source-receiver' function. For the Landers earthquake and TERRAscope stations source–receiver geometry, the 'source-receiver function' is dominated by the low-order components, particularly l=2, m=$\pm$2 in the epicentral coordinates. This beach-ball like pattern is the same for all the near–source stations located in different quadrants of the strike-slip mechanism. The two maxima of the 'beach ball' pattern coincide with the locations of the degree 2 maxima of the splitting functions; the western Pacific and east of South America. These features explain the weak dependence of the waveforms on higher order lateral heterogeneity and similarity of waveforms over the epicentral region. The location and the source mechanism of the Landers earthquake relative to the large scale lateral heterogeneity l=2, including the variations of the cruatal structures, are responsible for the cause of amplitude anomalies near the epicenter. However, the amplitude near the epicenter of an earthquake with a thrust fault type mechanism, for example the Northridge earthquake, is explained well with a spherical Earth model.

1. Introduction

After several hours after the 1992 landers earthquake, large spheroidal mode amplitude anomalies near the epicentral region ($\Delta \leq 3^o$) of the earthquake (dip=74^o, rake=-176^o, strike 340^o, Kanamori *et al.*, 1992), California, at periods up to about 600 s were observed. The amplitude anomalies can be explained by the currently available large scale three dimensional seismic tomographic models (Watada *et al.*, 1993; Tsuboi and Um, 1993; Hara and Geller, 1994). For a point source with a vertical strike slip source mechanism Rayleigh wave amplitude is expected to be small near the epicenter and its antipode if we assume that the Earth is spherically symmetric, because the epicenter is on the excitation node of the spheroidal mode for this source mechanism. The variations of average surface wave phase velocity along the great circles containing the epicenter result in the incomplete cancellation of surface waves converging from all directions near the epicenter after the waves travel around the Earth once or more. The spatial concentration of surface wave energy in the epicentral area causes large amplitude anomalies of the surface waves.

In this paper we develop a model to understand the interaction of the source mechanism and the station location with large–scale lateral heterogeneity, and its effect on the amplitude near the source. Hara and Geller (1994) performed numerical experiments and showed that a large scale lateral variation of seismic velocity, angular order l =2 and azimuthal order $m\pm2$ in the epicentral coordinates, can cause amplitude anomalies near the epicenter for a vertical strike slip. Watada *et al.* (1993) reported the results of computations for various 3D Earth models. They showed that amplitude anomalies are insensitive to the short wavelength ($l \geq 8$) lateral heterogeneity and very sensitive to the crustal structure.

Using the model developed here we isolate the aspherical structure of the Earth which caused the surface wave amplitude anomalies of the Landers earthquake. Syn-

thetic seismograms are computed for the structure which is responsible for the anomalies, and are compared with the observation.

2. Model

Watada *et al.* (1993) compared the spectral amplitude of synthetic seismograms with and without multiplet coupling, elliptic shape and rotation of the Earth. They showed that self coupling is the largest contribution to the amplitude anomalies near the epicenter of the Landers Earthquake and none of multiplet coupling, ellipticity and rotation of the Earth changes the amplitude significantly at frequences higher than 3 mHz. In the following discussion we assume that multiplets are isolated, and ignore the multiplet coupling, ellipticity and rotation of the Earth.

The contribution of a particular isolated multiplet with angular order l to an observed seismogram can be written as a function of time t (Woodhouse and Girnius, 1982; Giardini *et al.*, 1988)

$$u(t) = Re(\exp(i\omega_o t)\ \mathbf{r}\ \exp(iHt)\ \mathbf{s}), \qquad 1$$

where ω_o is the reference frequency of the multiplet, $\mathbf{r}$ is the receiver vector, $\mathbf{s}$ is the source vector. Both $\mathbf{r}$ and $\mathbf{s}$ are $2l+1$ dimension complex vectors whose m-th element $(-l \leq m \leq l)$ are given by,

$$r_m = \sum_{N=-1}^{1} R_N {Y_l}^{N\,m}(\theta_r, \varphi_r) \qquad 2$$

and

$$s_m = \sum_{N=-2}^{2} S_N {Y_l}^{N\,m}(\theta_s, \varphi_s), \qquad 3$$

where ${Y_l}^{N\,m}(\theta_r, \varphi_r)$ is the generalized spherical harmonics of Phinney and Burridge (1973), (θ_r, φ_r) and (θ_s, φ_s) are the spherical coordinates of the receiver and the source, respectively. R_N and S_N are given explicitly in Woodhouse and Girnius (1982). $\mathbf{s}$

depends on the source moment tensor and **r** depends on the instrument orientation and incorporates the instrument response.

The splitting matrix H is a square matrix with dimension $2l+1$ which can be written as

$$H_{mm'} = \omega_o \sum_{s=0,\text{even}}^{2l} \sum_{t=-s}^{s} \gamma_{ls}^{mm't} c_{st} \qquad 4$$

and

$$\gamma_{ls}^{mm't} = (2l+1)\sqrt{\frac{2s+1}{4\pi}} \begin{pmatrix} l & l & s \\ 0 & 0 & 0 \end{pmatrix} (-1)^m \begin{pmatrix} l & l & s \\ -m & m' & t \end{pmatrix}. \qquad 5$$

The quantity in a pair of large parentheses is the Wigner 3-j symbol defined, for example, in Edmonds (1960).

The coefficient c_{st} in eq. 4 depends linearly on the Earth's internal heterogeneity of spherical harmonic degree s and order t, through the expression of the form

$$c_{st} = \int_0^a \delta \mathbf{m}_{st}(r) \cdot \mathbf{M}_s(r) dr + \sum_d \delta h_{st}^d H_s^d \qquad 6$$

where $\mathbf{M}_s(r), H_s^d$ are the kernels for a spherical harmonic component of the lateral heterogeneity. $\delta \mathbf{m}_{st}$ is the volumetric perturbations of P- and S-wave velocities and density, and δh_{st}^d is the topography at the dth discontinuity. The formula for $M_s(r)$ and H_s are found in Woodhouse and Dahlen (1978). Giardini *et al.* (1988) introduced a visual representation of the splitting coefficients. A splitting function, which is defined by

$$\eta(\theta, \varphi) = \sum_{s=0,even}^{2l} \sum_{t=-s}^{s} c_{st} Y_l^m(\theta, \varphi), \qquad 7$$

where $Y_l^m(\theta, \varphi)$ is the completely normalized spherical harmonics defined in Edmonds (1960), is seen as a projected lateral heterogeneity of the interior onto the Earth's surface with weighting $M_s(r)$ and H_s. Figure 1 shows the splitting function of a spheroidal mode, ${}_0S_{30}$, for a three dimensional tomographic model, SH8U4L8 of Dziewonski and Woodward (1992).

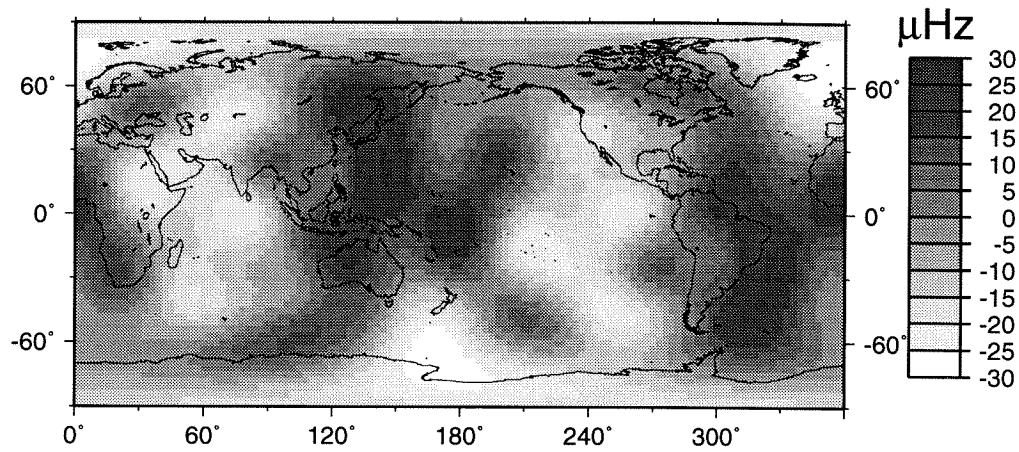

Figure 1. The splitting function of mode $_0S_{30}$ computed for a whole mantle 3D tomographic model, SH8U4L8 (Dziewonski and Woodward, 1992). The spherical harmonic components of the splitting function have only even angular orders up to l =8. Crustal correction is included.

For a short period of time eq. 1 is approximately

$$\begin{aligned} u(t) &\simeq Re(\exp(i\omega_o t)\ \mathbf{r}\ (I + iHt)\ \mathbf{s}) \\ &= Re(\exp(i\omega_o t)\mathbf{r}\ \mathbf{s} + it\exp(i\omega_o t)\mathbf{r}H\mathbf{s}), \end{aligned} \tag{8}$$

where I denotes the unit matrix with dimension $2l+1$. The first term is the contribution of the spherical Earth and the second term expresses the contribution from the lateral heterogeneity. In most cases, the magnitude of the second term relative to that of the first term, determinant of H, is of the order of lateral perturbation of the Earth, about 10^{-2}-10^{-3}. Therefore, in many cases, the use of a spherical Earth model is a good approximation in the computation of synthetic seismograms. In special cases when $\mathbf{r}$ and $\mathbf{s}$ are nearly orthogonal, the second term becomes important.

The generalized spherical harmonics $Y_l^{N\,m}(\theta,\varphi)$ is a matrix element of the finite rotation D of angular momentum with angular order l

$$\begin{aligned} Y_l^{N\,m}(\theta,\varphi) &= D^l_{N\,m}(0,\theta,\varphi) \\ &= d^l_{N\,m}(\theta)\exp(im\varphi), \end{aligned} \tag{9}$$

where $d^l_{N\,m}(\theta)$ is expressed by (eq. 4.1.15 in Edmonds, 1960)

$$d^l_{N\,m}(\theta) = \sqrt{\frac{(l+N)!(l-N)!}{(l+m)!(l-m)!}} \cdot \sum_\sigma \binom{l+m}{l-N-\sigma}\binom{l-m}{\sigma}(-1)^{l-N-\sigma}\left(\cos\frac{\theta}{2}\right)^{2\sigma+N+m}\left(\sin\frac{\theta}{2}\right)^{2l-2\sigma-N-m}. \tag{10}$$

From the binomial coefficients in eq. 10, σ should be in the range of

$$-N-m \le \sigma \le l-m. \tag{11}$$

Then the power of $\sin\frac{\theta}{2}$ should be in the range of

$$m-N \le 2l-2\sigma-N-m \le 2l+N+m. \tag{12}$$

As θ approaches zero, the dominant term in eq. 10 is the one that has the least power of $\sin\frac{\theta}{2}$, namely $(\sin\frac{\theta}{2})^{m-N}$.

For a vertical strike slip source, the source vector **s** has non–vanishing values only for the components $m = \pm 2$ in the epicentral coordinates. Because the receiver vector of a vertical component sensor has only $N = 0$ term in eq. 2, in the epicentral coordinates the receiver vector **r** of the vertical component of a station close to the epicenter has non–vanishing value only for the component $m = 0$. Thus the spherical Earth contribution, which is proportional to **r s**, vanishes for a vertical strike slip source and the vertical component of a station located near the epicenter. In this case the contribution from the aspherical structure becomes important.

The contribution from the aspherical structure is proportional to

$$\sum_{mm'} r_m H_{mm'} s_{m'}. \qquad 13$$

Again, in the epicentral coordinates for a vertical strike slip source and vertical component seismograms near the epicenter, r_m, m=0, and $s_{m'}$, $m' = \pm 2$ components have non–zero value. From eqs.4 and 5 and the selection rule of the Wigner 3–j symbol, namely $-m + m' + t = 0$ and s = even, eq. 13 has non–zero value only when s = even and $t = -m'$. That is, only a part of the lateral heterogeneity, which has even angular order s and azimuthal order $m = \pm 2$ components, contributes to the amplitude anomalies near the epicenter. Hara and Geller (1994) investigated the Born approximation expression of the excitation of singlets by a strike–slip source in a similar way, and reached the same statement.

We extend the evaluation of eq. 13 for both nearfield and farfield stations and for general earthquake source mechanisms. We rearrange eq. 13 as

$$\begin{aligned} \sum_{mm'} r_m H_{mm'} s_{m'} &= \sum_{st} \sum_{mm'} r_m \gamma_{ls}^{mm't} c_{st} s_{m'} \\ &= \sum_{st} {p_{st}}^* c_{st} \qquad 14 \\ &= \int \xi^*(\theta, \varphi)\, \eta(\theta, \varphi) \Omega, \qquad 15 \end{aligned}$$

where * denotes complex conjugate and the surface integral covers the whole surface of the Earth. We have introduced in the expression above a new function $\xi(\theta, \varphi)$, we call the source–receiver function, which is defined by

$$\xi(\theta, \varphi) = \sum_{st} p_{st} Y_l^m(\theta, \varphi), \qquad 16$$

and p_{st}, we call the source–receiver coefficient, are given by

$$p_{st} = \sum_{mm'} r_m \gamma_{ls}^{mm't} s_{m'}. \qquad 17$$

Because of the symmetries of $\gamma_{ls}^{mm't} = \gamma_{ls}^{-m\ -m'\ -t}$, $r_m = (-1)^m r_{-m}^*$ and $s_{m'} = (-1)^m s_{-m'}^*$, the source–receiver coefficient has a symmetry of $p_{s\ -t} = (-1)^t p_{st}^*$ and therefore the source–receiver function $\xi(\theta, \varphi)$ is real everywhere. The amplitude anomalies can be modeled by two functions defined on the surface of the Earth; one is the 3D structure of the Earth, which is expressed by the splitting function $\eta(\theta, \varphi)$, and the other is the configuration of a station and an earthquake including their locations and the sensor component and the source mechanism, which is expressed by the source–receiver function $\xi(\theta, \varphi)$. For a short period of time after the earthquake the amplitude perturbation is proportional to the surface integrals of the product of the splitting function and the source–receiver function.

3. Application

The source–receiver function of the ${}_0S_{30}$ mode shown in Figure 2 is computed for the Landers earthquake source and the vertical component at the Pasadena station at angular order 30. In the power spectrum of this source–receiver function, two sharp peaks exist at l=2 and 60 (Figure 3). The peak at l=2 for the Landers earthquake and the vertical component PAS geometry agrees with the qualitative discussion in section 1. The peak at l=60 indicates that the vertical component amplitude near

the epicenter of the Landers earthquake is also sensitive to the lateral heterogeneity, with a horizontal scale of half the wavelength of the mode.

The heterogeneity of the Earth's interior is dominated by long–wavelength features; the power of the large scale seismic heterogeneity of the Earth decreases with angular order. Tanimoto (1991) showed that the power spectrum of surface wave phase velocity maps has a secondary peak at l=5, 6 and decreases with l^{-1} at higher orders. Su and Dziewonski (1992) displayed that the power of a body wave travel time residual map decays more quickly at l higher than l=6$\sim$8. Because the amplitude perturbation is the product of the source–receiver function and the splitting function (eq. 15), we assume that the contribution from the peak at l=60 is small and negligible. In Figure 4 we plot the low–pass filtered (l<9) source–receiver functions for the vertical component at PAS and the Landers earthquake configuration, and the vertical component at MAJO and the Landers earthquake configuration. Their power spectra are shown in Figure 5. The l=2, m= $\pm$2 components of the source-receiver function in the epicentral coordinates are dominant for the vertical component at PAS and the Landers earthquake. The orientation of the $m = \pm 2$ term, the 'beach ball'–like pattern in the source–receiver function, is controlled by the source mechanism. The zero-line of the source–receiver function is parallel to the strike of the vertical slip source mechanism. For all the nearfield stations located in different quadrants of the strike–slip source mechanism of the Landers earthquake, the source–receiver functions show a very similar pattern but with different magnitude. This feature explains the observation of Watada *et al.* (1993) that the waveforms of long–period Rayleigh waves from the Landers earthquake observed at the nearfield stations within a different quadrant of the source mechanism are very similar with each other.

For farfield stations, the source–receiver function shows broad ridge-like and trough-like patterns along the great circle passing through the earthquake and station

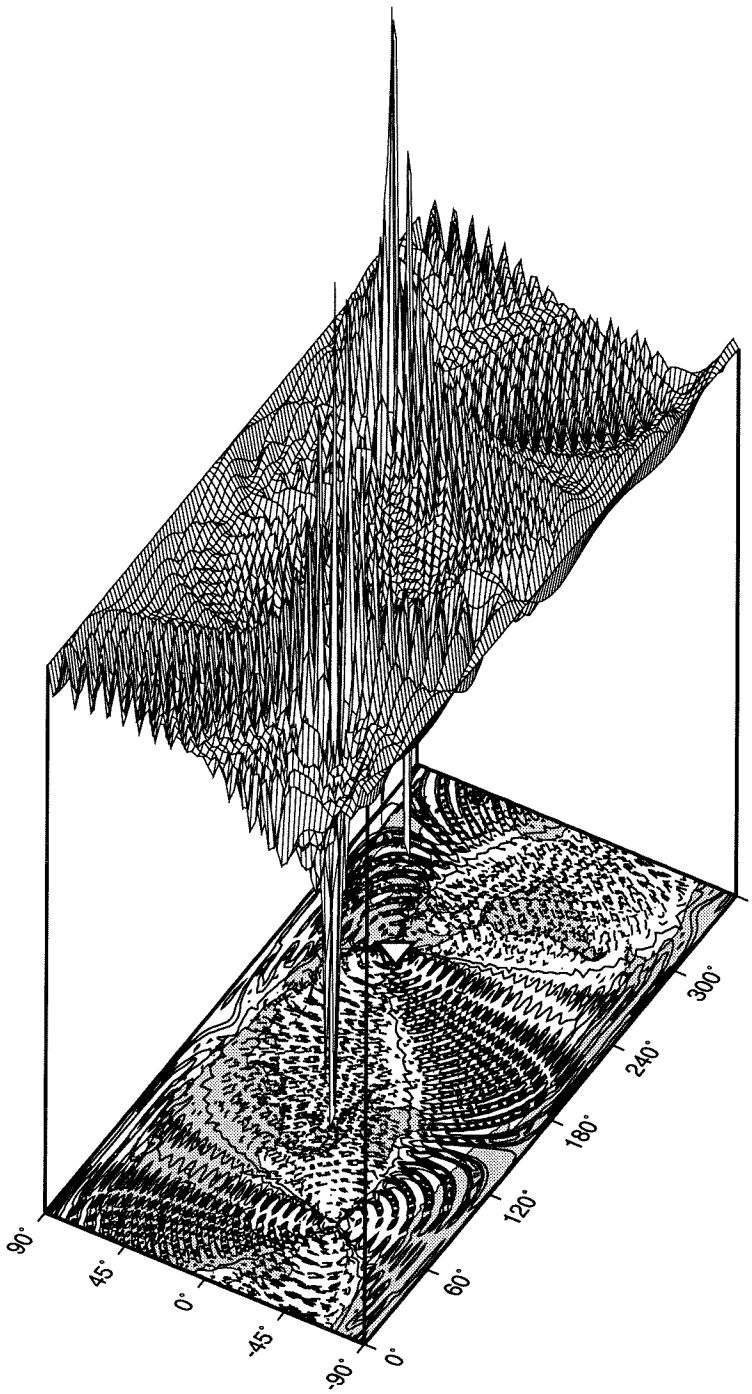

Figure 2. The source–receiver function for the vertical component of PAS and the Landers earthquake location with its source mechanism. The vertical scale is linear and its scale is arbitrary.

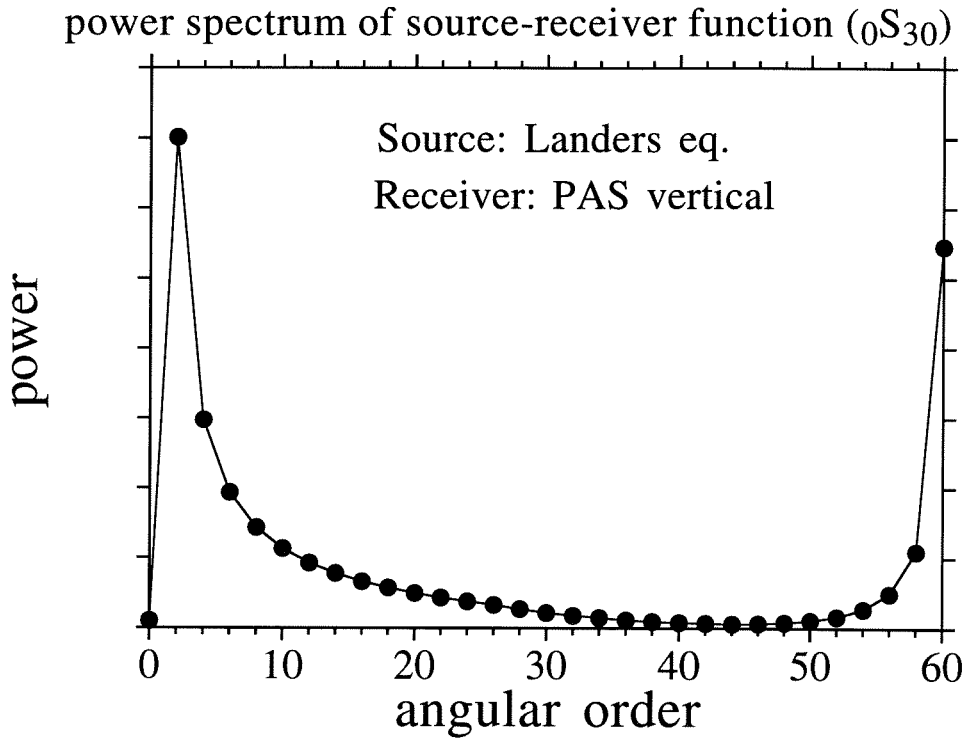

Figure 3. The power spectrum of the source–receiver function plotted in Figure 2. The power at angular order s is computed by $\sum_t p_{st}{}^* \; p_{st}$. The vertical scale is linear and its unit is arbitrary.

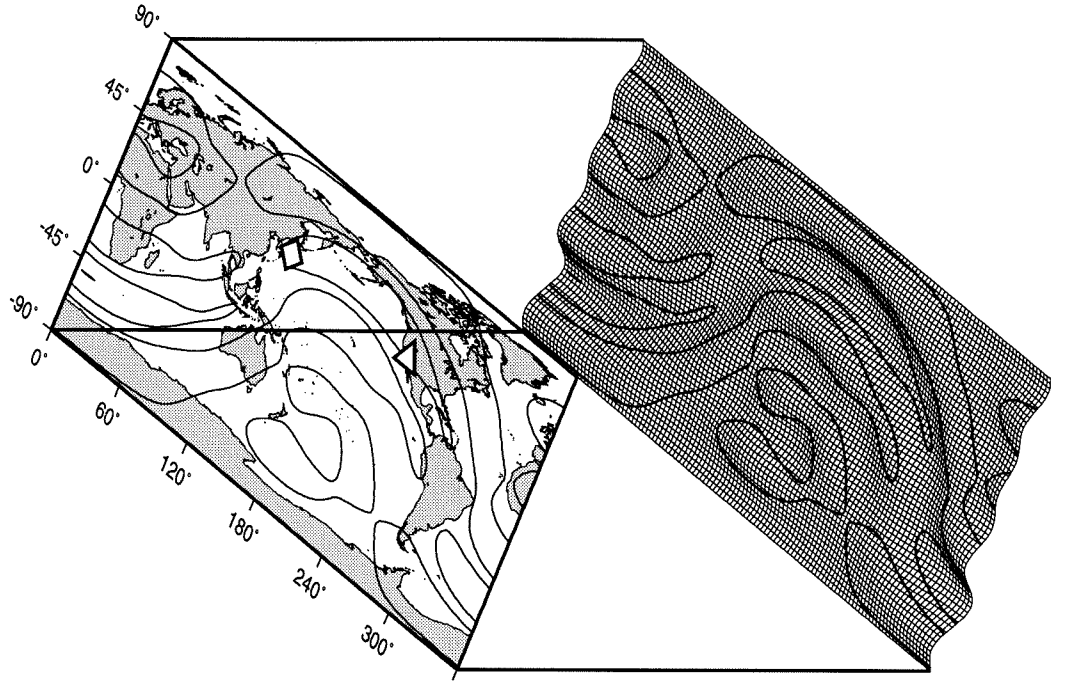
90°
45°
0°
-45°
-90°
0°
60°
120°
180°
240°
300°

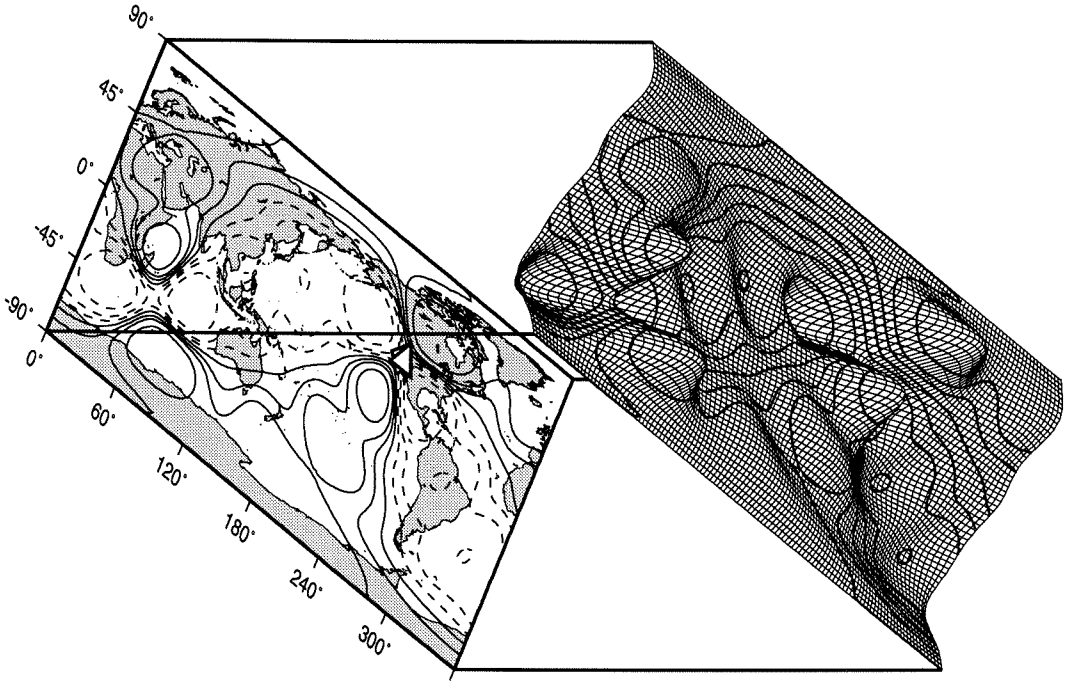
90°
45°
0°
-45°
-90°
0°
60°
120°
180°
240°
300°

Figure 4. The low–pass filtered l <9 source–receiver functions for the Landers earthquake and; left, for the vertical component of the MAJO station (36.5^{o}N, 138.2^{o}E), Japan. right, for the vertical component of the PAS station (34.1^{o}N, 118.2^{o}W), USA. While triangles and diamonds indicate station and earthquake locations, respectively. Both plots are in the same linear scale and its unit is arbitrary.

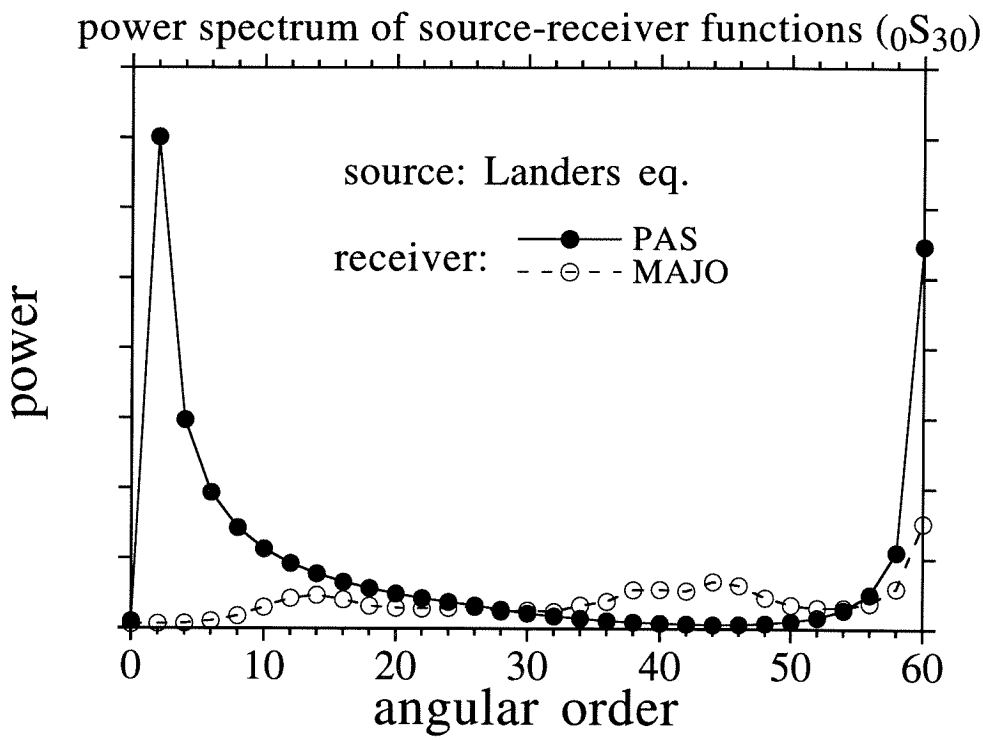

Figure 5. The power spectrum of the source–receiver functions for the vertical component at PAS and MAJO and for the Landers earthquake. The spectrum for PAS is the same as in Figure 3. Both plots are in the same linear scale and its unit is arbitrary.

locations (Figure 5). This is consistent with the picture that the structure along the great circle connecting the station and the earthquake affects the frequency of the normal modes (Jordan, 1978). What Woodhouse and Girnius (1982) called kernel in their study is very similar to the source–receiver function we introduced here.

Since both the splitting function and the source–receiver function have a peak in the power spectrum at l=2, if the patterns of the $l = 2$ component of each function are similar, or in other words the coefficients of two functions are 'parallel' in the sense of the vector operation in eq. 14, we expect large amplitude anomalies at the nearfield stations of the Landers earthquake. Figure 6 plots the source–receiver function for the vertical ground motion at PAS of the Landers earthquake and the splitting function for the SH8U4L8 tomographic model. Only the l=2 components are used in these plots. The two maximum regions in each l=2 pattern coincide; both have one peak in the western Pacific and another peak east of South America.

4. Synthetic test

We computed synthetic seismograms to confirm whether the l=2 pattern is responsible for the cause of the amplitude anomalies. The long–period seismogram for a 3D Earth model including only self coupling contribution from the l=2 lateral heterogeneity component, and one including all coupling effects from all lateral heterogeneity l<9, are compared with observation (Figure 7). The waveforms of R4,5 and R6,7 packet are well reproduced in both synthetic seismograms, indicating that self coupling caused by the very large scale structure (l=2) is the origin of the nearfield amplitude anomalies of the Landers earthquake.

Because the source–receiver function includes the information of the earthquake source mechanism, the nearfield amplitude of the spheroidal mode will change for an earthquake at the same location but with a different source mechanism. If the orientation of the vertical strike slip of the Landers earthquake differs by 45 degrees, the

(a)

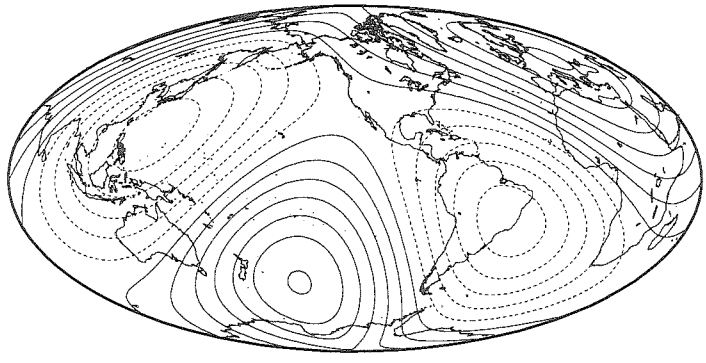

(b)

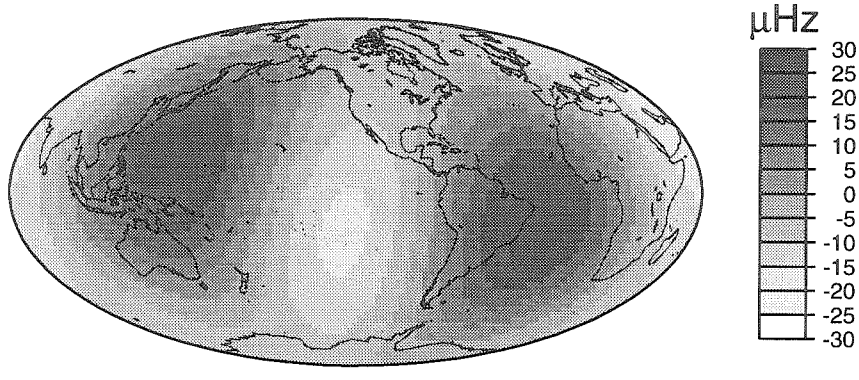

Figure 6. (a) l=2 component of the source receiver function in Figure 3 and 5. (b) l=2 component of the splitting function in Figure 1.

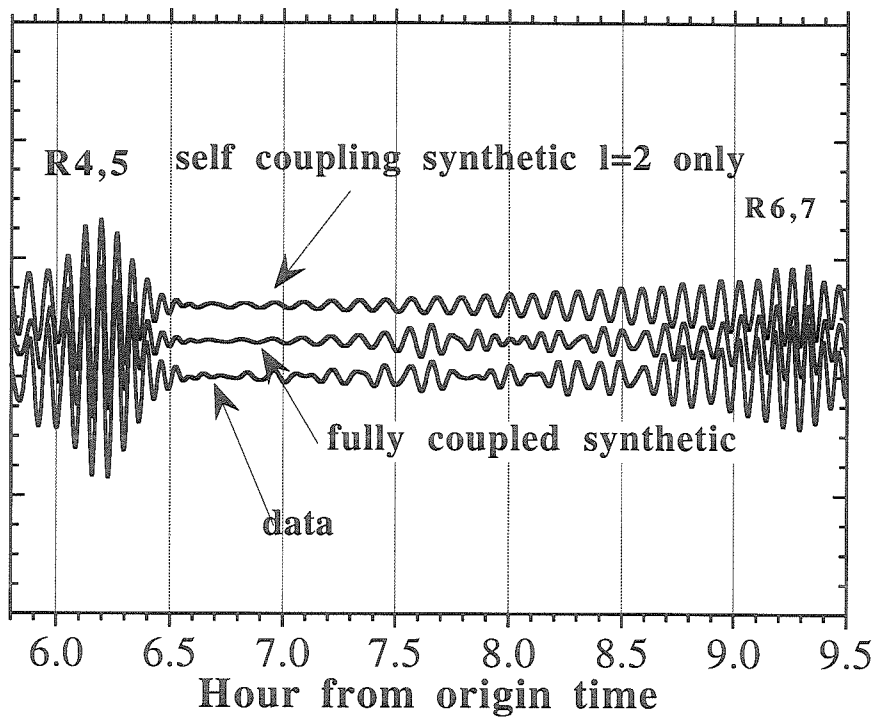

Figure 7. Vertical component seismograms at PAS for the Landers earthquake. Top) self coupling synthetic seismogram using only the l=2 component of lateral heterogeneity of the SH8U4L8 model. Middle) Synthetic seismogram computed by the variational method which takes into account self coupling, multiplet coupling effects. The SH8U4L8 tomographic model is used. Bottom) filtered VLP channel data recorded at PAS. All traces are filtered between 1–4 mHz.

two patterns of the l=2 component of $\eta(\theta, \varphi)$ and $\xi(\theta, \varphi)$ become nearly 'orthogonal' and the amplitude would be small. We performed synthetic tests of the rotated strike slip mechanisms for a tomographic 3D model (Figure 8).

The amplitude anomaly in the synthetic seismograms for pure strike–slip source mechanisms reaches its maximum at two strike angles. The orientations of the strike of these two mechanisms are 90 degrees apart and the polarity of waveforms is flipped. The strike of the Landers earthquake is 340 degrees, near the maximum. If we have a large strike slip earthquake with a strike angle of about 110 degrees along the San Andreas fault in Southern California, we will observe smaller amplitude anomalies near the epicenter, a few times larger than the spherical Earth predictions, instead of ten times as we have seen for the Landers earthquake.

In Figure 8 the amplitude of the surface waves one hour before the arrival of the R4,5 packet reaches its minimum when the amplitude of the R4,5 packet reaches maximum, and vice versa. The time one hour before R4,5 corresponds to the arrival time of the G4,5 packet in the horizontal component. These waves showed up on the arrival of the G packet are the Love waves appeared in the vertical component. For a strike–slip source mechanism, the directions of the maximum Rayleigh wave radiation are at the minima of Love wave radiation and vice versa, therefore Love wave amplitude anomaly reaches its maximum in the horizontal component when Rayleigh wave amplitude is minimum and larger Love waves appear on the vertical component through spheroidal–toroidal coupling. Similar waveforms, G6,7 in the vertical component, were displayed in the fully coupled synthetic seismogram and the observed waveforms in Figure 7 about 7.6hours after the origin time. When we take into account self coupling, spheroidal–spheroidal multiplet coupling but not spheroidal–toroidal coupling, these Love waves in the vertical component disappear.

For a strike–slip source, the aspherical Earth is responsible for the nearfield

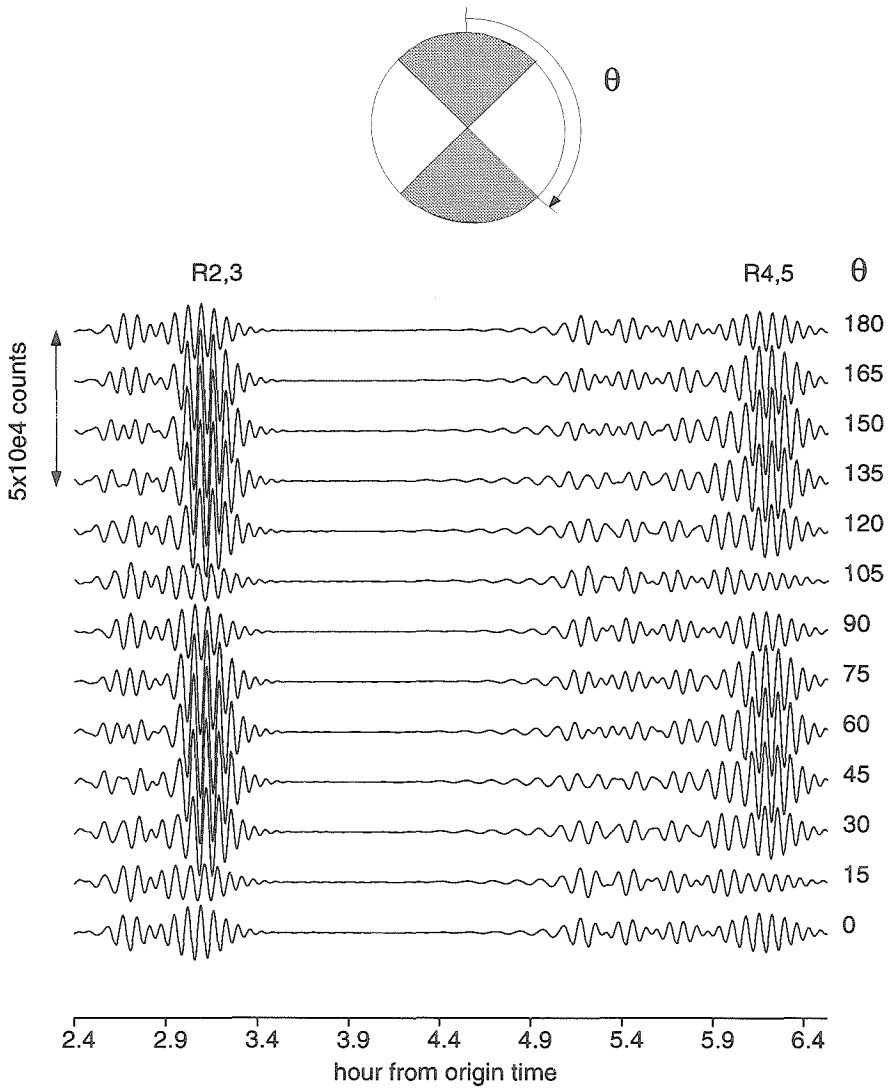

Figure 8. Synthetic seismograms of PAS vertical component for purely vertical strike–slip sources located at the epicenter of the Landers earthquake. Seismograms are filtered between 1–4 mHz. Seismograms are computed by the variational method which takes into account self coupling, multiplet coupling effects. The SH8U4L8 tomographic model is used

amplitude anomalies and the spherical Earth does not contributes to the anomalies. For a thrust or normal fault type source mechanism, on the other hand, the contribution from the spherical Earth, the first term in eq. 8, is much larger than the contribution from the aspherical Earth, the second term in eq. 8, therefore we expect little amplitude anomalies near the epicenter of an earthquake with these types of source mechanisms. The 1994 Northridge earthquake occurred in Southern California with a thrust fault type source mechanism (Figure 9). Lateral heterogeneity has little effect on the amplitude of synthetic seismograms of Rayleigh wave packets near the epicenter and the observed waveforms are explained well with the 1D Earth model (Figure 10).

5. Crustal effect

We have shown that very large scale lateral heterogeneity is responsible for the nearfield amplitude anomalies, although, the vertical extent of the lateral heterogeneity is not addressed yet. Watada *et al.* (1993) reported that the synthetic seismograms of the nearfield of the Landers earthquake change their amplitude by about a factor of two with and without crustal correction. The amount of amplitude change is as large as the one caused by the heterogeneity of the whole mantle.

Because the Landers earthquake may be a special case in which the crustal correction effect is enhanced and results in the amplitude anomalies, we cannot argue that the crustal correction is also as important as the whole mantle heterogeneity for other combinations of stations and earthquakes. To see whether the crustal structure is as important as the mantle structure in general, we plot the splitting width of fundmental spheroidal mode multiplets for various 3D models with and without crustal correction (Figures 11 and 12).

The splitting width is purely determined by the 3D Earth model and independent of the source mechanism. The source mechanism determines the excitation of

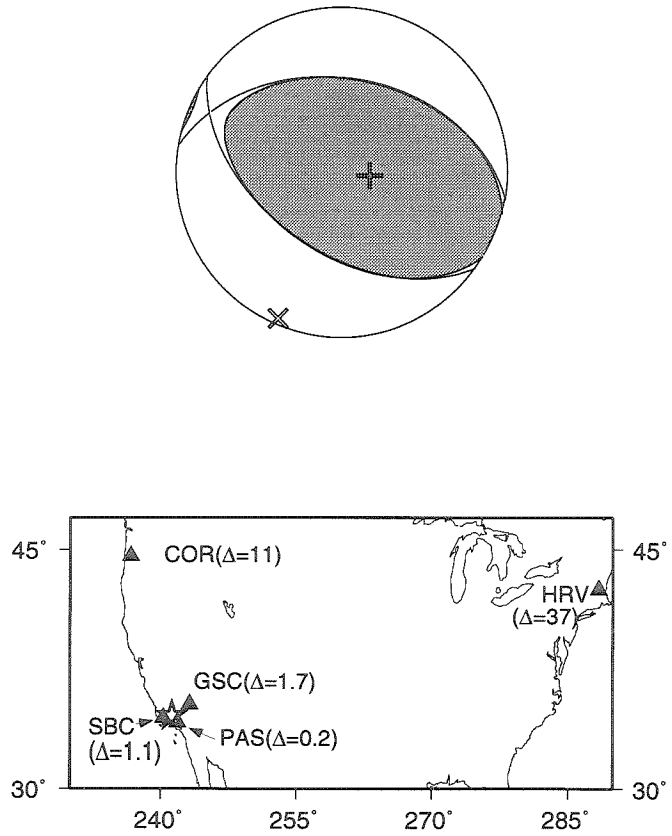

Figure 9. Top: the Northridge earthquake (1994/01/17 12:31:2.1 GMT, 34.56^{o}N, 118.76^{o}W, M_w=6.6) occurred also in Southern California. The source mechanism is thrust (strike =126^o, dip=50^o, slip=108^o). Bottom: five broadband stations in North America appeared in Figure 10.

(a)

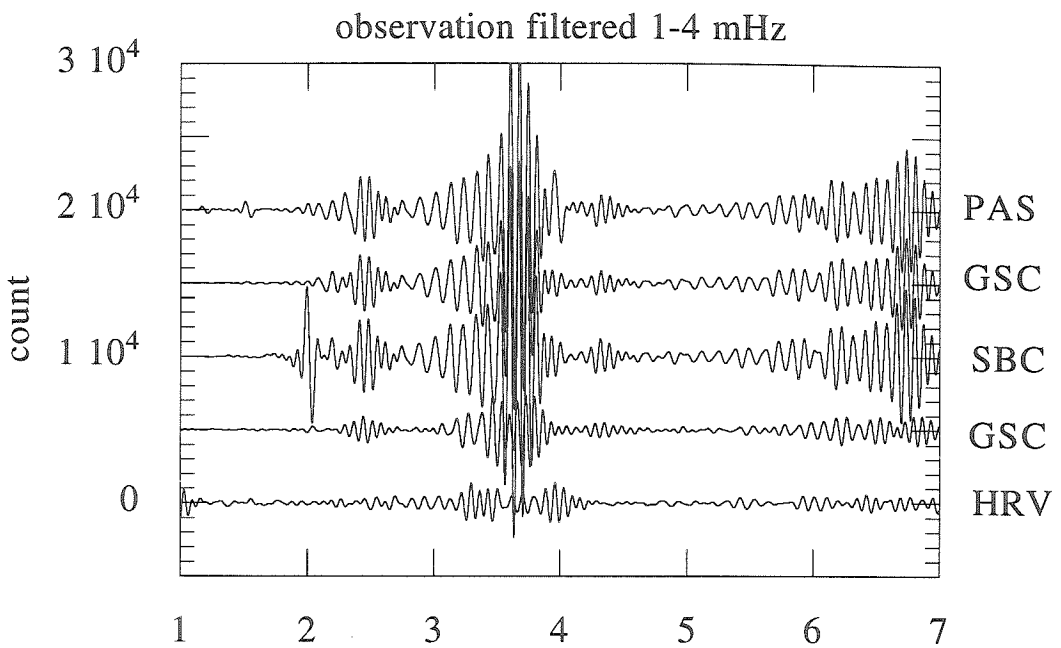
observation filtered 1-4 mHz
3 10^4
2 10^4
1 10^4
0
count
PAS
GSC
SBC
GSC
HRV
1
2
3
4
5
6
7

(b)

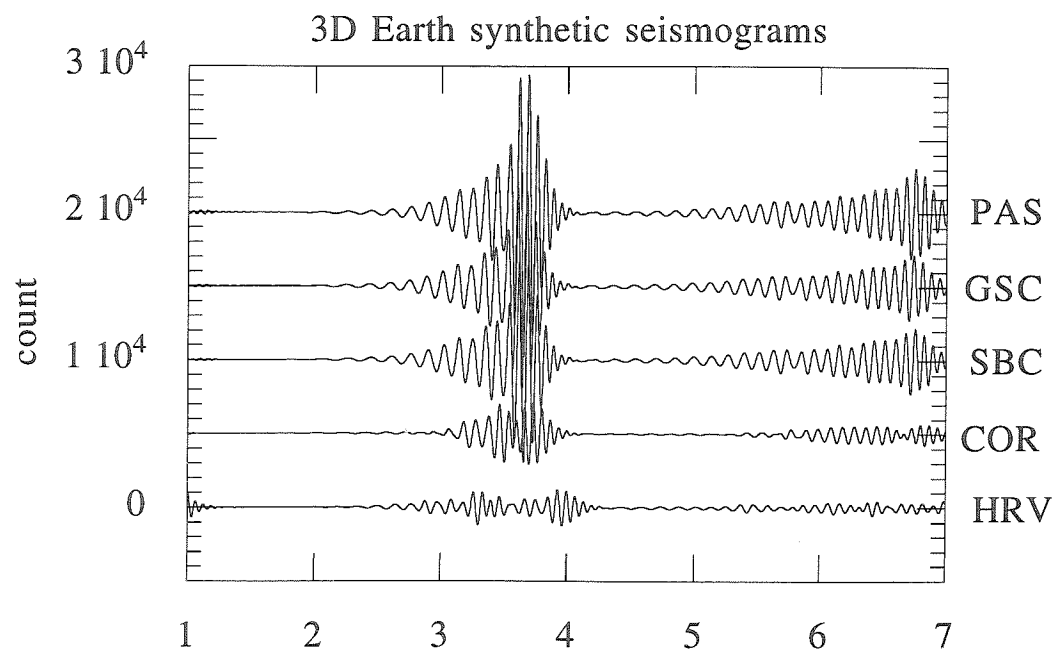
3D Earth synthetic seismograms
3 10^4
2 10^4
1 10^4
0
count
PAS
GSC
SBC
COR
HRV
1
2
3
4
5
6
7

(c)

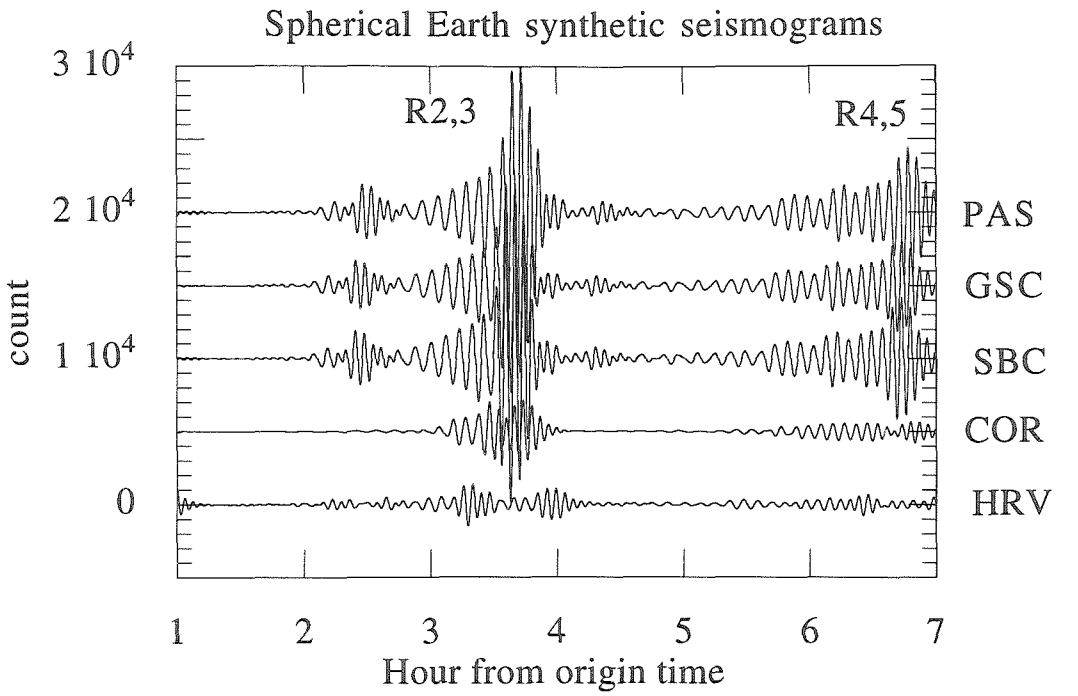

Figure 10. Vertical component VLP channel records in North America (a) filtered between 1 and 4 mHz and synthetic seismograms; (b) for 3D Earth model SH8U4L8 (Dziewonski and Woodward, 1992) and (c) for 1D Earth model PREM (Dziewonski and Anderson, 1981). The spike at 2hours after the origin time in SBC data is due to an aftershock glitch. In the computation of 1D Earth synthetic seismograms overtones are included.

singlets within a multiplet. The larger splitting width indicates larger lateral seismic velocity variations in the 3D Earth model. Many 3D seismic velocity mantle models were obtained by the inversion after the crustal effects were modeled and subtracted from the waveform residuals. These mantle models, if the corrected crustal structure is not included in the splitting width computation, predict erroneously large splitting (Figures 11 and 12). For example, a fundamental spheroidal mode with l=43 or T$\sim$200 s without the crustal correction splits about 40 % wider than the one with the correction (Figure 11). The splitting width difference for a mantle model with and without the crustal correction grows as the wavelength of the spheroidal mode becomes shorter because a mode with large l is more sensitive to the shallower structure, *i.e.*, lateral heterogeneity in the crust. However, even for low–order spheroidal modes, for example l=10 (T$\sim$ 600 s), the crustal correction can change the splitting width by about 20 %.

The variation of the splitting width for various 3D models is much smaller than the change of the splitting width with and without including the crustal correction for a mantle 3D model. In Figure 11, the splitting width of fundamental spheroidal modes for two tomographic models, whole mantle model SH12WM13 of Su *et al.* (1994) and upper mantle model M84A of Woodhouse and Dziewonski (1984), are compared. The splitting width predicted by M84C differs several percent at $l \geq 10$ from the one by SH12WM13. For low angular order l <10 the difference increases because the low–order modes are sensitive the deeper mantle structure. But at very low angular order the difference decreases because the rotational splitting becomes dominant.

This large crustal effect on the splitting width is consistent with the non–negligible crustal corrections, such as surface topography and the variations of Moho depth, for the phase velocity measurements of long–period surface waves. It has been

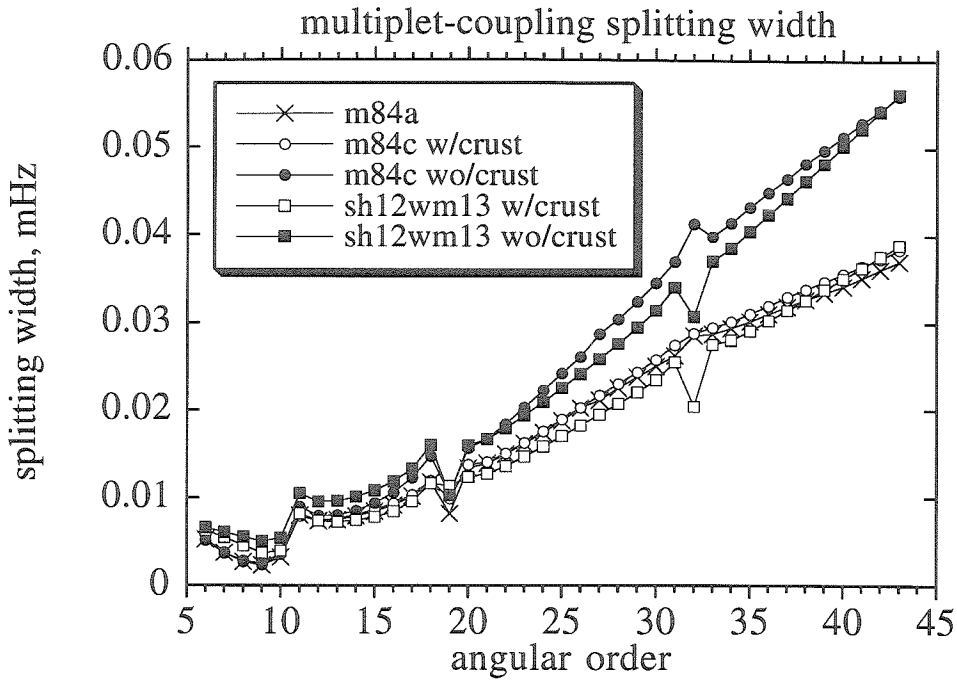
multiplet-coupling splitting width
m84a
m84c w/crust
m84c wo/crust
sh12wm13 w/crust
sh12wm13 wo/crust
splitting width, mHz
angular order
0.06
0.05
0.04
0.03
0.02
0.01
0
5
10
15
20
25
30
35
40
45

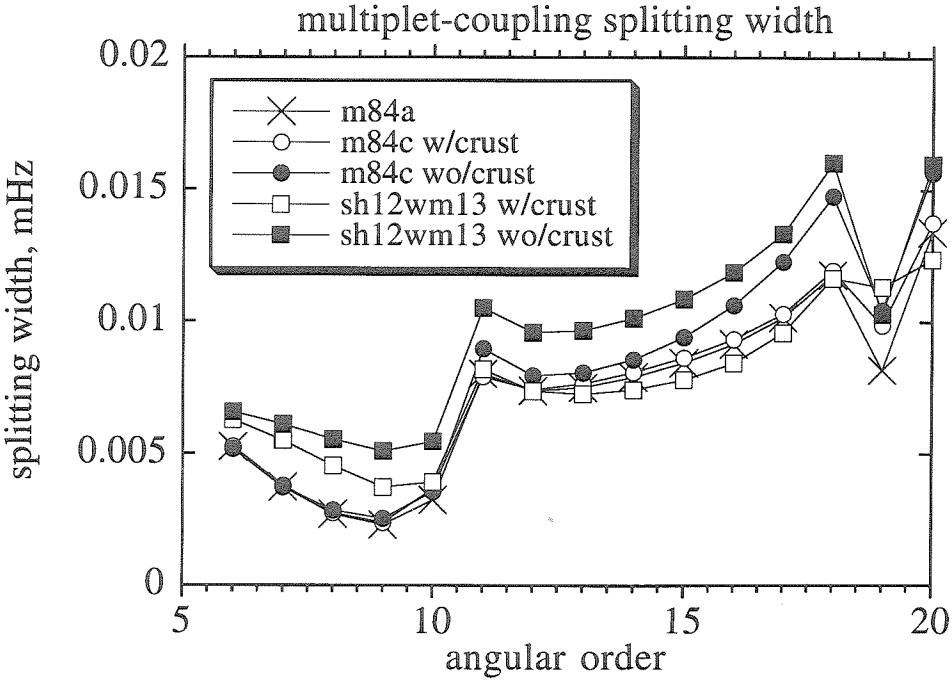
multiplet-coupling splitting width
m84a
m84c w/crust
m84c wo/crust
sh12wm13 w/crust
sh12wm13 wo/crust
splitting width, mHz
angular order
0.02
0.015
0.01
0.005
0
5
10
15
20

Figure 11. Splitting width of fundamental spheroidal mode multiplets computed for various mantle models with and without crustal correction. Splitting width is defined by the real part of the difference between the maximum and minimum eigenfrequencies within the multiplet. Symbols indicate; cross, upper mantle model M84A (Woodhouse and Dziewonski, 1984) in which crustal correction is not considered in the inversion; circle, upper mantle model M84C (Woodhouse and Dziewonski, 1984) in which crustal effect is subtracted before the inversion; square, whole mantle model SH12WM13 (Su *et al.* 1994) in which crustal effect is subtracted before the inversion. Black symbols indicate that for which we did not include the crustal structure in the calculation of the splitting width. In the calculation the effects of rotation, ellipticity, spheroidal–toroidal coupling and fundamental mode along–branch coupling are included.

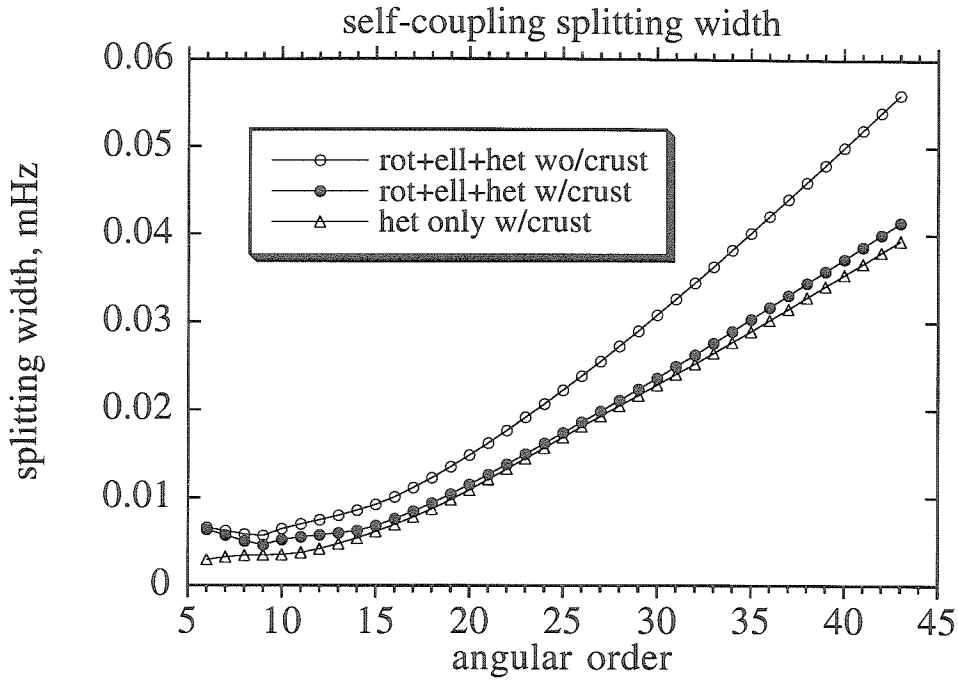
self-coupling splitting width
splitting width, mHz
0.06
0.05
0.04
0.03
0.02
0.01
0
5
10
15
20
25
30
35
40
45
angular order
rot+ell+het wo/crust
rot+ell+het w/crust
het only w/crust

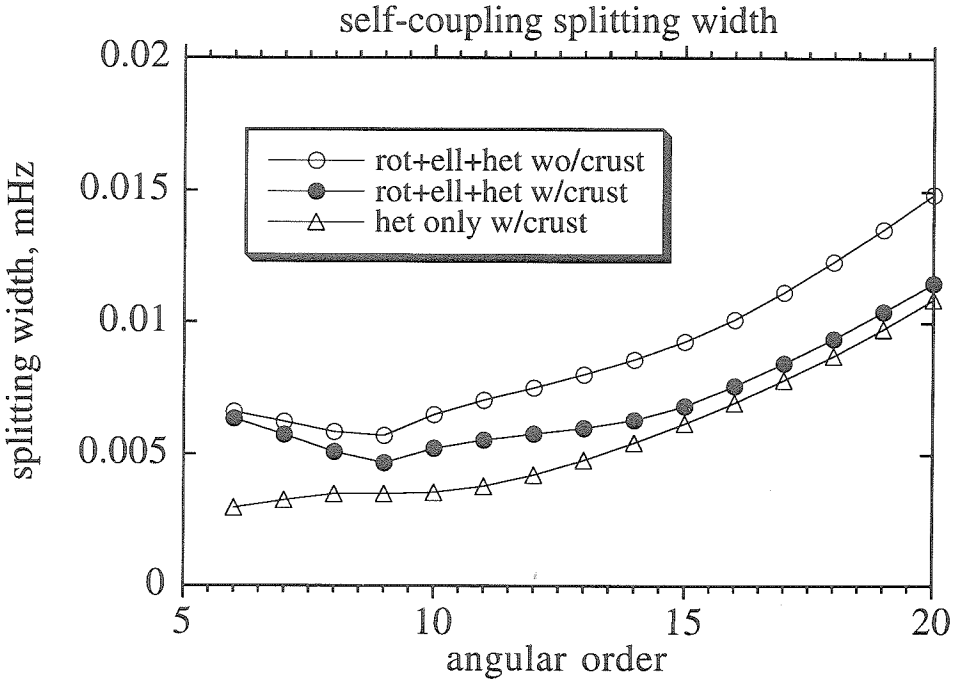
self-coupling splitting width
splitting width, mHz
0.02
0.015
0.01
0.005
0
5
10
15
20
angular order
rot+ell+het wo/crust
rot+ell+het w/crust
het only w/crust

Figure 12. Splitting width of fundamental spheroidal mode multiplets computed for a whole mantle model, SH12WM13 of Su *et al.* (1994). Black circles indicate that Earth rotation, ellipticity and the mantle model with crustal correction are included in the computation. White circles indicate same as black circles except the mantle model without crustal correction. White triangles indicate same as black circles except that rotation and ellipticity are not included. In the calculation coupling with other multiplets is ignored.

known that in the analysis of surface wave propagation including the effect of the lateral variation of seismic velocities, the crustal structure as well as the mantle structure should be take into account. Nataf *et al.* (1986) noticed that the contribution from the crustal thickness variation is a dominant factor in the phase velocity variations of long–period surface waves; the effect is quite important even for 300 s Rayleigh waves.

6. Discussion and conclusion

The nearfield spheroidal mode amplitude anomalies of the Landers earthquake are caused by the very large scale lateral heterogeneity of the Earth, in terms of spherical harmonics, l=2 and $m\pm$2 components in the epicentral coordinates.

The orientation of the strike–slip source mechanism of the Landers earthquake controls the l=2 pattern which describes where the surface waves, recorded near the epicenter after traveling around the Earth, are sensitive to the lateral heterogeneity. The lateral heterogeneity filtered by the pattern determines the amplitude near the source. For the location and the source mechanism of the Landers earthquake, the 'beach ball' pattern has two peaks; one in the western Pacific and the other east of South America. The lateral heterogeneity of the Earth also has peaks at these geographical regions and thus contributes to the large amplitude anomalies near the epicenter. This amplitude anomaly is probably the first direct observation of l=2, $m\pm$=2 components of the lateral seismic velocity variation. A good agreement of synthetic seismograms using only l=2 component with observation suggests that l=2 $m\pm$2 components are successfully constructed in the current seismic tomographic models.

The fault ruptured unilaterally from south to east during the Landers earthquake over a fault length 65 km with an average rupture velocity 2.7 km/s (Wald and Heaton, 1994). Because the fault length is much smaller than the wavelength of the

long-period (1-4 mHz) surface waves $\geq$ 1000 km, we ignored the fault size finiteness and the rupture directivity effect in this study. The method to compute synthetic seismograms for a unilateral horizontally laying line source outlined in Woodhouse (1983) can be incorporated in the variational method to simulate the long-period ground motions in Southern California during the Landers earthquake with a line source for an aspherical Earth model. The confirmation of the validity of our negligence of the fault finiteness is a future research topic.

The Northridge earthquake showed no evidence of any amplitude anomalies. This observation is explained by the thrust–fault type source mechanism. For a strike–slip mechanism, the Rayleigh amplitude for a spherical Earth vanishes at the epicenter and a small aspherical Earth perturbation results in the large amplitude near the epicenter because of the imperfect cancellation of surface waves. For a thrust or normal fault type mechanism, the Rayleigh wave amplitude reaches its maximum near the epicenter and the antipode for a spherical Earth. An aspherical Earth structure can cause a small phase perturbation of the large amplitude surface waves but not results in the substantial amplitude change.

Large–scale variations of the crustal structures also contribute to the nearfield amplitude anomalies. The change of the splitting of the fundamental spheroidal modes when we incorrectly include the crustal structure is much larger than the splitting width variations for different tomographic 3D Earth models, even at 300 s. Therefore we need to carefully subtract the crustal effect in long–period surface waves when we determine the structure in the mantle from surface wave data.

7. Acknowledgements

We are grateful to Drs. T. Hara and R. J. Geller for sending us a preprint of their paper prior to the publication. We also thank Dr. A. Hales for telling us that he is amused by this research. His words encouraged us a lot.

References

Dziewonski, A. M. and D. L. Anderson, 1981, Preliminary reference Earth model, *Phys. Earth Planet. Inter.*, **25**, 297–356.

Dziewonski, A. M. and R. L. Woodward, 1992, Acoustic imaging at the planetary scale, *Acoustical Imaging*, **19**, 785–797.

Edmonds, A. R., 1960, *Angular Momentum in Quantum Mechanics*, Princeton University Press, New Jersey.

Giardini, D., X.-D. Li and J. H. Woodhouse, 1988, Splitting functions of long–period normal modes of the Earth, *J. Geophys. Res.*, **93**, 13716–13742.

Hara, T. and R. J. Geller, 1994, Anomalously large near–field Rayleigh waves excited by the 1992 Landers, California, earthquake, *Bull. Seismol. Soc. Am.*, 84, 751–760.

Jordan, T. H., 1978, A procedure for estimating lateral variation from low–frequency eigenspectra data, *Geophys. J. Astron. Soc.*, **52**, 441–455.

Kanamori, H., H.-K. Thio, D. Dreger, E. Hauksson and T. Heaton, 1992, Initial investigation of the Landers, California, earthquake of 28 June 1992 using TERRAscope. *Geophys. Res. Lett.*, **19**, 2267–2270.

Phinney, R. A. and R. Burridge, 1973, Representation of the elastic–gravitational excitaion of a spherical Earth model by generalized spherical harmonics, *Geophys. J. Astron. Soc.*, **34**, 451–487.

Su, W.-J. and A. M. Dziewonski, 1992, On the scale of mantle heterogeneity, *Phys. Earth Planet. Inter.*, **74**, 29–54.

Su, W.-J., R. L. Woodward and A. M. Dziewonski, 1994, Degree 12 model of shear velocity heterogeneity in the mantle, *J. Geophys. Res.*, **99**, 6945–6980.

Tanimoto, T., 1991, Predominance of large–scale heterogeneity and the shift of velocity anomalies between the upper and lower mantle, *J. Phys. Earth*, **38**, 493–509.

Tsuboi, S. and J. Um, 1993, Anomalous amplification of the Earth's normal modes near the epicenter due to lateral heterogeneity, *Geophys. Res. Lett.*, **20**, 2379–2382.

Wald, J. D. and T. H. Heaton, 1994, Spatial and temporal distribution of splip for the 1992 Landers, California, earthquake, *Bull. Seismol. Soc. Am.*, **84**, 668–691.

Watada, S., H. Kanamori and D. L. Anderson, 1993, An analysis of nearfield normal mode amplitude anomalies of the Landers earthquake, *Geophys. Res. Lett.*, **20**, 2611–2614.

Woodhouse, J. H., 1983. The joint inversion of seismic waveforms for lateral variations in Earth structure and earthquake source parameters, *Proc. Enrico Fermi Inst. Sch. Phys.*, **85**, 366–397.

Woodhouse, J. H. and F. A. Dahlen, 1978, The effect of a general aspherical perturbation on the free oscillations of the Earth, *Geophys. J. Astron. Soc.*, **53**, 335–354.

Woodhouse, J. H. and T. P. Girnius, 1982, Surface waves and free oscillations in a regionalized earth model, *Geophys. J. Astron. Soc.*, **68**, 653–673.

Woodhouse, J. H. and A. M. Dziewonski, 1984, Mapping the upper mantle: Three–dimensional modeling of Earth structure by inversion of seismic waveforms, *J. Geophys. Res.*, **89**, 5953–5986.

APPENDIX A

Synthetic seismogram for an aspherical Earth model

In this appendix we show how synthetic seismograms for an aspherical Earth model are computed. The governing equation of elasto-gravitational oscillations of a non–rotating elastic body is formally expressed as (Woodhouse, 1983)

$$\left(\mathcal{H} + \rho\frac{\partial^2}{\partial t^2}\right)\mathbf{u}(\mathbf{x},t) = \mathcal{F}(\mathbf{x},t), \qquad 1$$

where

$\mathcal{H}$: integro-differential operator acting on the spacial domain of the Earth

ρ density distribution

$\mathbf{u}$ displacement vector field

$\mathcal{F}$ external body force.

$\mathcal{H}$ includes the effect of elastic force and gravitational force. The expression of $\mathcal{H}$ for a slightly aspherical Earth model is found, for example, Woodhouse and Dahlen (1978). We take $\mathbf{v}_i(\mathbf{x})$ as a complete set of spatial functions, but not necessarily orthogonal. By expanding eq. 1 with this basis set and integrating over the Earth with $\int \mathbf{v}_j{}^\dagger(\mathbf{x})\ dV$, † denotes transpose and complex conjugate, we obtain an equation

$$\sum_i \left(< j|\mathcal{H}|\ i > + < j|\rho|i > \frac{\partial^2}{\partial t^2}\right) c_i(t) = F_j(t), \qquad 2$$

where $C_i(t)$ is the expansion coefficients of $\mathbf{u}(x,t)$;

$$\mathbf{u}(\mathbf{x},t) = \sum_i c_i(t)\mathbf{v}_i(\mathbf{x}),$$

$F_j(t)$ is defined by

$$F_j(t) = \int \mathbf{v}_j{}^\dagger \mathcal{F}(\mathbf{x},t)\ dV$$

and symbol $< j|A|i >$ means

$$< j|A|i > = \int \mathbf{v}_j{}^\dagger A\mathbf{v}_i\ dV.$$

Or a matrix form

$$\left(H + T\frac{\partial^2}{\partial t^2}\right)\mathbf{c}(t) = \mathbf{F}(t), \qquad 3$$

where

$$H_{ij} =< i|\mathcal{H}|j >,$$

$$T_{ij} =< i|\rho|j > .$$

Woodhouse (1983) solved eq. 3 in the time domain. We solve eq. 3 by the Laplace transform method. The Laplace transform, $\mathcal{L}$, of eq. 3 is obtained by integrating with $\int_0^\infty e^{-st}\ dt$. The result is expressed formally as

$$\left(H + s^2 T\right) \tilde{\mathbf{c}}(s) = \tilde{\mathbf{F}}(s), \qquad 4.$$

where

$$\tilde{\mathbf{c}}(s) = \mathcal{L}\left\{\mathbf{c}(t)\right\} = \int_0^\infty e^{-st}\mathbf{c}(t)dt,$$

$$\tilde{\mathbf{F}}(s) = \mathcal{L}\left\{\mathbf{F}(t)\right\} = \int_0^\infty e^{-st}\mathbf{F}(t)dt.$$

In order to get solution $\tilde{\mathbf{c}}(s)$ in s domain, we have to solve $(H + s^2T)^{-1}$. We define a generalized eigenvalue problem

$$HA = \Lambda^2 TA,$$

$$B^\dagger H = \Lambda^2 B^\dagger T, \qquad 5$$

where the columns of A are the right eigenvectors of a generalized eigenvalue problem of the form $(H - {\lambda_i}^2 T)\mathbf{a}_i = 0$ and columns of B are the left eigenvectors of a generalized eigenvalue problem of the form $\mathbf{b}_j{}^\dagger(H - {\lambda_j}^2 T) = 0$ and ${\Lambda^2}_{ij} = {\lambda_i}^2\delta_{ij}$. For a given eigenvalue there are left and right eigenvectors (Golub and Van Loan, 1989). We find that

$$({\lambda_i}^2 - {\lambda_j}^2)(\mathbf{b}_j{}^\dagger T\mathbf{a}_i) = 0$$

because

$$\mathbf{b}_j{}^\dagger H\mathbf{a}_i = {\lambda_i}^2\mathbf{b}_j{}^\dagger T\mathbf{a}_i = {\lambda_j}^2\mathbf{b}_j{}^\dagger T\mathbf{a}_i.$$

If we assume that there is no degeneracy in the eigenvalues, the kinetic energy potential T and the potential energy matrix H can be simultaneously diagonalized with

the left and right eigenvectors;

$$B^{\dagger}TA = J, \tag{6}$$

$$B^{\dagger}HA = B^{\dagger}TA\Lambda^2 = \Lambda^2 J, \tag{7}$$

where J is the diagonal matrix defined by the above equations, not the unit matrix I. When H and T are hermitian, $A = B$ and $A^{\dagger}TA = J$. From eqs. 6 and 7 we can express $(H + s^2T)^{-1}$ by

$$\begin{aligned}\left(H + s^2T\right)^{-1} &= A\left(\Lambda^2 + s^2I\right)^{-1} A^{-1}T^{-1} \\ &= A\left(\Lambda^2 + s^2I\right)^{-1} J^{-1}B^{\dagger}\end{aligned} \tag{8}$$

Using

$$\mathcal{L}^{-1}\left\{\frac{1}{\lambda^2 + s^2}\right\} = \frac{1}{\lambda}\sin\lambda t,$$

we can invert $\tilde{\mathbf{c}}(s)$ for $\mathbf{c}(t)$

$$\mathbf{c}(t) = \int_0^t A\Lambda^{-1} \begin{pmatrix} \ddots & & O \\ & \sin\lambda_0(t-t') & \\ O & & \ddots \end{pmatrix} A^{-1}T^{-1}\mathbf{F}(t')\,dt'.$$

By integrating by parts we obtain

$$\mathbf{c}(t) = \int_0^t A\Lambda^{-2} \begin{pmatrix} \ddots & & O \\ & 1-\cos\lambda_i(t-t') & \\ O & & \ddots \end{pmatrix} A^{-1}T^{-1}\dot{\mathbf{F}}(t')\,dt', \tag{9}$$

where $\dot{\mathbf{F}} = \frac{\partial \mathbf{F}}{\partial t}$. For a step time-function earthquake source

$$\dot{\mathbf{F}}(t) = \delta(t)\mathbf{F},$$

eq. 9 becomes

$$\begin{aligned}\mathbf{c}(t) &= A\Lambda^{-2} \begin{pmatrix} \ddots & & O \\ & 1-\cos\lambda_i t & \\ O & & \ddots \end{pmatrix} A^{-1}T^{-1}\mathbf{F} \\ &= -Re\left(A\Lambda^{-2}e^{i\Lambda t}A^{-1}T^{-1}\mathbf{F}\right).\end{aligned} \tag{10}$$

In the last equation we have neglected the static deformation. The acceleration is given by

$$\begin{aligned} \ddot{\mathbf{c}}(t) &= Re(Ae^{i\Lambda t}A^{-1}T^{-1}\mathbf{F}) \quad \text{or} \\ &= Re(Ae^{i\Lambda t}J^{-1}B^{\dagger}\mathbf{F}). \end{aligned} \tag{11}$$

The choice of a set of complete spatial functionals $\mathbf{v}_i(\mathbf{x})$ is arbitrary. In the real computation we cannot sum infinite number of $\mathbf{v}_i$ and we truncate the dimension of the basis set. If we take spatial grid points as a basis set, this approach is a finite element method. For the long-period oscillation of the Earth, we take the eigenfunctions of a spherical Earth model as a basis set because in order to have the same accuracy in eq. 3 we need fewer number of basis for the eigenfunctions of a spherical Earth model than we need for other complete sets. Hereafter we use $\mathbf{v}_{k,m}(\mathbf{x})$ to specify a singlet of the spherical Earth model in terms of multiplet index k, which incorporates spheroidal or toroidal mode type and overtone number n and angular order l, and azimuthal order m.

Synthetic seismogram $u(t)$ at $\mathbf{x}_r$ excited by an earthquake at $\mathbf{x}_s$ is given by

$$\begin{aligned} u(t) &= Re(\mathbf{R}(\mathbf{x}_r)\mathbf{u}(\mathbf{x},t)) \\ &= -Re(\mathbf{R}(\mathbf{x}_r)A\Lambda^{-2}e^{i\Lambda t}J^{-1}B^{\dagger}\mathbf{S}(\mathbf{x}_s)) \\ &= -Re\frac{\mathbf{R}Ae^{i\Lambda t}B^{\dagger}\mathbf{S}}{\Lambda^2 B^{\dagger}TA}. \end{aligned} \tag{12}$$

Receiver vector $\mathbf{R}(\mathbf{x}_r)$ incorporates the sensor orientation and the response of the seismometer at $\mathbf{x}_r$ including the effect of the free air gravity change by the vertical displacement and the gravity potential perturbation (Gilbert, 1980), and earthquake source vector $\mathbf{S}(\mathbf{x}_s)(=\mathbf{F})$ incorporates the source mechanism at $\mathbf{x}_s$. The vector elements of $\mathbf{R}_k$, $\mathbf{S}_k$ for a multiplet are given in Woodhouse and Girnius (1982). In the variational method (Park and Gilbert, 1986) $\mathbf{R}$ and $\mathbf{S}$ are extended to include a set of multiplets near the target multiplet in the frequency domain. In our computation five fundamental spheroidal modes and five fundamental toroidal modes are used. The matrix elements of H and T for an elliptic rotating aspherical Earth are constructed

from the expression of Z in eq. 16 of Woodhouse (1980) as

$$H = {\Lambda_o}^2 + H_1$$

$$T = I + T_1,$$

where H_1 and T_1 are obtained from the decomposition of Z

$$Z = H_1 - {\omega_o}^2 T_1$$

and ${\Lambda_o}^2$ is a diagonal matrix whose elements are the square of the degenerate eigenfrequencies. In the computation of matrix elements, we take into account the effects of self coupling, fundamental mode along-branch coupling and spheroidal and toroidal mode coupling caused by rotation, ellipticity and lateral heterogeneity of the Earth. The density, S-wave and P-wave velocity perturbations are included but the potential perturbation is not.

Often tomographic mantle models are obtained by the inversion after the shallow layer correction, *i.e.,* crustal correction, in the raw data, such as travel times and waveforms, are modeled and subtracted. If a tomographic model is provided with a crustal model, for example all Harvard models except M84A of Woodhouse and Dziewonski (1984), we include the effect of lateral variation of surface topography, P, S velocity perturbations in the crust and the Moho and mid-crust boundary undulations. Woodhouse and Dziewonski (1984) describes a model of these corrections based on the ocean function expanded up to the same order as that used for the mantle.

The spherically symmetric PREM Q model is also included in H. When Q is included, the eigenvalue problem (eq. 5) becomes non–hermitian. Complex eigenvalues λ^2 and left and right eigenvectors A, B are computed by CRAY YMP at JPL using the LAPACK (Anderson *et al.*, 1992) numerical package. The largest eigenvalue problem used to compute synthetics in this thesis is for target multiplets ${}_0\mathrm{T}_{40}$ and ${}_0\mathrm{S}_{43}$ (upto 200 s). In this case ${}_0\mathrm{S}_l$, l=41–35 and ${}_0\mathrm{T}_l$, l=38–42 are the basis set and the total dimension of the eigenvalue problem is 840. Recently we extended the computation

to a higher frequency and with more multipets in a basis set. Barbara (1994) used the eigenfunctions with a period down to 125 s, target mulitiplets ${}_0T_{67}$ and ${}_0S_{75}$, with a basis set composed of ${}_0T_l$, l=64–70 and ${}_0S_l$, l=72–78, total dimension 2002, computed by the same algorithm.

For each multiplet k we solve the eigenvalue problem and only store the eigenfrequencies and hybrid eigenfunctions which have the largest component in the subspace spanned by the multiplet k. Usually we find $2l+1$ hybrid eigenfunctions except a few cases of strong Coriolis spheroidal-toroidal coupling. In a strongly Coriolis coupling case between ${}_0S_l$-${}_0T_{l'}$, we find $2(l+l')+2$ singlets which have the largest component in the subspace spanned by either ${}_0S_l$ or ${}_0T_{l'}$. Once we build a set of eigenfunctions for a 3D earth model, band-pass synthetic seismograms are computed by eq. 12 using all eigenfunctions ($\mathbf{a}_i$, $\mathbf{b}_i/j_i$) and the complex eigenfrequencies (λ_i) within the frequency band.

References

Anderson, E., Z. Bai, C. Bischof, J. Demmel, J. Dongarra, J. Du Croz, A. Greenbaum, S. Hammarling, A. Mckenney, S. Ostrouchov and D. Sorensen, 1992, *LAPACK Users' Guide*, SIAM. Philadelphia.

Barbara, A. R., 1994, A global tomographic model of shear attenuation in the upper mantle, *Submitted to J. Geophys. Res.*

Gilbert, F., 1980, An introduction to low-frequency seismology, in *Proc. Int. Scho. Phy., LXXVIII*, Dziewonski and Bosch ed., Amsterdam, North-Holland, 41-81.

Park, J. and F. Gilbert, 1986, Coupled free oscillations of an aspherical, dissipative, rotating Earth: Galerkin theory, *J. Geophys. Res.*, **91**, 7241-7260.

Golub, G. H. and C. F. Van Loan, 1989, *Matrix Computations* 2nd ed., Johns Hopkins Univ. Press, Baltimore.

Woodhouse, J. H., 1983, The joint inversion of seismic waveforms for lateral variations in Earth structure and earthquake source parameters, *Proc. Enrico Fermi Inst. Sch. Phys.*, **85**, 366-397.

Woodhouse, J. H. and F. A. Dahlen, 1978, The effect of a general aspherical perturbation on the free oscillations of the Earth, *Geophys. J. Astron. Soc.*, **53**, 335-354.

Woodhouse, J. H. and T. P. Girnius, 1982, Surface waves and free oscillations in a regionalized earth model, *Geophys. J. Astron. Soc.*, **68**, 653-673.

Woodhouse, J. H. and A. M. Dziewonski, 1984, Mapping the upper mantle: Three dimensional modeling of Earth structure by inversion of seismic wave forms, *J. Geophys. Res.*, **89**, 5953-5986